REFURBISHMENT AND COLD TESTING OF THE WISCONSIN FREE ELECTRON LASER ELECTRON GUN CAVITY

Troy Bennet Petersen

Submitted to the faculty of the University Graduate School in partial fulfillment of the requirements for the degree

Master of Science

In the Department of Physics

Indiana University

July 2023

Accepted by the Graduate Faculty, Indiana University, in partial fulfillment of the requirements for the degree of Master of Science.

Master's Thesis Committee

_____

William Michael Snow, PhD

_____

Michael P. Kelly, PhD

_____

Daniel Joseph Salvat, PhD

Acknowledgements

I would like to acknowledge multiple groups, the first being those involved with US Particle Accelerator School. This school has helped form the basis of my professional career and helped me expand upon my skillset and knowledge. In particular I would like to thank Susan Anderson, Irena Novitski, and Steven Lund for administering these sessions. Additionally, thank you to Professor Michael Snow and Daniel Salvat for serving on the thesis committee, as well as for the extensive comments and edits that helped make the document more concise and readable.

I would also like to thank my coworkers and managers (through three different jobs) that allowed and encouraged me to participate in this program, as well as to Argonne and Fermilab for supporting my education. I would like to thank those in my group (both current and those who have since moved on) who helped work on the WiFEL gun, as the bulk of this thesis would not be possible without you. This includes Mark Kedzie, Tom Reid, Jacob Packard, and Gongxiaohui Chen. In particular I would like to thank my manager and mentor Mike Kelly, who has patiently introduced me to and helped me comprehend almost every SRF concept in this thesis. Additionally, I would like to thank all of the staff who previously worked on WiFEL and were willing to lend a hand with explanations and documentation, in particular Mike Fisher, who aided us in many ways throughout this project. Lastly, Philippe Piot, who has helped in many ways during this collaborative project as well as with this thesis.

I would also like to thank those in my personal life who have supported me throughout this program. Eight sessions of being away for two weeks at a time is substantial, and I would like to thank my wife, Kim, for supporting me throughout. None of this would be possible without you.

Troy Bennet Petersen

REFURBISHMENT AND COLD TESTING OF THE WISCONSIN FREE ELECTRON LASER ELECTRON GUN CAVITY

The Wisconsin Free Electron Laser gun was tested at Argonne National Laboratory in December 2019. Its unexpectedly low Q_0 ~10^7 was caused by a niobium pentoxide contaminant. In this thesis I describe how this electron gun cavity was revived. A cold test after disassembly and cavity cleaning improved the cavity performance enough for future applications. We report measurement of microphonics, pressure sensitivity, field emission onset, Lorentz detuning, and multipacting relevant for performance. We discuss supporting simulations and operational and mechanical design lessons for application to future designs.

Table of Contents

Acceptance ii

Acknowledgements iv

Abstract v

Acronyms ix

Introduction 1

Basics of QWR SRF design 1

Basics of superconductivity 1

Surface Resistance, R_s 4

Residual Resistance Ratio (RRR) 6

Mean free path effect on R_{BCS} 7

RF cavity design 8

History of the WIFEL gun 12

Overview of WiFEL design 16

Cryostat Modification at ANL 18

RF Testing Overview 21

Signal measurement and calibration 21

Multipacting 27

Initial Cryostat Cooldown and investigation 29

Initial cold testing 29

CST simulations 34

Borescope investigation 37
Disassembly and cleaning of the WiFEL cryostat 40
Second Cooldown Testing 40
RF Testing Results 42
Multipacting 42
Q-curve results 44
Additional Cold Testing 45
Microphonics 45
Pressure sensitivity df/dp 46
Lorentz Detuning 47
Q disease testing 48
Exercising mechanical tuner 51
Summary of Cold Testing 52
Future Work 52
Multipacting simulations 53
Summary 53
Bibliography 55
Appendix A - Pillbox mode derivation 57
Appendix B - RF Photocathode field shape effects 60
Appendix C – Cleaning the cavity 67

Disassembly of the WiFEL cryostat 67

WiFEL Cavity Cleaning 73

WiFEL Clean Assembly 75

Curriculum Vitae .....

Acronyms

WiFEL – Wisconsin Free Electron Laser

FEL - Free electron laser

SRF – superconducting radiofrequency

UW – University of Wisconsin

SLAC – Stanford Linear Accelerator Center

ANL – Argonne National Laboratory

QWR – quarter wave resonator

DC – direct current

RF – radiofrequency

CW – continuous wave

LCLS-II – Linear Coherent Light Source II

AC – alternating current

RRR – residual resistance ratio

BCP – buffered chemical polish

HPR – high pressure rinse

DOE – Department of Energy

NbTi – Niobium titanium

ASME – American Society of Mechanical Engineers

NA – network analyzer

ADTF – Accelerator Development Test Facility

SEY – secondary electron yield

GaAlAs – gallium aluminum arsenide

UED/UEM – ultrafast electron diffraction/microscopy

TE – transverse electric

TM – transverse magnetic

DI – De-ionized

Introduction

The Wisconsin Free Electron Laser (WiFEL) Superconducting Radiofrequency (SRF) electron gun is a quarter wave resonator (QWR) accelerating cavity built as a source for high repetition rate, high intensity electron bunches. This cryomodule was conceived and constructed at University of Wisconsin (UW) Madison using a SRF cavity fabricated by Niowave, Inc. It was designed as a high brightness, high repetition rate source for an FEL design. The gun had been initially tested at UW, then moved to Stanford Linear Accelerator Center (SLAC) for tests. The gun was then transported to Argonne National Laboratory (ANL)'s Accelerator Development Group to run the cryomodule on a closed loop liquid helium refrigerator for further tests.

The QWR geometry of the WiFEL SRF is essentially a quarter wave stub shorted at one end which realizes a low frequency cavity at a reasonable size. Simpler geometries (such as an elliptical cell cavity) are too large for a given frequency to realistically manufacture. The frequency used in this WiFEL SRF design (199.6 MHz) is desirable for low-beta accelerators, particularly for ion linacs [1], where the low frequency provides a quasi-static accelerating field that helps to shape a small beam bunch emittance. Low-beta refers to lower particle velocity, with beta being the particle velocity over the speed of light. More details on this geometry and other cavity geometries are provided in subsequent sections.

Basics of QWR SRF design

Basics of superconductivity

There are many reasons why superconducting materials are chosen to fabricate accelerating cavities rather than normal conducting materials. The very small surface resistance in a superconducting cavity material reduces the power dissipation in the cavity by factors of 10^5-10^6 compared to normal conducting cavities [2]. This tremendous advantage often outweighs the disadvantages that make SRF systems more complicated to operate, which include the cryogenic systems required to keep the cavity

superconducting coupled with associated technical problems from microphonics, Lorentz detuning, and cavity quenches. Superconducting cavities allow continuous wave (CW) or high-repetition pulsed operation at high fields up to tens of MV/m. This makes them well suited for unique applications such as a MHz source for an FEL like the LCLS-II. High gradient normal conducting cavities made from copper must be operated in a pulsed RF mode in order to limit the total dissipated power to manageable levels.

Kammerlingh-Onnes discovered the zero DC electrical conductivity of a superconductor below a critical temperature in 1911. Meissner and Ochsenfeld discovered the perfect diamagnetism of a superconductor in 1933. Mathematical equations invented by the London brothers in 1935 to capture this physics were further developed by Pippard, who introduced the concept of the coherence length using a nonlocal form of the London equation. Ginzberg and Laundau proposed in 1950 a more general theory to explain many additional superconducting phenomena poorly described by the previous theories. Bardeen, Cooper, and Schrieffer won the Nobel Prize in physics for their microscopic theory of superconductivity published in 1957, which finally made clear the fundamental physical origin of the effect. The field of superconductivity is quite vast and has expanded well beyond these pioneering theories. [3]

The phenomenon of superconductivity is well described by the Bardeen-Cooper-Schrieffer (BCS) theory, which details the interaction of electrons with the crystal lattice via phonons (quantized lattice vibrations) [4]. This theory shows that two electrons can have a net attraction due to the distortions in the lattice caused by the same electrons. Figure 1 illustrates how these electrons can form Cooper pairs that allow them to move through the lattice without scattering. These lattice distortions (or vibrations) come in quantized lattice vibrations referred to as phonons. This pairing of electrons mediated by phonons is analogous to the electromagnetic interaction of charges mediated by photons, but it is an attractive force in contrast to the repulsive electrostatic interaction between like charges in vacuum. [2]

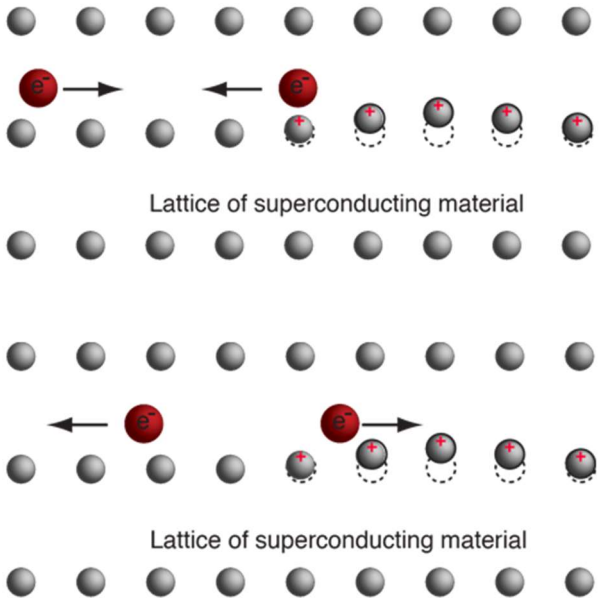

Figure 1. Electrons passing through metal crystal lattice distort the lattice and provide a net attractive interaction with a second electron. [5]

At T = 0 K all electrons condense into Cooper pairs, and the number of unpaired electrons decreases exponentially with rising temperature (as $e^{-\Delta/kT}$, where Δ is the pairing energy, k the Boltzmann constant, and T is temperature). Current flow in a superconductor is located within a thin layer at the surface, characterized by a parameter called the London penetration depth. These "supercurrents" shield unpaired electrons from static fields outside of the superconductor. Alternating fields can penetrate the surface of the superconductor and subsequently affect unpaired normal conducting electrons, leading to energy dissipation. The depth of these fields depends on surface properties and properties of the external field like frequency. The temperature of the superconductor affects the number of normal conducting electrons compared to superconducting electron pairs. The combined action of these two different conduction mechanisms leads to a "two-fluid" theory, a mix of superconducting and normal conducting current carriers superposed on each other.

The perfect diamagnetism of superconductors, known as the Meissner effect, is characterized by the complete expulsion of magnetic flux from the superconductor as the temperature is lowered below the

critical temperature T_c into the superconducting state. This is NOT what a perfect conductor described by classical electrodynamics would do: a perfect conductor would trap the magnetic flux inside while passing through the critical temperature rather than expelling it. These two cases are illustrated in Figure 2.

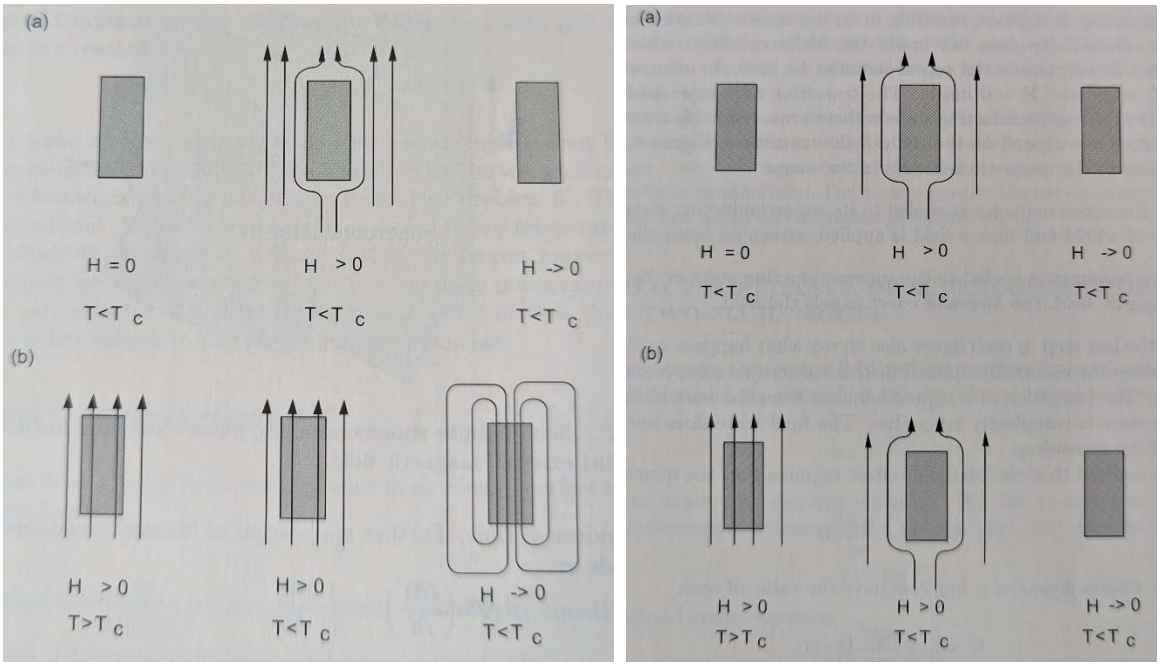

Figure 2. Illustration of the response of a perfect conductor (left) and a superconductor (right) to the presence of a magnetic field when a) already under T_c and b) when transitioning through T_c. [2]

Surface Resistance, R_s

While direct current (DC) resistance in a superconductor is exactly zero, this is not the case for an alternating current (AC). A superconductor's current is carried near the surface in both the DC and AC cases in a layer of material characterized by the London penetration depth. Normal conductors carry AC current in a surface region characterized by the skin depth. The surface resistance (R_S) of a superconductor is generally described as the sum of two parts, BCS resistance (R_{BCS}) and residual resistance (R_{res}). [2]

$$R_s = R_{BCS} + R_{res} \quad (1)$$

The residual resistance is a temperature independent [7] component of the surface resistance above R_{BCS} which lumps in various "nonideal" effects, such as flux trapping (due to exposure to ambient magnetic field during transition) as well as "hydrogen Q-disease" from hydrogen impurities in the metal. R_{res} generally ranges from 5-10 nΩ for well-prepared niobium, with values measured as low as 0.5 nΩ. [6] This resistance can be minimized but not eliminated and sets a lower bound to the surface resistance even at arbitrarily low temperatures.

R_{BCS} as predicted by the Bardeen-Cooper-Schrieffer theory of superconductivity describes the resistance from the remaining normal conducting electrons scattering off lattice impurities/interstitials in the near-surface region where the supercurrent is flowing. [7] It is displayed in Equation 2, where ω is the angular frequency, T is temperature, Δ is the energy gap, and k is the Boltzmann constant. The function A depends on the London penetration depth (λ_L), coherence length of the Cooper pairs (ξ_F), the mean free path (l), and the square root of the normal state electrical conductance (ρ_n).

$$R_{BCS} = A\left(\lambda_L^4, \xi_F, l, \sqrt{\rho_n}\right)\frac{\omega^2}{T}e^{-\Delta/kT} \tag{2}$$

Equation 3 shows the RF-specific phenomenological equation for this surface resistance

$$R_{BCS} = 2 \times 10^{-4}\frac{1}{T}\left(\frac{f}{1.5}\right)^2 e^{-\frac{17.67}{T}} \tag{3}$$

which scales with the frequency squared and decreases exponentially with temperature (frequency f in GHz, and temperature T in K). [2] These features guide design trade-offs for cavities. For example, one can operate at higher temperatures while keeping losses acceptable if the resonant frequency of the cavity is sufficiently low.

Residual Resistance Ratio (RRR)

A high value of the residual resistance ratio (RRR), defined as the ratio of electrical resistance at 300 K to 4.2 K, is an advantageous characteristic for modern SRF cavity material. This ratio gives a quantitative value of impurities within the metal that cause scattering of electrons (the classical cause of resistance in a metal); a higher RRR value corresponds to a higher purity metal sample. The RRR definition as an engineering parameter for SRF cavity design loses some of its usefulness when T_c is greater than 4.2 K, with multiple approaches to obtaining an accurate RRR measurement on a superconductor. [8] Sometimes this is as simple as taking the ratio at 10 K instead of 4.2 K, just above the superconducting transition.

While starting with a lower resistance at room temperature is beneficial, it is not the reason for requiring high RRR materials for an SRF cavity as R_{BCS} depends weakly on the normal state conductance. High RRR niobium is instead used to satisfy thermal stability requirements, allowing any heat generated by surface resistance to be wicked away to the helium bath quickly enough such that the local niobium surface temperature stays below the critical temperature. [7] Heat is conducted by two means within a metal: by electrons and by phonons. Phonons are quanta of energy corresponding to lattice vibrations, and their number density within a volume increases as T^3. At low temperatures the thermal conduction is therefore dominated by electrons. In an "electron cloud" model, the thermal conductivity scales directly with the normal state electrical conductivity, as given in Equation 4, where κ is thermal conductivity, σ is electrical conductivity, T is temperature, and L is the Lorenz number [2].

$$\frac{\kappa}{\sigma} = LT \tag{4}$$

High RRR niobium is chosen for the bulk cavity material since having high electrical conductivity corresponds to a high thermal conductivity at low T. This allows for better removal of heat on the SRF surface and allows for higher fields to be achieved without quenching the superconducting cavity.

As the superconductor cools past the critical temperature, the paired electrons are no longer able to carry thermal energy effectively and the main mechanism shifts to phonon interactions. The thermal conductivity of the superconductor therefore drops off sharply below T_c. Electrons also stop acting as scattering sites for phonons below the critical temperature, which greatly increases the thermal conductivity for the few remaining phonons (as they scale with T^3). [2] The remaining scattering sites are lattice discontinuities such as interstitial light elements as well as grain boundaries. As phonon scattering scales with the number of impurities, it stands that a high RRR superconductor is desirable for high thermal conductivity below the critical temperature.

Mean free path effect on R_{BCS}

The mean free path for a given metal greatly affects the BCS resistance, perhaps quite counterintuitively. Figure 3 below shows the calculated BCS resistance for niobium at 1.5 GHz at two temperatures. There is a minimum to the BCS resistance where the mean free path is approximately equal to the coherence length ($l \sim \xi$), near 200 Å for niobium at 1.5 GHz. A mean free path much greater than the coherence length is known as the "dirty limit," and much less is known as the "clean limit." In the "clean limit" (to the right of the BCS resistance minimum) the resistance increases as the relevant length scale becomes the London penetration depth instead of the mean free path. This behavior is similar to the anomalous skin effect in normal conductors. [6]

Figure 3 clearly shows why it can be advantageous to add impurities to high RRR material using various surface treatments. Controlled impurity doping of the surface region with nitrogen doping improved the cavity Q by more than a factor of 3. [9] Nitrogen infusion has enabled Q values above 10^{10} with surface resistances as low as 0.63 nΩ. [10]

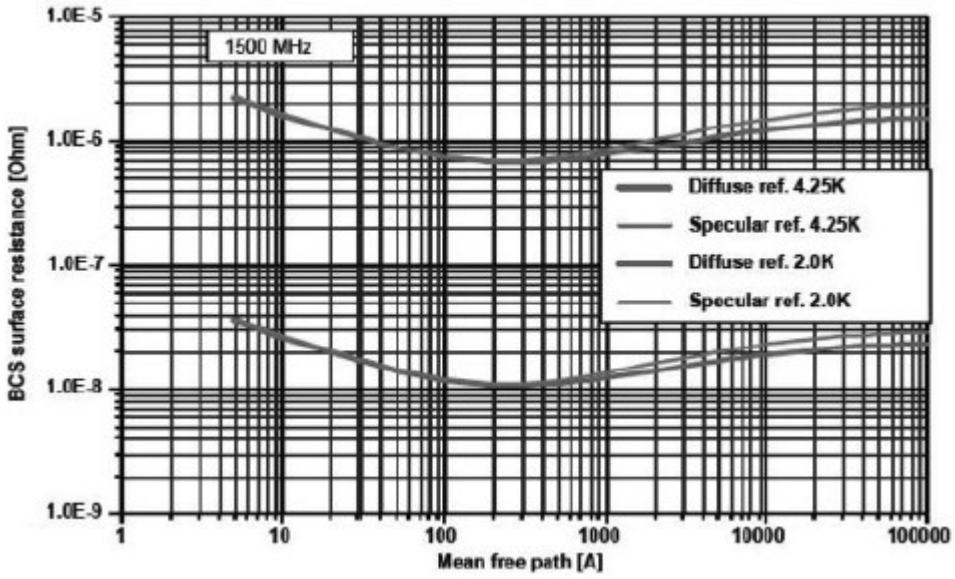

Figure 3. Mean free path vs BCS resistance for niobium at 1.5 GHz at two temperatures. [6]

RF cavity design

RF cavities can vary in geometry and purpose but are all designed to electromagnetically resonate at a certain frequency specific to the particular accelerator and purpose of the cavity. A given geometry is characterized by a series of eigenmodes at well-defined frequencies. Most are designed to provide an electric field that provides a "kick" of one kind or another to incoming particles. This kick can provide an energy increase, phase space movement, or focusing depending on the cavity type. In an electron gun, electrons are generated from the cathode at very low energy. Many modern electron guns use a laser pulse striking a photocathode.

There are many nuances to cavity design, and many general categories of RF cavities that work in specific conditions. Quarter wave resonators are often chosen for accelerating low beta particles. The low-frequency operation provides a DC-like field, and having many independently phased resonators allows for great flexibility for ion guidance. Figure 4 shows an overview of common cavity geometries.

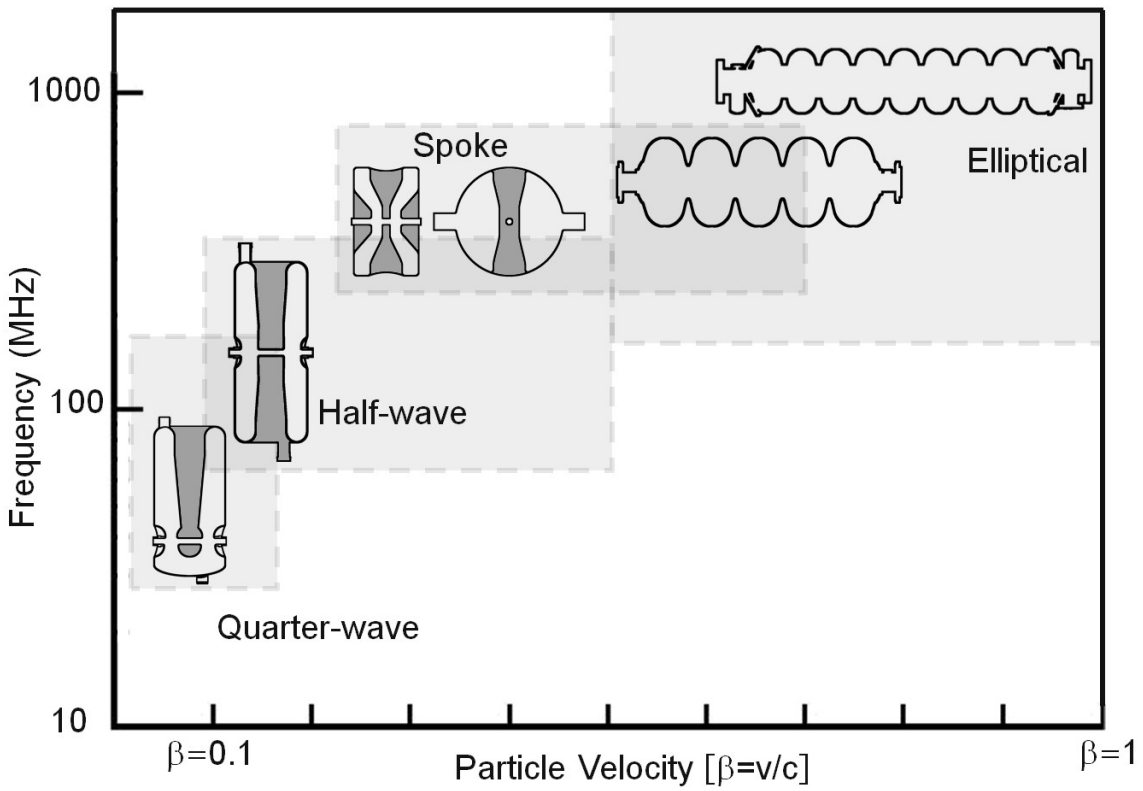

Figure 4. Design regimes for various cavity types, showing which cavity types suit certain frequencies and particle velocities. [1]

The most basic RF cavity is generally considered to be the pillbox cavity. The pillbox cavity is a hollow cylinder with a fundamental mode dictated by the cavity diameter. A derivation of the fundamental pillbox cavity mode frequency is included in Appendix A. Figure 5 shows an illustration of the E and H fields for a cylindrical pillbox cavity.

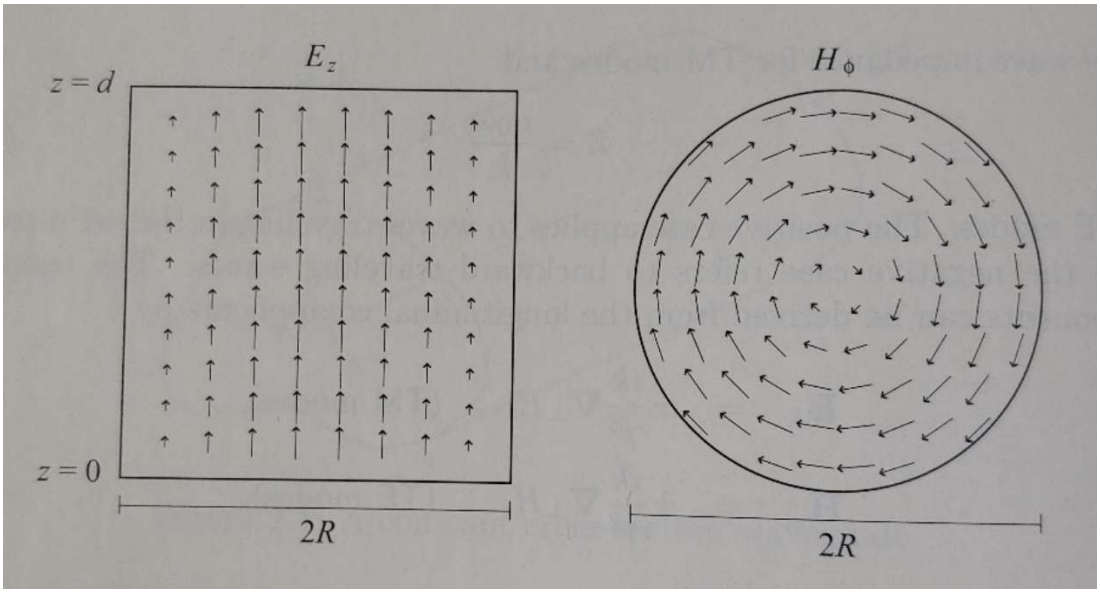

Figure 5. E and H fields for the fundamental TM pillbox mode. [2]

Quarter wave resonators are the most compact resonator geometry at a given frequency so that they are particularly useful for low beta linear accelerators [1]. The two-gap QWR design shown in Figure 6 is used in linear ion accelerators.

Low frequency QWRs are also desirable for certain gun applications when turned on its side [11]. Figure 6 shows the orientation of the e-gun style QWR compared to the regular, two-gap QWR. The field between the center conductor and the “dome” part of the cavity is the accelerating field. The electric field along the beam axis is shown in Figure 7.

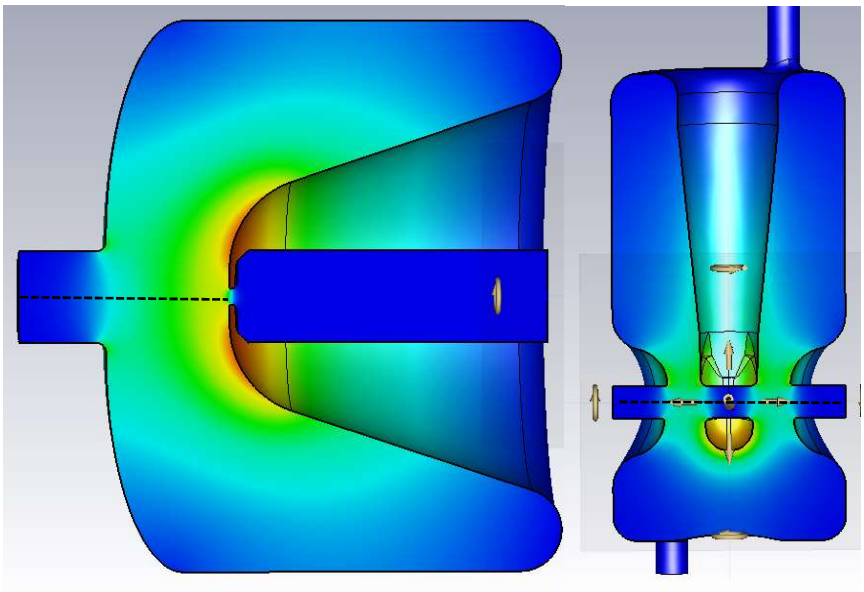

Figure 6. Comparison of WiFEL quarter-wave resonator compares to the more conventional, two-gap QWR design (dashed black lines are beam axes). Red/yellow indicates higher electric field magnitude, while blue is the lowest.

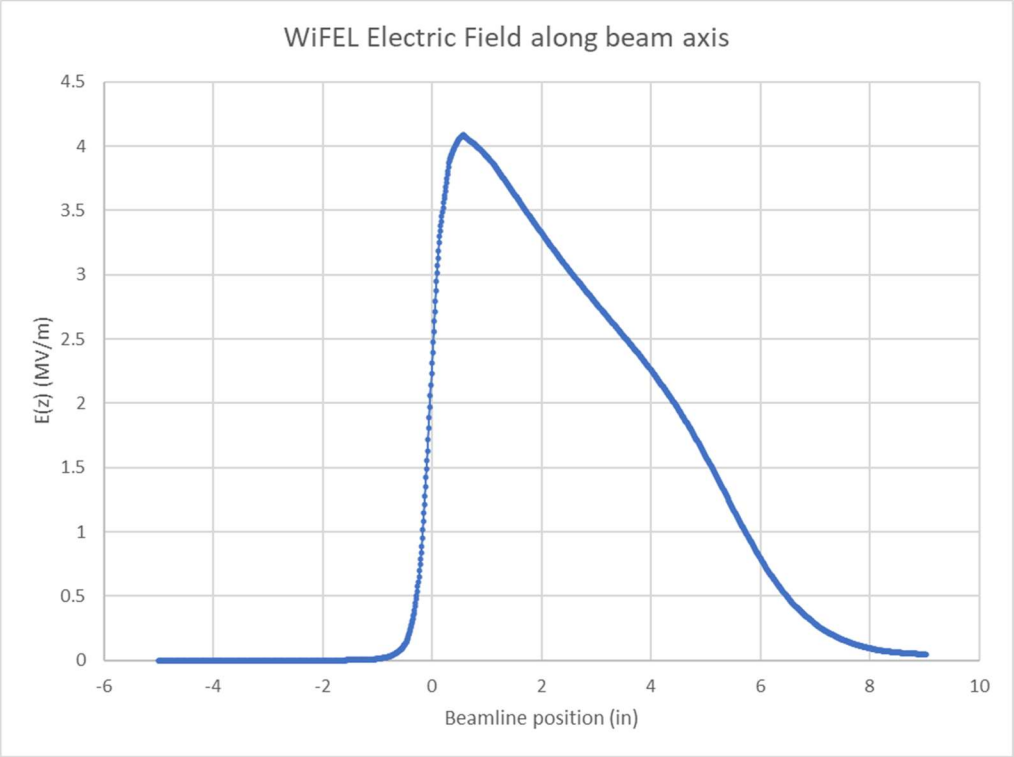

Figure 7. Electric field along the beamline axis of the WiFEL cavity (modeled without cathode inserted), fields normalized to 1 Joule stored energy in CST.

This flat field profile shape is one of the reasons that this cavity design was chosen for the WiFEL e-gun. The relatively low slope of the field along the beamline helps to reduce the radial electric field, which in turn reduces emittance growth of the beam. The relationship between the radial field and the spatial derivative of the longitudinal field can be described by using the Penofsky-Wenzel theorem [2]. The optimization of the shape of an e-gun cavity was explored during the initial design of a next generation electron gun cavity. It is possible to obtain an even flatter field profile by changing basic elements of the cavity geometry at the cost of a lower peak field. Flattening the E_z field profile even more while keeping the same peak field is likely possible in future designs. Appendix B presents additional investigations of the field shape. We decided that the current profile was sufficient for the desired beam characteristics.

History of the WIFEL gun

The WIFEL gun was designed and built for the University of Wisconsin, with the cavity fabricated by Niowave, Inc. The design of the gun was based on a similar design from the Naval Postgraduate School gun. The cavity electromagnetic modeling design was all done at UW. The figures of merit and other operating parameters for the cavity design are given in Table 1. Particularly interesting are: Q_0, energy gain, R/Q, G, and static heat loss. These figures of merit (energy gain, shunt impedance, peak RF fields, static heat loss) are comparable to the best designs known today. Argonne half-wave resonators operate at an energy gain of 1.26 MeV and dissipate 40 watts. [2]

Temperature	4.2	K
Cavity Frequency @ 4.2 K	199.6	MHz
Cavity vacuum at 22 °C	1.00E-08	Torr
Helium dewar vacuum at 22 °C	1.00E-06	Torr
Unloaded Q (Q_0), nominal at nominal E Accelerating	2.50E+09	
Peak surface electric field, nominal	53	MV/m
Energy gain at nominal Q_0	3.96	MeV
R/Q	147.9	Ω
G	85.7	Ω
G*R/Q	12.67	$k\Omega^2$
Max Transverse Dimension	0.6	m
Cathode Aperture	1.2	cm
Cavity Mass (Nb)	63.9	kg
Dynamic heat loss at Peak surface electric field	39.2	W
Static Heat loss of cavity and dewar	15	W

Table 1. Cavity design parameters for the WIFEL cavity. [12]

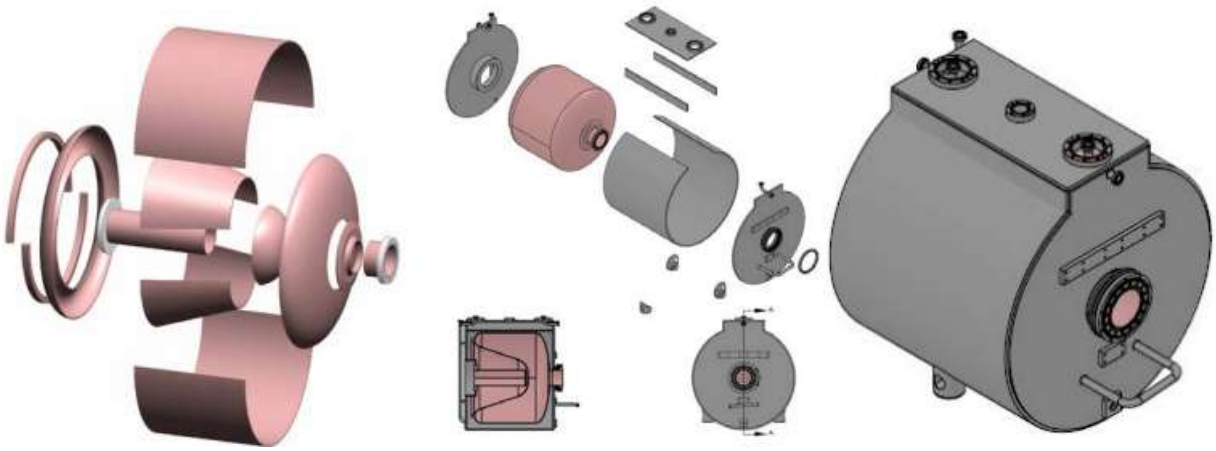

Figure 8. WiFEL cavity components sectioned to show weld seams for the cavity and helium jacket, with pink being niobium and gray being titanium. Jacketed cavity is approximately two feet long. [12]

The cavity and helium jacket were fabricated using standard SRF techniques. Welding of the high purity niobium (RRR>300) was done under vacuum (<50 µTorr) and the niobium was allowed to cool enough to suppress oxide formation and minimize gettering when reintroduced to atmosphere. Grade 2 titanium (a common commercially available grade of titanium) was used and all welds were performed in inert gas. Custom titanium bellows provided compliance between the cavity NbTi flange and the titanium helium jacket. Two GaAlAs diodes were bolted onto the cavity body to provide cryogenic

instrumentation, and a 20 W heater was installed to speed warmup of the cavity/cryostat assembly. The cryogenic sensors were bolted to the top and bottom of the cavity, with the heater placed at the bottom of the helium jacket.

The cavity was etched with a buffered chemical polish (BCP) to remove 120 microns of niobium and was baked at 600°C for 24 hours to remove hydrogen in the niobium, which can cause cavity performance degradation dubbed "Q-disease". The buffered chemical polish is a 1:1:2 mixture of hydrofluoric, nitric, and phosphoric acids. [2] Following the bake-out the cavity underwent another (light) BCP process to remove 30 microns of material (approximately ¼ of the time spent etching initially) and was high pressure rinsed (HPR) with de-ionized, ultrapure water at 1600 psi for 5 hours both before and after the cavity jacket was welded on.

The bare cavity was tested at Niowave, Inc. in a helium dewar at atmospheric pressure before the helium jacket was welded on. Initial testing after fabrication done at UW and shown in Figure 10 measured a cavity Q_0 of nearly 1 x 10^9 at 4.2 K and at low fields with a maximum accelerating voltage of almost 500 kV. The gun was later shipped to SLAC for additional testing. Two issues constrained the testing at UW and SLAC. The lack of a closed loop helium system necessitated cooling in batch fills using helium dewars. The associated transient pressure fluctuations complicate the measurements during the limited testing time. RF power measurements were made calorimetrically rather than by direct measurement of the forward, reflected, and transmitted RF signals. Accurately measuring the power dissipated in the helium system is not trivial. Figure 9 shows a decay curve measured by Niowave. The curve shows two measurements, with (Q_L) and without (Q_C) the drive cable attached. Figure 10 shows the measured Q curve with radiation levels (from field emission as the cavity reaches its operating limit). Q curves are explained in more detail in a later section.

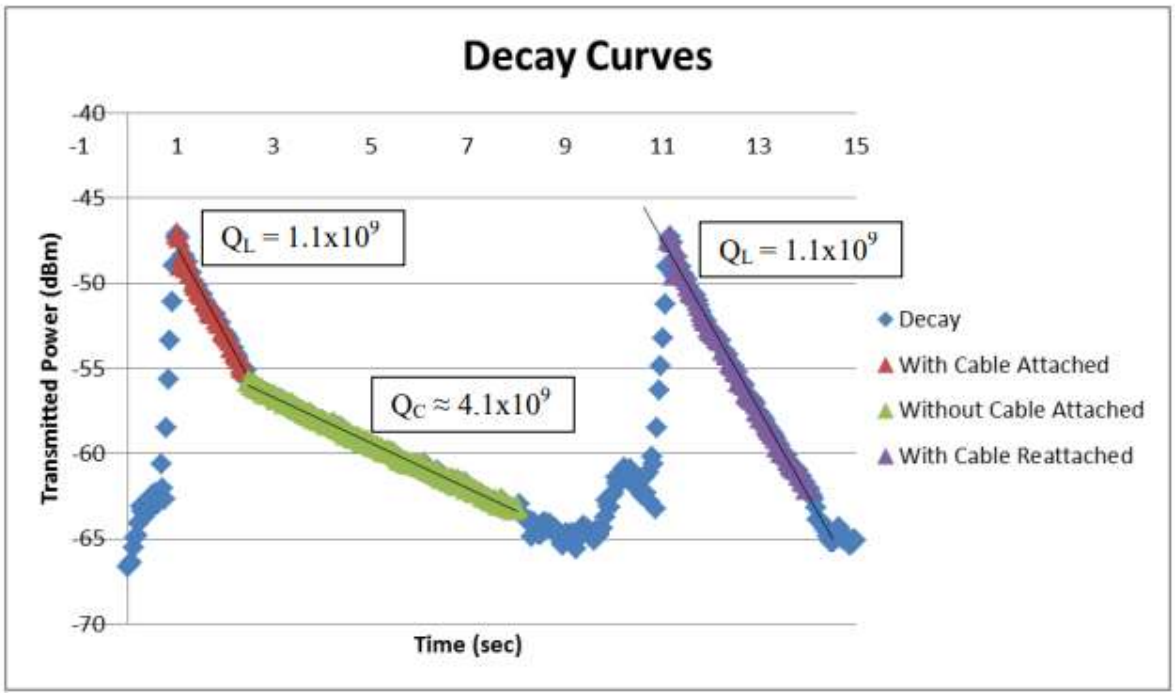

Figure 9. Results of initial testing of the WiFEL cavity as UW. [12]

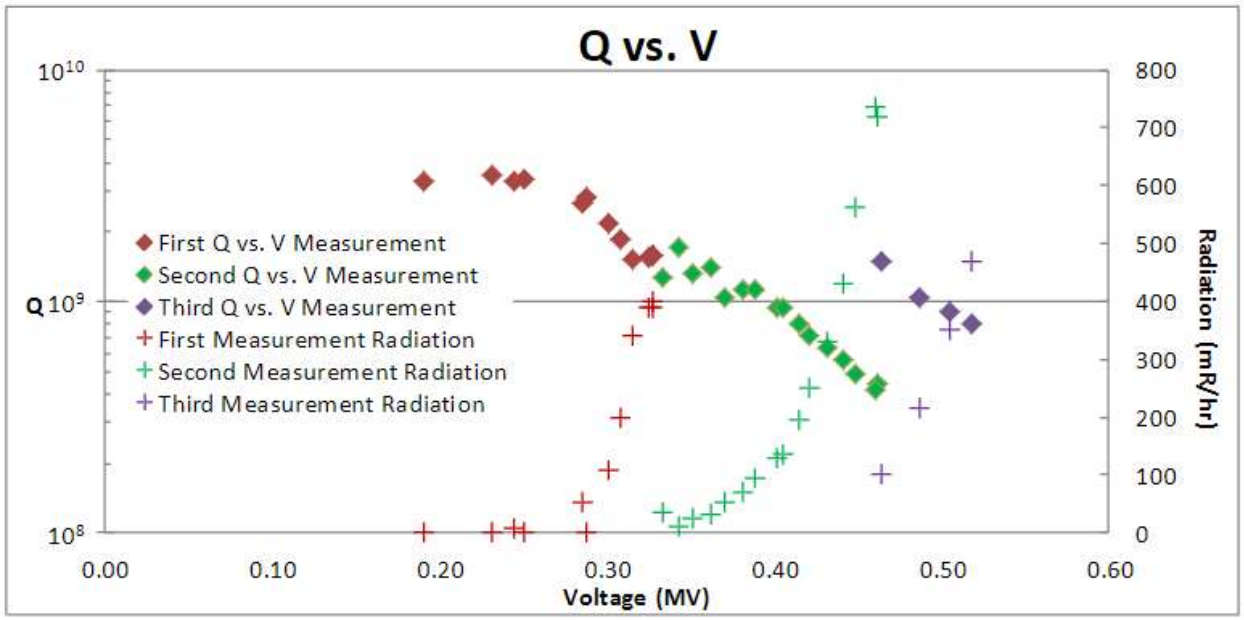

Figure 10. Q curve results from Niowave, Inc. [12]

Argonne has a liquid helium refrigerator to run the gun as a closed system and expertise in quarter wave resonator designs, so the gun was shipped to ANL in December 2019. The initial test in the "as-received"

state in December 2020 revealed a very low cavity quality factor, ~10^7. After performing a full cavity disassembly, cleaning, and re-assembly followed by a second cold test, we measured Q near 10^9. The cavity operated stably with E_{peak} = 14.3 MV/m and V_{acc} = 1.07 MV.

Overview of WiFEL design

Figure 11 shows a section view of the cryostat model for the "ship-in-a-bottle" style WiFEL design.

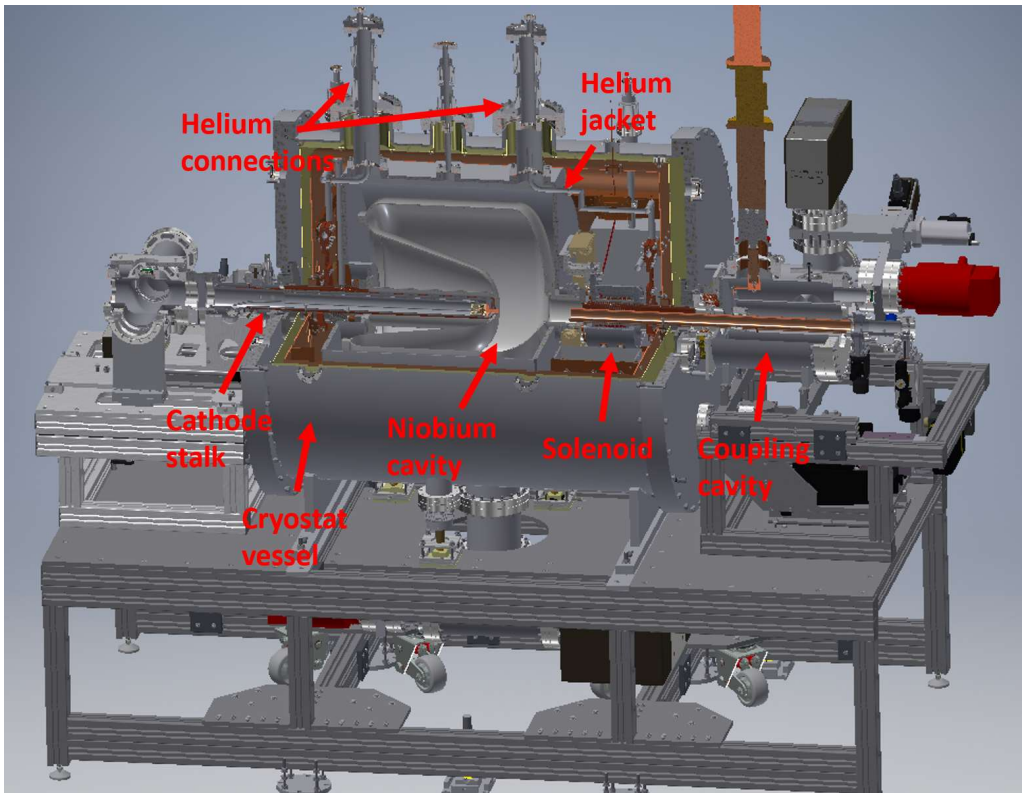

Figure 11. A section view of the cryomodule, table, and associated beamline components as originally received from SLAC.

The superconducting niobium cavity is the curved device inside the cryostat near the beam axis. In operation with a cathode plug to produce beam, a laser pulse will enter from the right and strike the photocathode, emitting a pulse of electrons. These electrons will be accelerated by the cavities electric field and exit the cavity through the beamport on the right. A hole at the center point of the nose or center conductor of this cavity allows for photocathode insertion almost flush with the cavity face. This

is perhaps the major design and operations issue for gun designs requiring high gradient (E > 15 MV/m) at the cathode. For our testing purposes we were initially concerned with proving cavity performance without the cathode and cathode stalk, mostly as a means of simplifying the first test run. This cathode stalk port was used as an RF probe of known coupling, a critical measurement for our testing. The cavity itself is supported by three kinematic feet fabricated from thermally-insulating G10 Garolite material which penetrate the cryostat walls at the bottom and are supported by the cryostat table.

While the cavity is well optimized for electromagnetic properties (peak fields, shunt impedance, geometry factor), several lessons were learned during the refurbishment work for future SRF e-guns. The addition of cleaning access ports in the cavity would improve the high pressure rinsing step. Moving the main power coupler from the beamport to a separate port could allow for a more easily movable coupler setup to allow for a critically coupled state for RF measurements (which simplifies the measurement process) and over-coupled for operation or for RF conditioning purposes. The beam-axis coupler is movable by manually moving the entire coupling cavity, but the range of coupling and difficulty of moving the coupler in and out are suboptimal. The coupling cavity is an intermediate resonant structure that transfers power between the incoming coaxial line and the on beam-axis power coupler. An off beam-axis coupler is a more standard configuration in other designs.

The cavity experienced a significant low field multipacting barrier. Extensive simulation and optimization work showed that this shape can be improved to reduce or entirely remove this multipacting barrier, which would be of great operational importance for a real electron gun. Changing the cathode plug would likely require conditioning through this multipacting barrier. The many hours consumed by this process would likely be unacceptable for electron gun operations at a light source.

Cryostat Modification at ANL

Many modifications to the cryomodule had to be performed after delivery of the cryostat from SLAC. A vacuum leak check revealed a large leak in the cavity RF space from the damaged bellows shown in Figure 12. A new section of bellows had to be welded onto the coupling cavity. Figure 13 and Figure 14 show the coupling cavity removal and re-assembly with the repaired bellows.

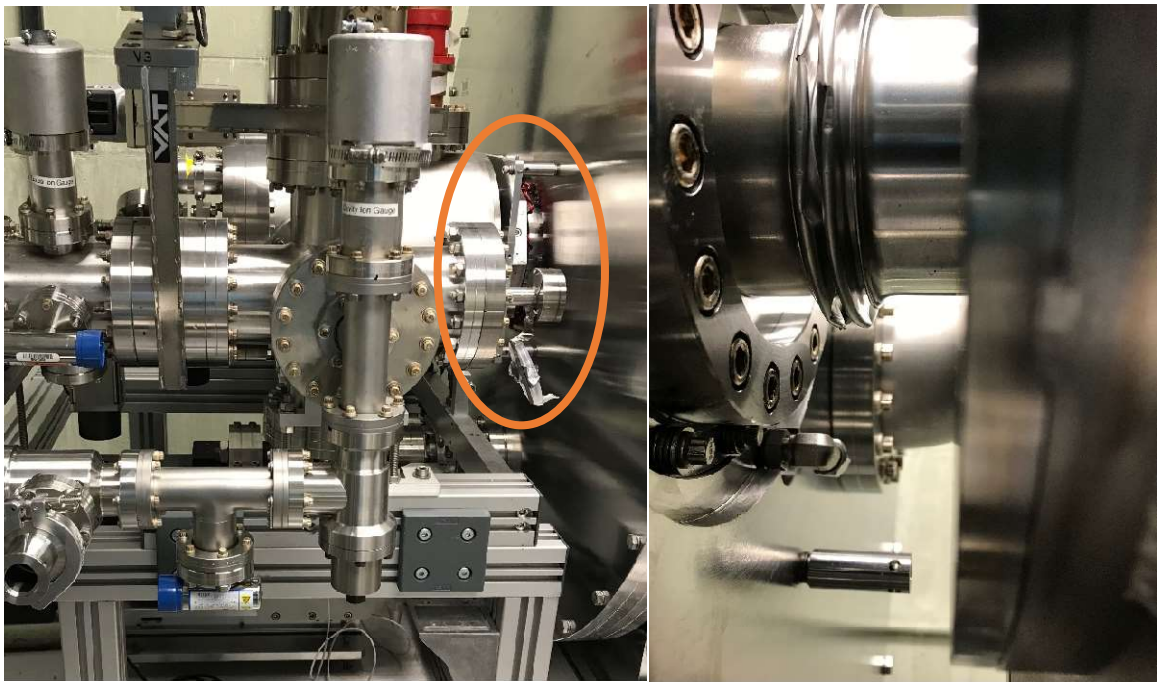

Figure 12. Location of bellows on the cryostat (left) and closeup (right) of damaged bellows identified for repair.

Figure 13. The coupling cavity (with damage beamline bellows) being removed in the clean room.

Figure 14. Re-assembly of coupling cavity to the cryomodule with new beamline bellows. The copper coupler is removed during this operation and was inserted later.

Connecting the WiFEL cryostat to the ANL liquid helium refrigerator required us to install a helium bayonet connection, shown in Figure 15, and to install ASME-certified burst discs at the helium ports, the RF space, and the insulating vacuum space, shown in Figure 16.

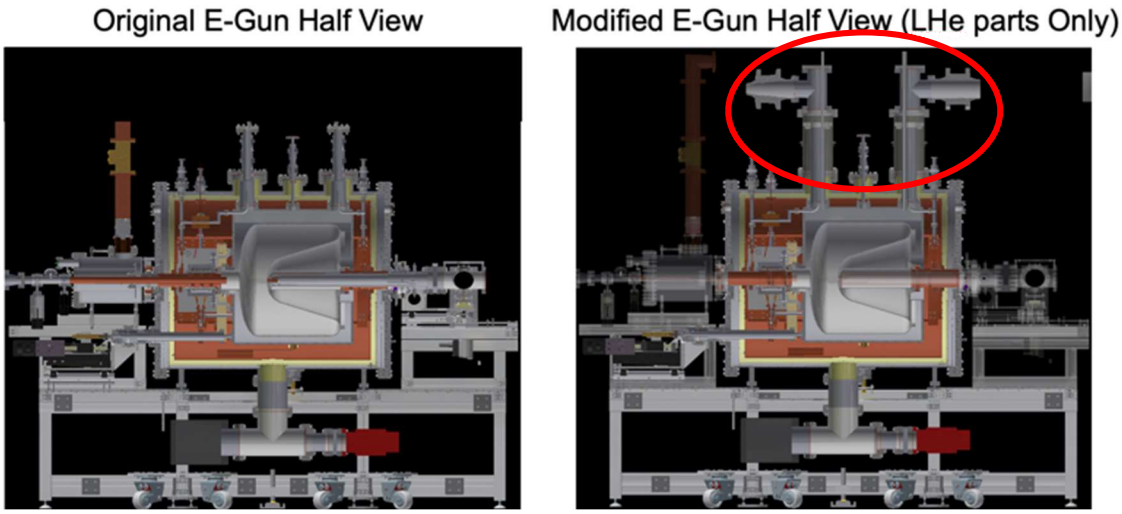

Figure 15. Model section views of the cryogenic interface modifications. Each of the two new large stacks above the cavity (circled in red) is an integrated helium bayonet connection and ASME burst disk assembly.

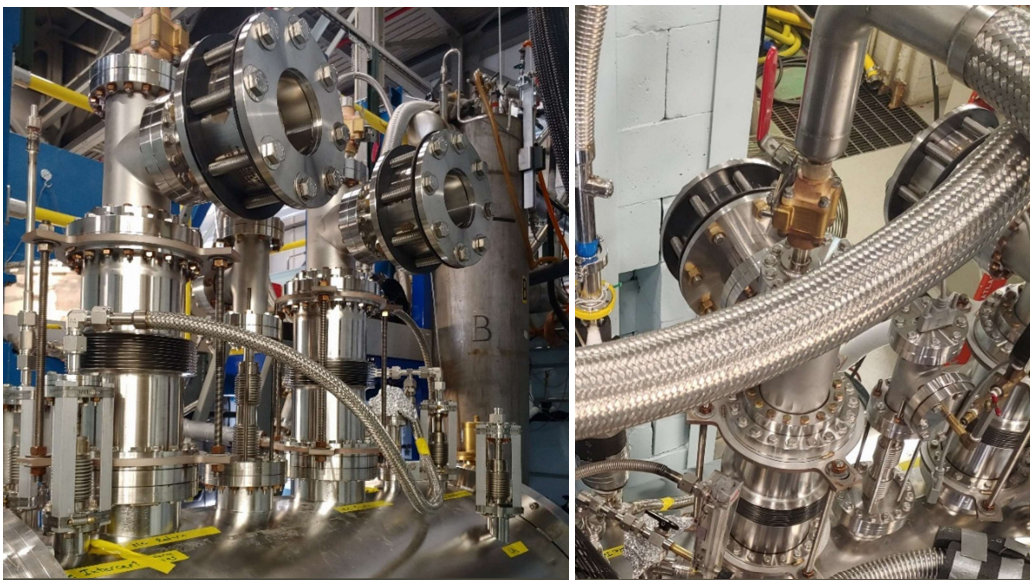

Figure 16. Two of the added burst disc assemblies (left) and helium bayonet connection (right) installed on the WiFEL cryostat.

We removal the entire cathode stalk assembly and replaced with an RF field probe with a length determined through CST Microwave Studio simulations to achieve the desired coupling strength. A

replacement RF probe is shown in Figure 17. The probe assembly required shielding from ambient light as well as a nitrogen system thermal intercept (the large copper piece and stainless-steel tubing).

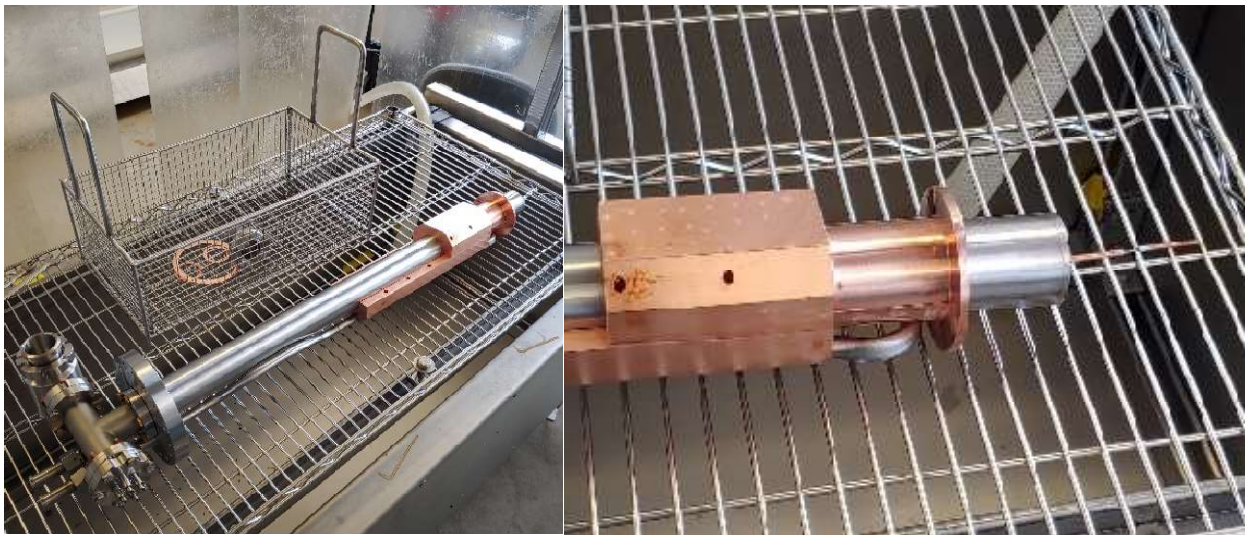

Figure 17. RF field probe assembly post-cleaning (left), close up of antenna at the end of the assembly (right)

We also replaced thermocouples with cryogenic silicon diodes to allow accurate temperature measurement below the range covered by thermocouples and added pressure gauges/transducers.

RF Testing Overview

Signal measurement and calibration

The general process of testing SRF cavities is described in the following section as a primer for the RF results. All equations and formulas in this section are given in Padamsee [2]. A network analyzer (NA) is a common tool for a whole host of RF measurements, and is especially useful for initial, warm measurements of the cavity system (coupler, resonator, and pickup probe).

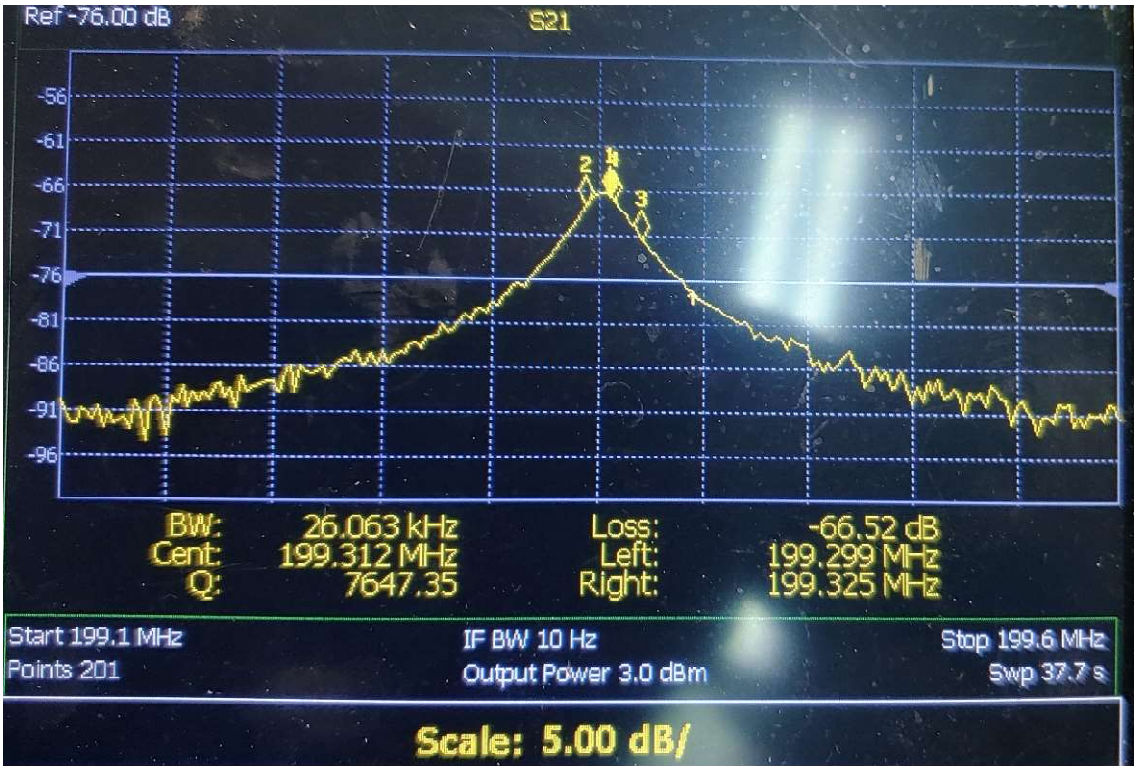

Figure 18. S21 measurement of the WiFEL cavity in the warm state, with a Q_L = 7650. Taken during the clean assembly before the second round of cold testing.

An example of this scattering parameter measurement (S21), taken at room temperature, is shown in Figure 18. Scattering parameters are ratios of voltages taken at different ports in an RF system, with S21 being the ratio of the output voltage to the input voltage. This measurement is performed over a specified frequency sweep, providing a plot like that shown in Figure 18.

The Q_L value of 7650 is in reasonable agreement with simulation values for the cavity shape (so called geometry factor, G) along with an expected value for surface resistance (R_S) for clean, high purity niobium at room temperature. The relationship between the quality factor (Q_0), surface resistance (R_S), and geometry factor (G) is given below in Equation 5. The WiFEL cavity geometry factor was simulated to be 85.7 ohms, meaning the room temperature surface resistance of this niobium is approximately 11 mOhm. Q_0 will continue to grow as the cavity cools and the surface resistance drops, until the critical temperature of niobium at which the Q will increase by many orders of magnitude.

$$Q_0 = \frac{G}{R_s} \tag{5}$$

A network analyzer becomes ineffective once the cavity is superconducting as the 3 dB full width half maximum (FWHM) bandwidth of the cavity is too narrow for the NA to resolve quickly. The NA can also miss the resonance peak as microphonic noise shifts the extremely narrow peak of this resonance curve as the vibrations detune the cavity. In the superconducting state RF measurements must instead be made with a phase-locked loop. Figure 19 shows this setup in block diagram format.

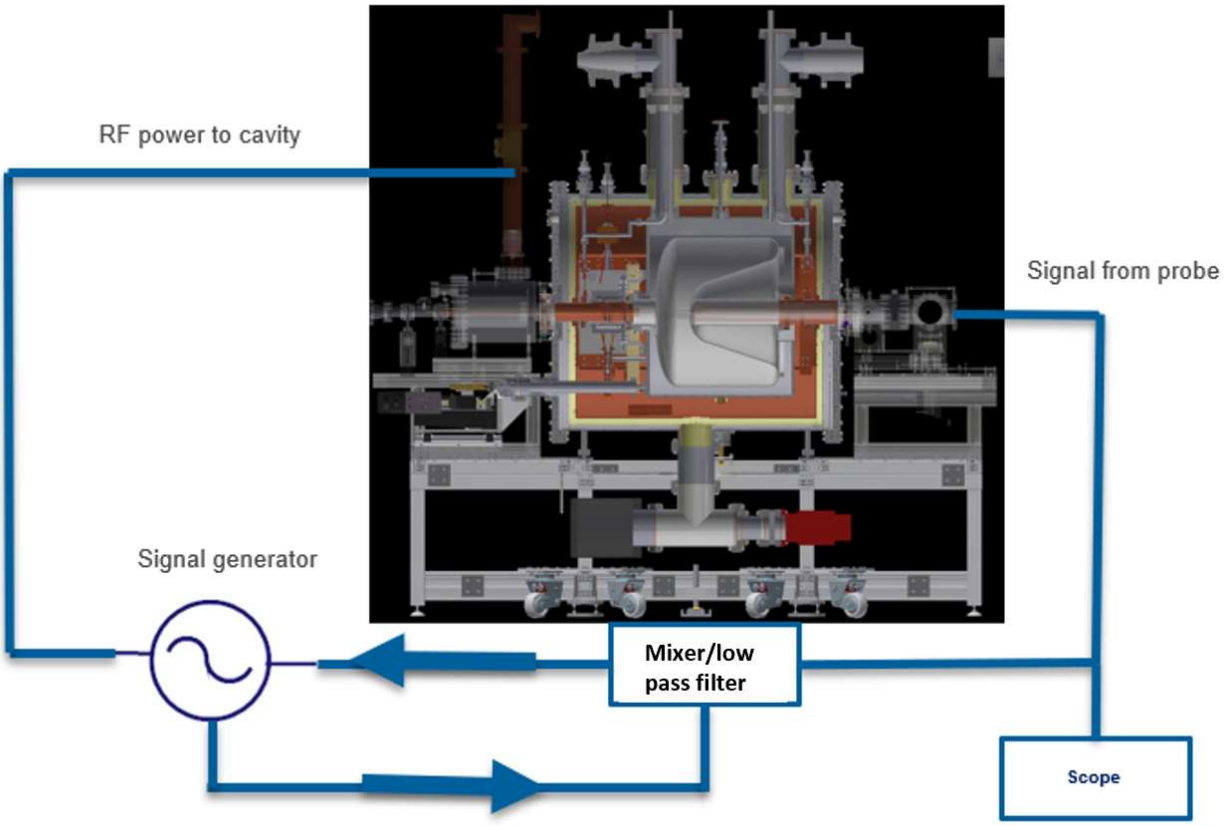

Figure 19. Block diagram of phase locked loop setup for resonator measurement and testing.

A phase-locked loop allows the cavity to be driven by a signal generator while using feedback from the pickup probe to track the eigenfrequency as it changes due to microphonics, pressure changes, or other

effects. This allows tracking within a set bandwidth, usually hundreds of hertz to a few kilohertz, depending on the loop settings.

The phase-locked loop works by exciting the cavity with a signal close to the eigenfrequency, taking the signal from the pickup loop, comparing it to the set frequency, and adjusting the output signal to minimize the error. The error signal is the product of mixing the signal generator output signal with the signal from the cavity. This signal is fed into a voltage-controlled oscillator built into our device for this purpose so that the error signal appropriately adjusts the frequency. The loop works to reduce the error signal and matching the phases of the signals (and therefore their frequencies).

The error signal also provides a way to monitor the microphonics of the cavity system. By sampling the error signal over time and taking the Fourier transform, once can decompose the signal into its constituent frequencies. This sort of measurement is crucial for operating a cryomodule such as WiFEL.

For the actual measurement setup in the Accelerator Development Test Facility (ADTF), the three signals of interest (voltage signal for forward, reflected, and transmitted power) are read by an oscilloscope. These values are calibrated with an RF power meter by driving a known signal level into well terminated and unterminated loads to calibrate the forward voltage signal, reflected voltage signal, and to determine the cable line loss.

The transmitted signal calibration also relies on computer simulation results. In order to calibrate the signal level to the RF field level in the cavity, we use the relationships

$$Q = \omega \tau_{1/e} \tag{7}$$

$$U = P_{in} \tau_{1/e} \tag{8}$$

where Q is quality factor, U is stored energy, ω is frequency, P_{in} is power into the cavity, and $\tau_{1/e}$ is the time constant. With a known input power to the cavity (determined from measured forward and

reflected power signals) and a measured cavity Q, the stored energy in the cavity can be calculated. This stored energy can then be used along with the equations

$$\frac{V_{ACC}{}^2}{U\omega} = \frac{R_{SH}}{Q} = \frac{l_{eff}{}^2 E_{ACC}{}^2}{U\omega} \tag{9}$$

$$U = \frac{l_{eff}{}^2 E_{ACC}{}^2}{\omega\left(R/Q\right)} \tag{10}$$

$$\left(\frac{E_{ACC}}{E_{ACC=1MV/m}}\right)^2 = \left(\frac{U}{U_0}\right) \tag{11}$$

to calibrate the measured signal to a known stored energy, and then from the stored energy to a known field level. Here V_{ACC} is the accelerating voltage, R_{SH} is the shunt resistance, l_{eff} is the effective length of the cavity, and E_{ACC} is the accelerating electric field. The known field level requires the value of (R/Q), which is a geometrically determined value for the cavity taken from CST Microwave Studio. We define $E_{ACC=1MV/m}$ as 1 MV/m, and similarly define U_0 as the stored energy in the cavity at 1 MV/m.

We need a decay curve measurement to finish calibrating the signal level. One determines Q_L of the system by taking two measurements of signal voltage a known interval apart and fitting to Equation 12.

$$\tau_{energy} = \frac{\Delta t}{2\ln\left(\frac{V_1}{V_2}\right)} \tag{12}$$

where τ_{energy} is the time constant, V_1 and V_2 are measured voltage signals, and Δt is the time between measured data points. Q_L, the loaded Q, can be calculated from Equation 13.

$$Q_L = \omega\tau_{energy} \tag{13}$$

This time constant is the 1/e decay time of the energy in the system, so if one is measuring a voltage the time constant will be half that of the decay time of the energy ($\tau_{voltage} = 2\tau_{energy}$), since energy scales with

the electric field strength squared ($U \propto E^2$). Q_0, the intrinsic Q of the cavity, can be determined from Equation 14, which requires the coupling strength β.

$$Q_0 = (1 + \beta) Q_L \tag{14}$$

Q_0 is twice Q_L at critical coupling (ß = 1), and

$$Q_0 = \omega \tau_{\text{voltage}} \tag{15}$$

From the loaded Q one can determine the intrinsic Q of the cavity if the coupling strength of the forward power coupler is known. With a movable coupler it is best to position it to be critically coupled as it removes the need to calculate the coupling strength, one of the larger error sources. The WiFEL cryostat allowed for some manual movement of the coupler, but it was not easy to change the coupling strength while testing the cavity as the range of motion (approximately +/- 1 cm) was limited.

The coupling can be calculated from the measured forward and reflected power signals. This measurement can be done both in steady state as well as pulsed RF modes. For the CW case, the coupling can be calculated with Equation 16

$$\beta = \frac{1 \pm \sqrt{P_r / P_f}}{1 \mp \sqrt{P_r / P_f}} \tag{16}$$

where P_r is the reflected power and P_f is the forward power. In both the over- and under-coupled cases, the CW measurements become less accurate as P_r becomes exceedingly close to P_f and difficult to accurately measure. One must also know if the cavity is over- or under-coupled.

Another measurement approach uses P_e, the power emitted from the cavity, as measured by looking at the “reflected” signal immediately after the forward power is removed. The coupling strength can be determined by Equation 17.

$$\beta = \frac{1}{2\sqrt{P_f / P_e} - 1} \tag{17}$$

A strongly over-coupled system has $P_e = 4P_f$, so a large spike will appear immediately after the forward power is removed. For a very under-coupled system the emitted power will be essentially zero. This method of measurement also provides a quick qualitative test to determine if the system is over- or under-coupled.

Multipacting

Multipacting is a phenomenon often seen while operating SRF cavities. It is a transient resonance condition met only for specific geometries and frequencies at specific RF field levels. Electrons must gain enough energy to yield secondary electrons upon impact rather than implanting into the bulk material, while also satisfying temporal and spatial resonance conditions. [13] This phenomenon is strongly dependent on the properties of the cavity surface and requires a secondary electron yield (SEY) coefficient (number of electrons released per incident strike) greater than one. Figure 20 shows a plot of the SEY coefficient for niobium.

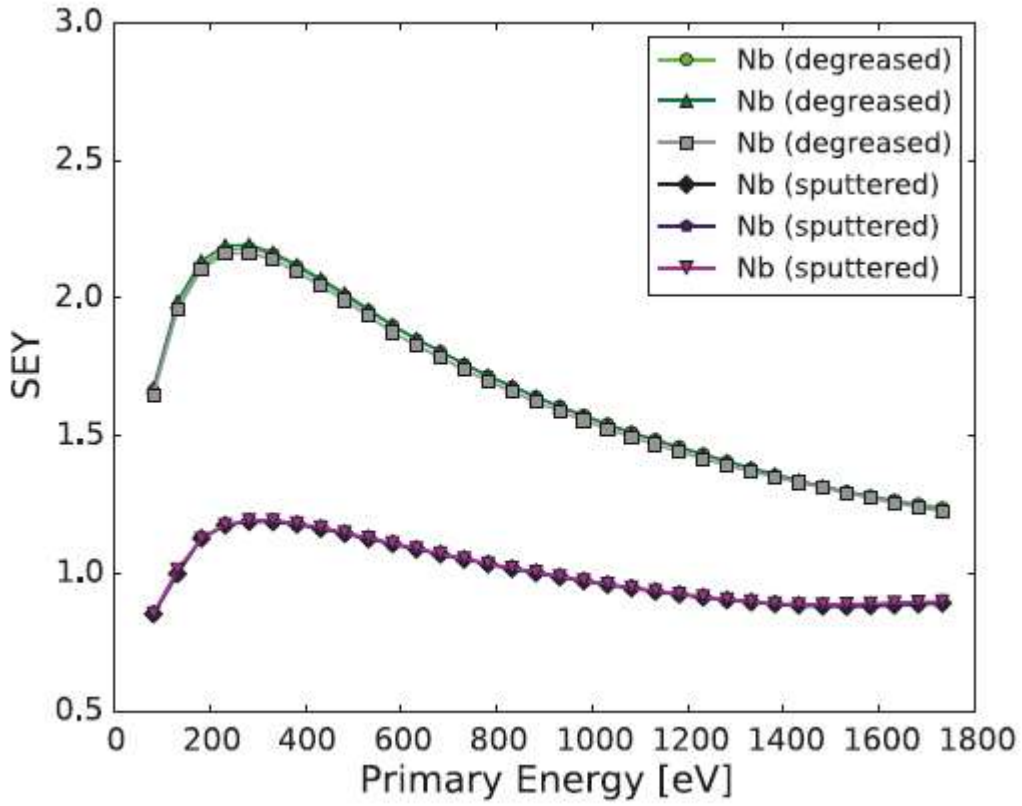

Figure 20. SEY vs incident electron energy for niobium. Peak value of SEY=2.2 was used as a worst-case scenario for simulations, a SEY of 1.5 to 1.8 is more likely realistic following standard cavity surface treatments. [14]

This issue is well known and documented for standard coaxial lines, which suffer mostly from two-point multipacting between the inner and outer conductors. The problem is not analytically solvable for complex cavity shapes, so CST Studio and its particle tracking capability is used to judge if a cavity will suffer from multipacting. Multipacting locations are determined by the cavity shape as well as the RF field distributions. Single-point (two point,…) multipacting occurs when a particle strikes the same single (two,…) point(s) and can be first/second order (or higher) depending on the number of RF cycles between strikes. Figure 21 shows multipacting in the WiFEL cavity.

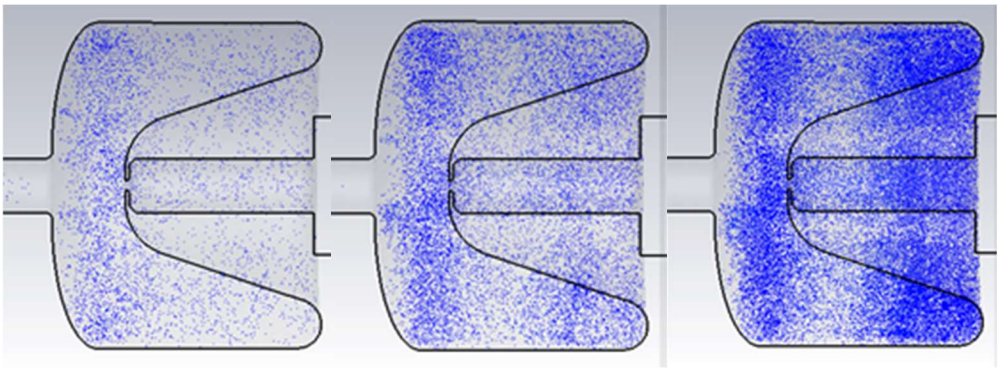

Figure 21. Progression of multipacting over tens of RF cycles at low field (tens of kilovolts) in a CST particle tracking simulation.

Multipacting is seen in almost all cavity geometries, with rounder corners helping to mitigate this resonance condition. Even with careful design multipacting can present a stubborn barrier to improved cavity performance. Once this secondary electron growth has started any additional power put into the cavity goes into multipacting. Multipacting can be overcome by pushing the forward power level beyond the barrier. Following cleaning and assembly the cavity surface will be covered with a monolayer of water, which has a much higher SEY value than niobium. Dumping additional power into this surface can release this water layer for relocation or pumping, lowering the SEY and allowing the cavity to reach a higher RF field level. This process can be quite slow, but eventually the field makes a discontinuous jump as this multipacting barrier is overcome.

Initial Cryostat Cooldown and investigation

Initial cold testing

The first cooldown at Argonne done toward the end of 2020 was the first time that the WiFEL cryomodule had been hooked up to a closed loop liquid helium refrigerator, allowing continuous operation at cryogenic temperatures. Figure 22 shows the cryostat in the test bunker both before and during cooldown.

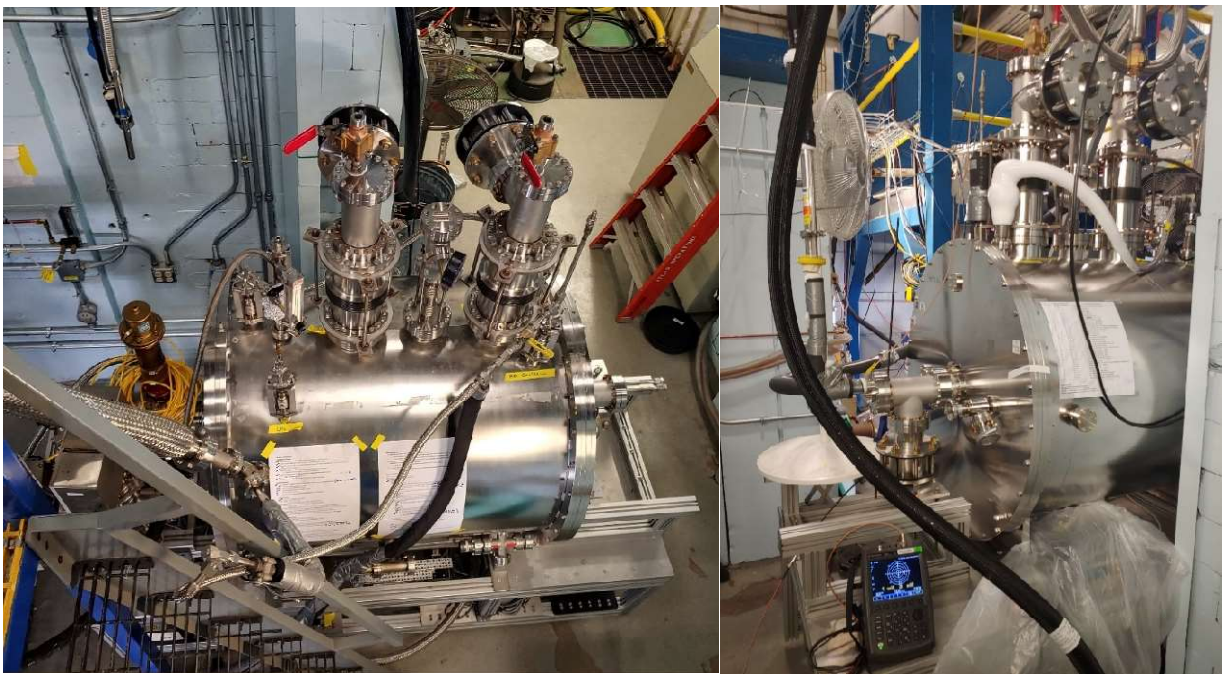

Figure 22. WiFEL cryomodule in test cave before connection to the liquid helium refrigerator (left). Cryostat in cave during cooldown, ice balls forming on helium connection lines (right).

The thermocouples distributed around the cryostat were kept intact for initial testing to verify how the system cooled down. The cavity was fitted with two cryogenic Gallium Aluminum Arsenide diode sensors, and two silicon diodes were dropped into the helium space for additional cryogenic readouts. Figure 23 shows the readout of these sensors over the course of two days. Data logging was unavailable for this test, which led to the large gaps in data points outside of work hours.

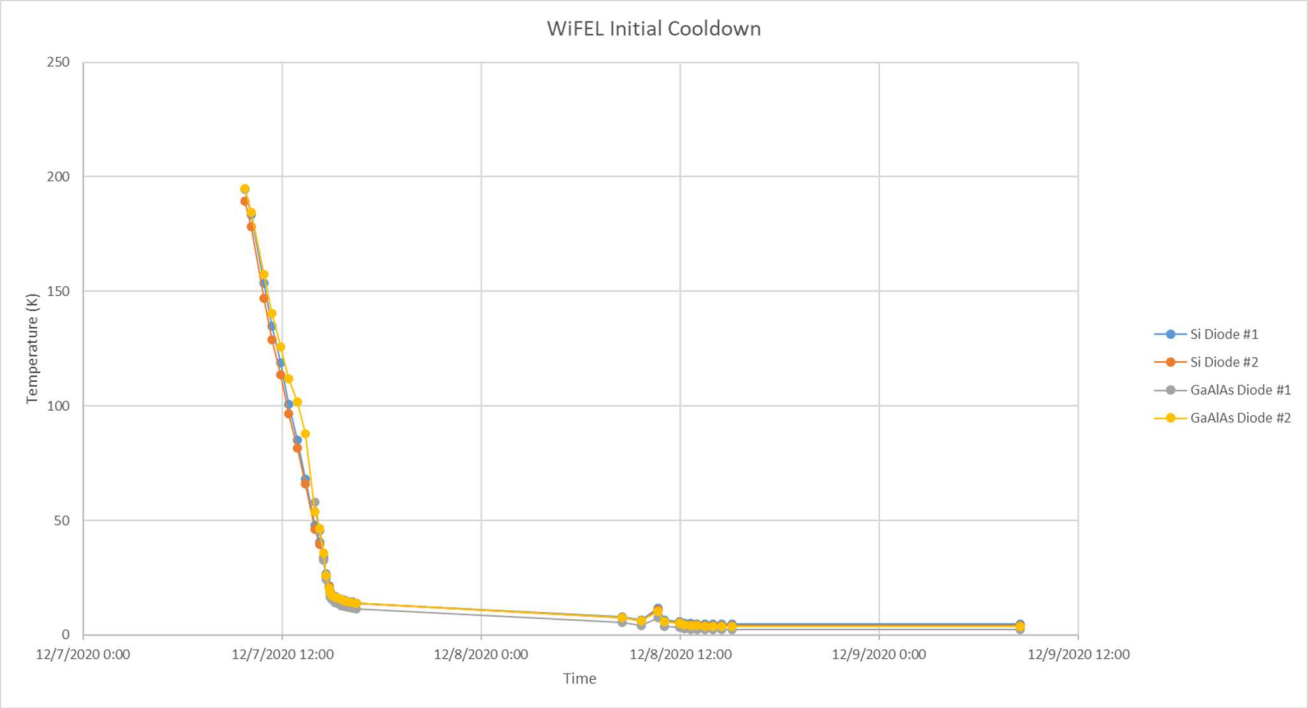

Figure 23. Cooldown over the course of multiple days.

Figure 24 shows the initial decay time measurement, which allows one to calculate the loaded quality factor (Q_L) of the cavity/coupler system. Along with the coupling strength of the coupler, the decay time provides the information needed to calculate the intrinsic quality factor (Q_0) of the cavity. The coupling strength of the power coupler can be calculated through direct RF power measurements. The coupling strength of the pickup probe can be experimentally measured, and then all RF measurements are done with known calibration.

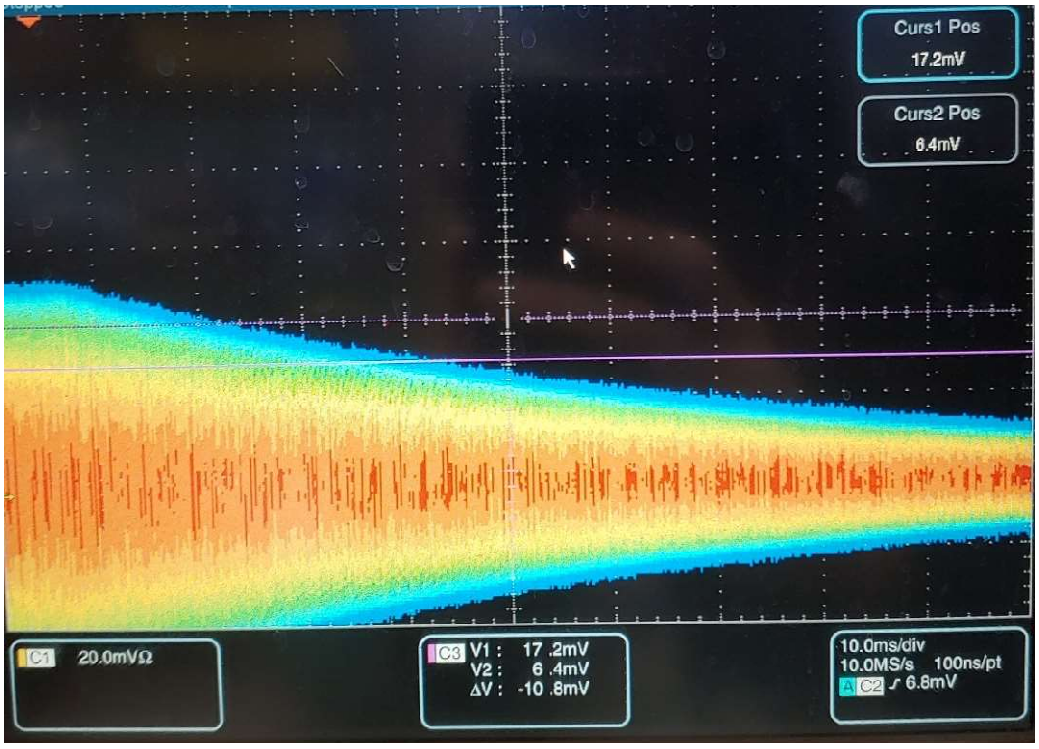

Figure 24. Decay time measurement looking at the RF signal from the pickup probe, indicating a lower Q than expected.

The order of magnitude of the power coupler coupling strength was known from previous CST Microwave Studio simulations (Q ~4 x 10^8) and directly measured later. The mechanical assembly of the power coupler allowed for approximately +/- 1 cm of travel from a neutral position, which allowed for some adjustment of the coupling strength. The first decay time measured was very short for the expected quality factor of the cavity, τ = 36 ms. The calculated Q_L from this measurement was ~4 x 10^7, and since we knew that the power coupler quality factor was higher than this figure, the intrinsic quality factor of the cavity was much lower than originally expected. This follows from knowing how the quality factors of the system are related, given in Equation 18.

$$\frac{1}{Q_L} = \frac{1}{Q_0} + \frac{1}{Q_{ext}} \tag{18}$$

The reflected RF power signal during pulsed operation was also measured. Figure 25 shows the qualitative shapes of under-, critically-, and over-coupled systems. Figure 26 shows that we did not see

the large voltage spike after the RF turns off expected for the over-coupled case as we would have expected with the assumed Q_0 ~ 10^9 and Q_{ext} ~ 4 x 10^8. The coupler was under-coupled and Q_0 was ~10^7.

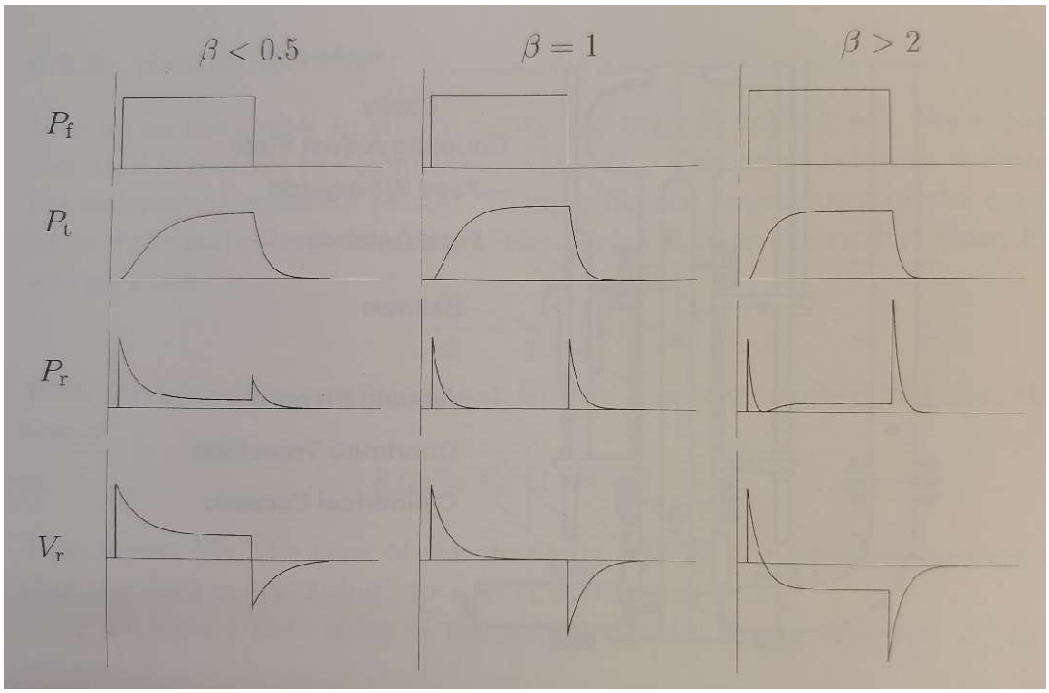

Figure 25. Characteristic shapes of measured RF signal for under-, critically-, and over-coupled states of a resonant system. [2]

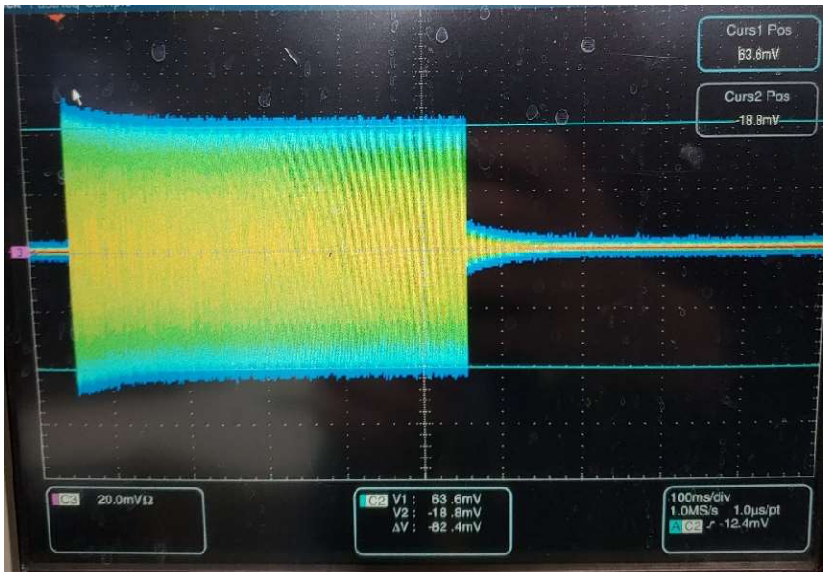

Figure 26. Reflected RF power signal during pulsed operation, indicating the coupler is in an under-coupled state.

CST simulations

In view of the bellows failure that vented the RF space during transit, we suspected contamination inside of the cavity as the cause of the low Q. CST Microwave Studio simulations investigated multiple scenarios that could cause such a loss. We checked if the probe could possibly be inserted into the cavity too far to cause extra loss on the surface of the probe support structure, which was fabricated from stainless steel, much more lossy than the copper probe. Simulation results are shown for the probe in the designed spot 1.5" back from flush with the cavity (Figure 27), as well as flush with the cavity face (Figure 28) and inserted into the cavity by 1" (Figure 29).

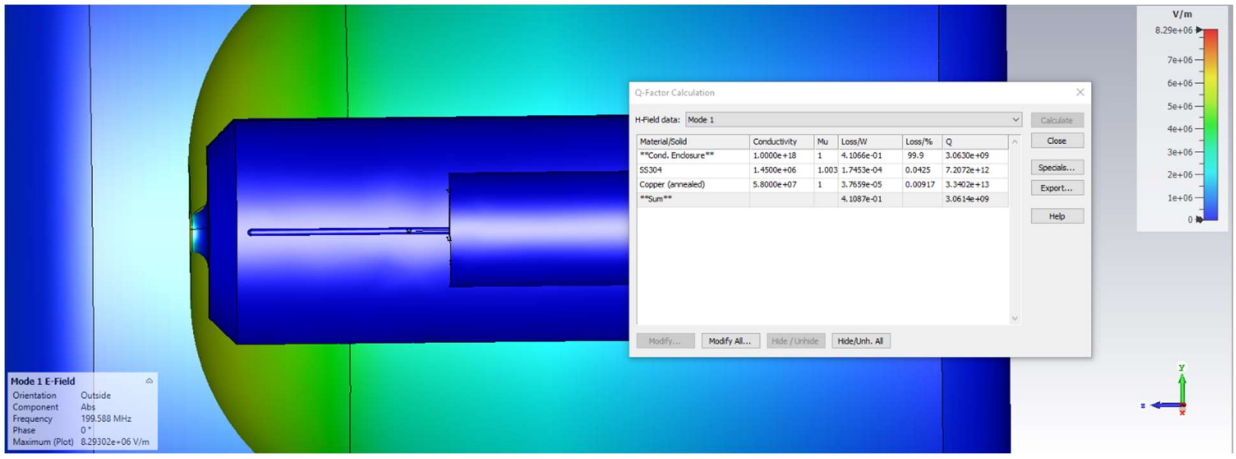

Figure 27. CST simulation of RF pickup probe in correct spot, $Q_L = 3 \times 10^9$.

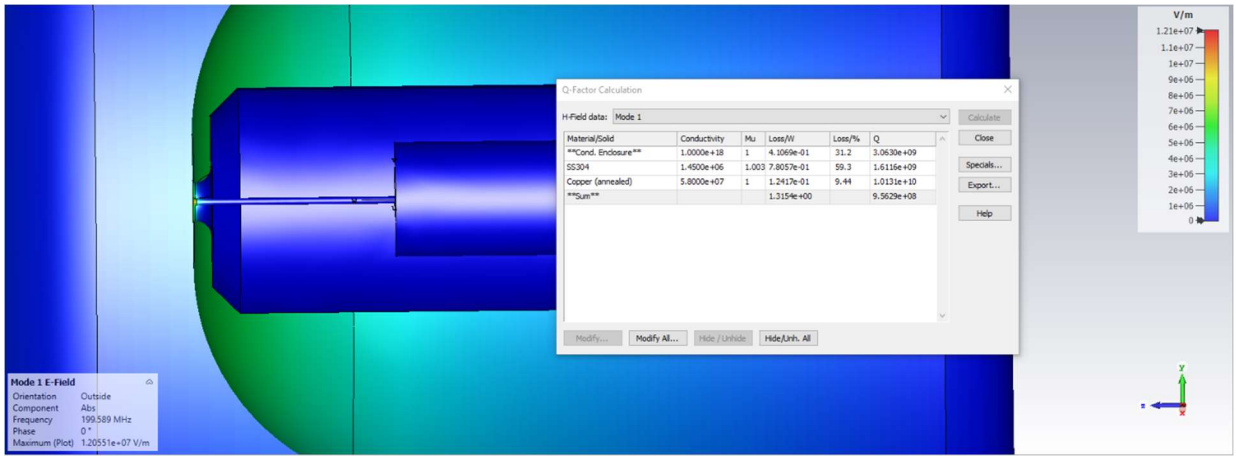

Figure 28. CST simulation of RF pickup probe flush with the cavity surface, $Q_L = 9.6 \times 10^8$.

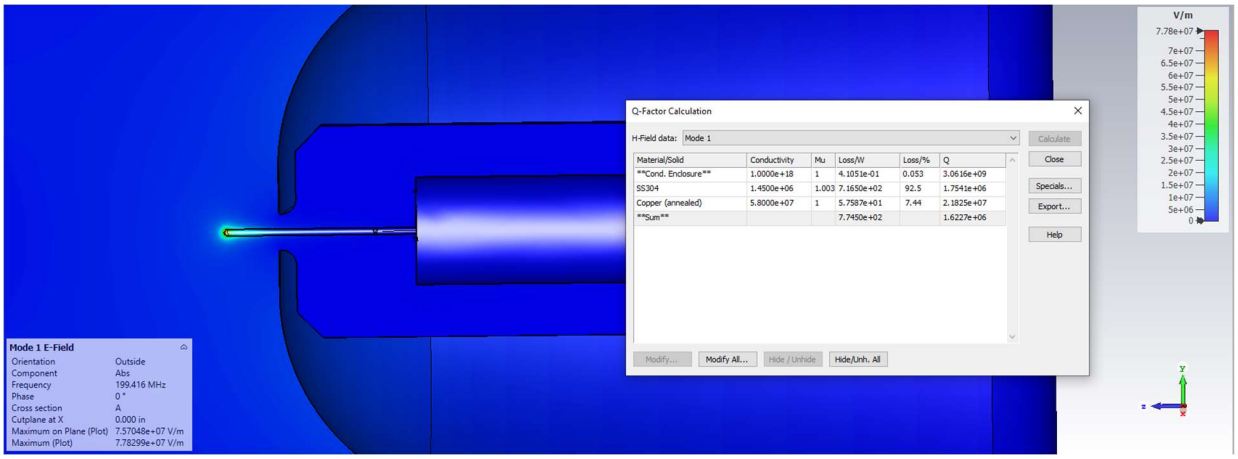

Figure 29. CST simulation of RF pickup probe 1" into cavity, $Q_L = 1.6 \times 10^6$.

These simulations required the probe to be inserted more than 2" further than expected to get the loaded quality factor we measured, which seemed unrealistic. Perhaps the RF probe support structure with copper heat shield/intercept inserted into the cavity could form another resonant structure that would couple power out of the system to lower the Q. Simulations showed this was also unlikely.

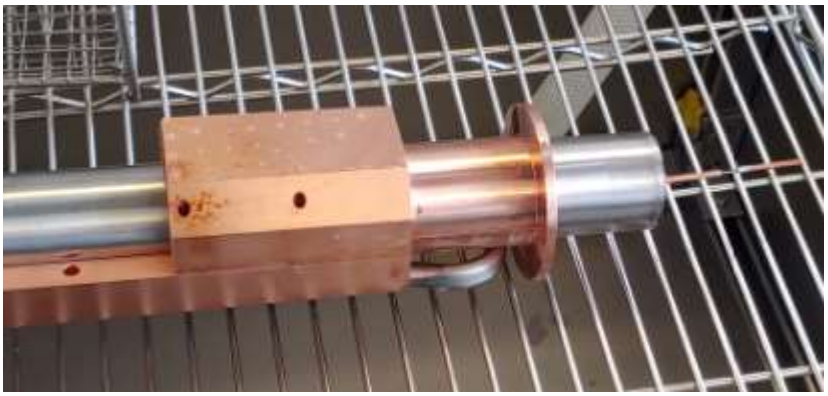

Figure 30. Close-up of RF pickup structure with potentially suspect features.

CST was used to determine whether a metallic or dielectric particle could feasibly lower the Q to our measured value and what particle size would be required. Perhaps particles could have been dragged into the RF space during the vent to lower the Q.

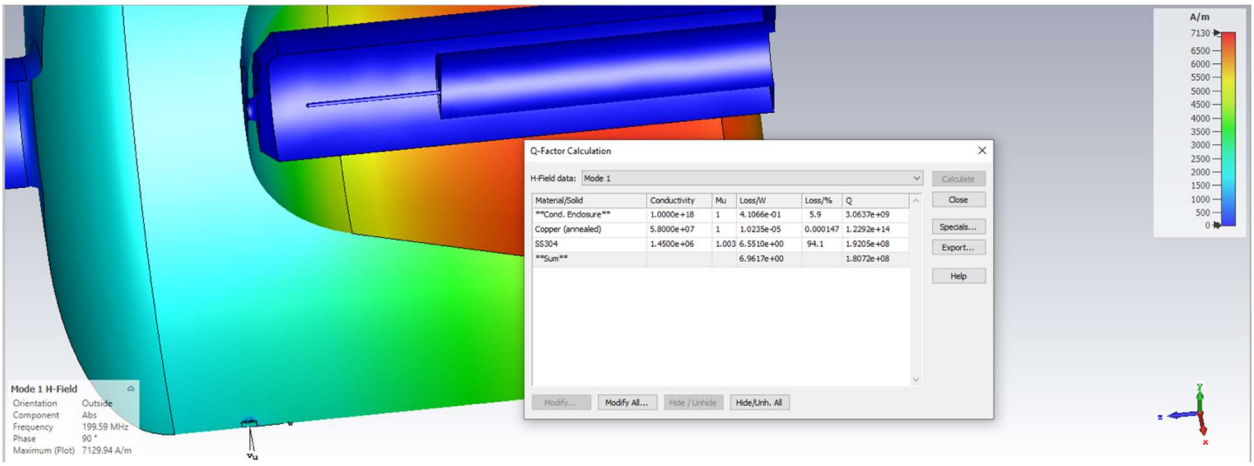

Figure 31. CST simulation of stainless steel "shrapnel" 1cmx1cm in low H-field region, $Q_L = 1.8 \times 10^8$.

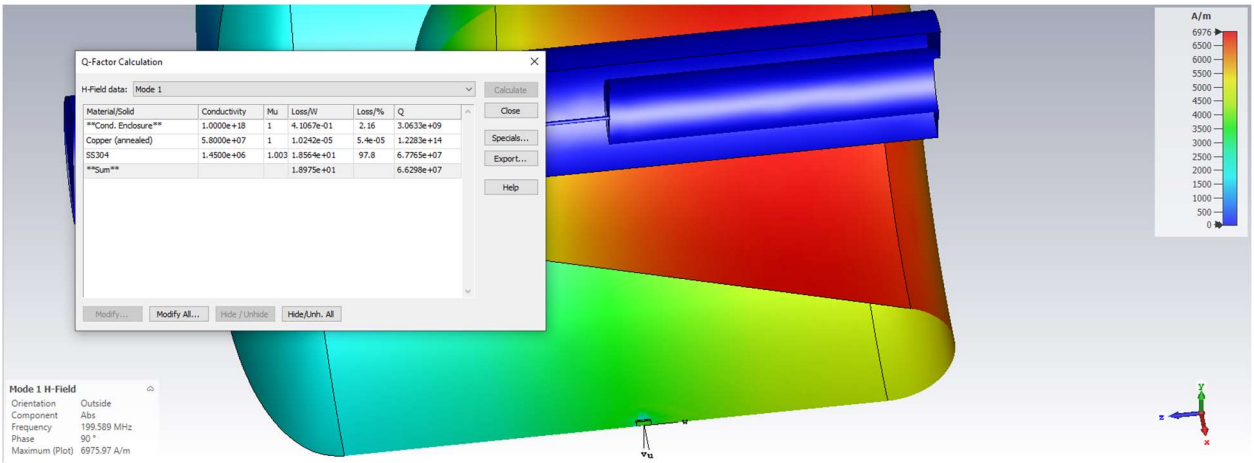

Figure 32. CST simulation of stainless steel "shrapnel" 1cmx1cm in mid H-field region, $Q_L = 6.6 \times 10^7$.

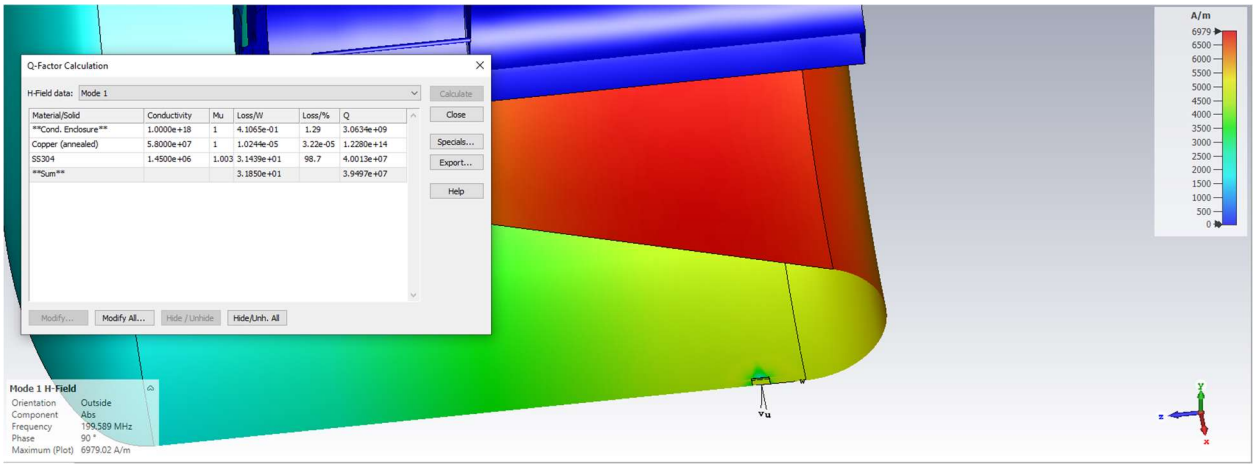

Figure 33. CST simulation of stainless steel "shrapnel" 1cmx1cm in high H-field region, $Q_L = 4 \times 10^7$.

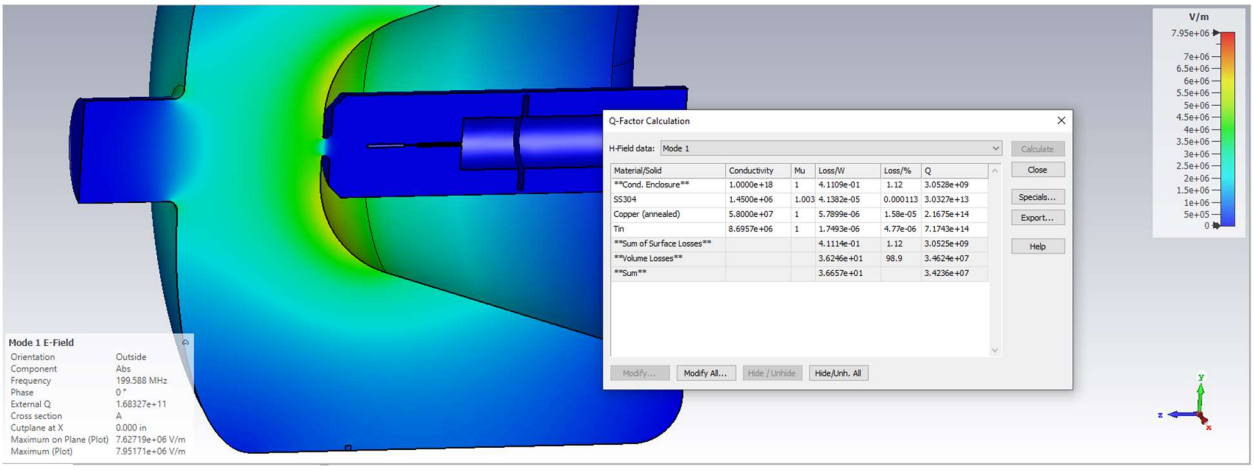

Figure 34. CST simulation of dielectric "shrapnel" 0.5cmx0.5cmx0.5cm, $Q_L = 3.4 \times 10^7$.

These simulations showed that it would be feasible for a particle (or collection of particles), either metallic or dielectric, to lower the quality factor of the cavity to the level that was measured, but only if they were large enough to be visible.

Borescope investigation

We decided to see if the cavity contained such visible contamination, even though inserting anything into the cavity risks contamination of the SRF surface. We decided to vent the cavity vacuum space, remove the end port of the beamline, and insert a flexible borescope into this cavity. Figure 35 shows a section view with a red arrow detailing how the borescope was inserted.

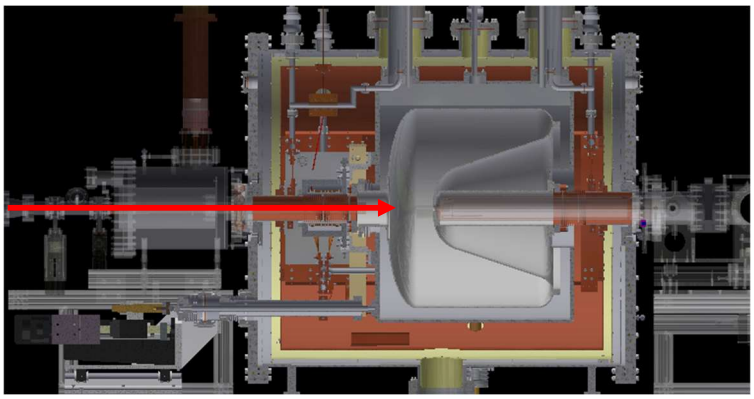

Figure 35. Section view of WiFEL cryostat, the flexible borescope was inserted from the left into the beamline and pushed into the SRF cavity.

Figure 36 shows the contamination on the bottom surface of the cavity in the form of particles of various size sub-millimeter to millimeter range, affectionately described as “moon rocks.”

Figure 36. Images of “moon rocks” taken from flexible borescope inserted into the WiFEL cavity.

This confirmation that the SRF surface was compromised prompted discussion about the potential benefits of disassembling, cleaning, and re-testing the cavity. Ultimately it was decided that WiFEL was worth refurbishing. The following figures show additional internal images (taken with a rigid borescope as well as simply looking into the bare cavity) of the contamination as well as some additional locations that this contamination was found.

Figure 37. Photograph of contamination on the bottom of the WiFEL SRF cavity (image taken looking into beamport).

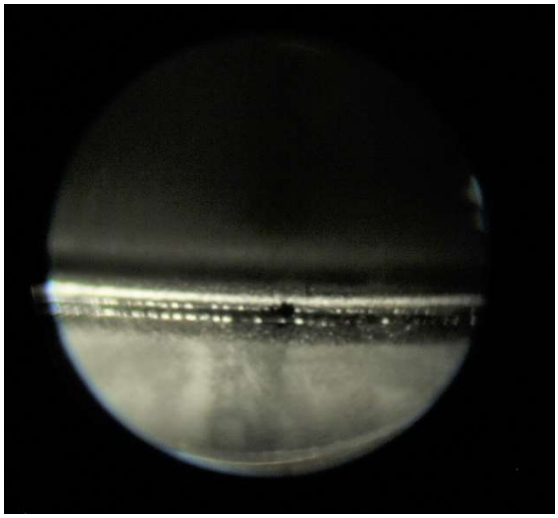

Figure 38. Image of a weld bead and contamination at the bottom of the cavity, taken through a rigid borescope.

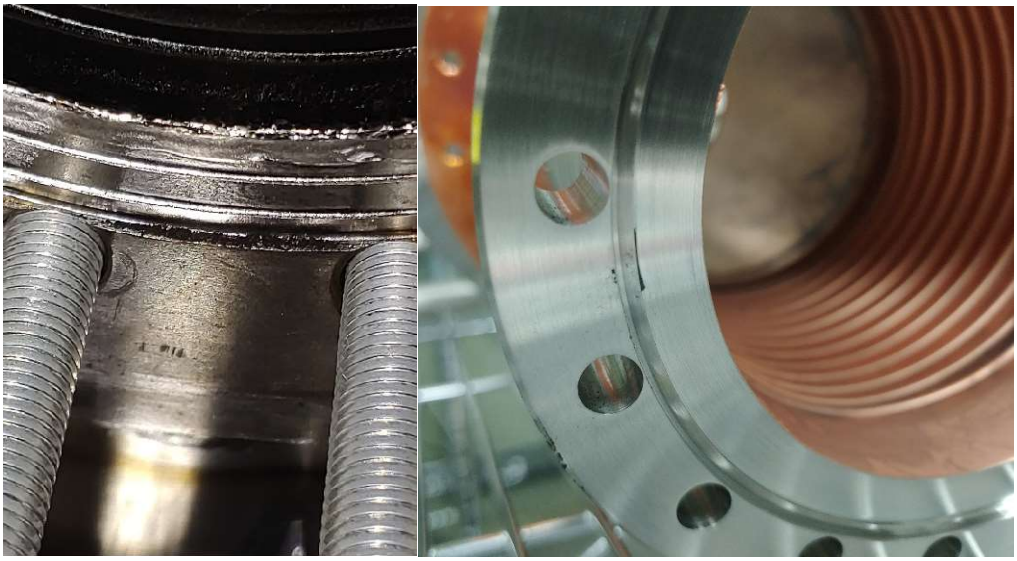

Figure 39. Additional contamination found on cathode stalk flange (and mating bellows)

Once the cavity was removed from the cryostat a small sample of the contamination was taken by swabbing the bottom of the cavity with a lint-free cleanroom wipe. This sample was sent to Argonne's analytical chemistry lab, which returned a result stating that the sample was principally niobium pentoxide.

There has been some speculation on the origin of this oxide, especially since the cavity had previously been tested and shown a much higher Q_0. The leading explanation is that this oxide may have formed during plasma processing done earlier to the cavity.

Disassembly and cleaning of the WiFEL cryostat

The cavity was removed, ultrasonically cleaned with soap and deionized ultrapure water, rinsed, then high pressure rinsed in a cleanroom. Reassembly of the cavity string was done as cleanly as possible, with critical stages of assembly being performed in a cleanroom. These processes are detailed extensively in Appendix C.

Second Cooldown Testing

The cryostat was moved back to the ADTF for cooldown and RF testing. We used a supplementary dewar to speed cryostat cooling (seen below in Figure 40), with the warm helium gas being fed back into the helium refrigerator. Figure 41 shows the thermometry readout over the course of the cooldown.

Figure 40. WiFEL cryostat in cave during cooldown post-cleaning. A helium dewar was used to help during the cooldown process.

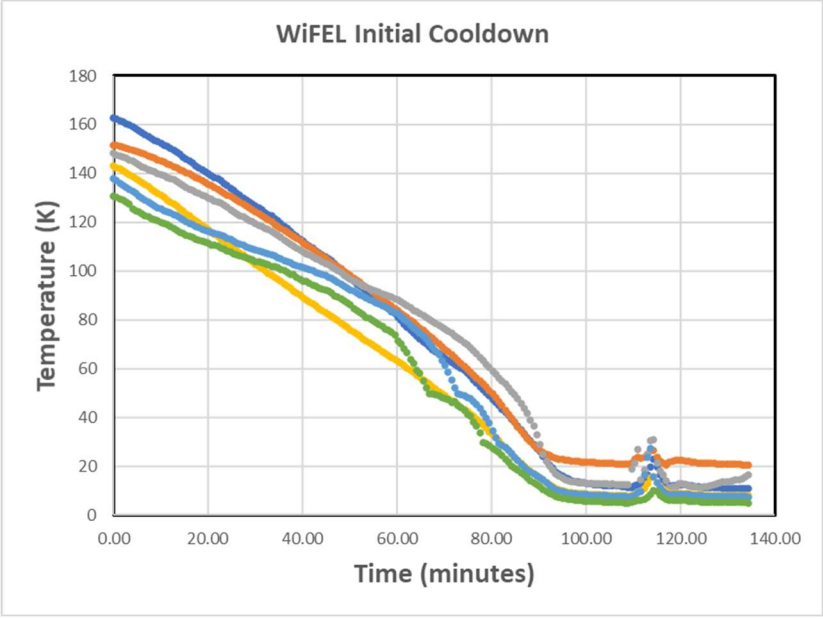

Figure 41. Silicon diode readout during first cooldown, time spent in hydride forming region (Q-disease region) is approximately 70 minutes.

RF Testing Results

The RF testing and calibration measurements were conducted as described above. These measurements account for all RF losses and give us accurate signal and power level calibrations. Once the phase locked loop had been properly set up and was locked to the cavity frequency, we began taking measurements. Initially the signal was simply generated by an RF signal generator (and not put through a power amplifier) since we wanted to drive the cavity with <1 watt power at first.

Multipacting

We ran into a multipacting barrier very quickly. Multipacting can be easily recognized: the field level stays constant while the forward power increases. There are many different types of multipacting barriers depending on the geometry of the cavity. A colleague and I performed extensive CST Microwave Studio simulations that match well with the multipacting barrier seen during testing. Empirical results showed a very broad, stubborn barrier starting at around a V_{ACC} of 8 kV and continuing until roughly 40 kV, in agreement with simulations. We decided to only condition the cavity while someone could watch to get data on the multipacting conditioning time and to ensure that the cavity would not "break through" the barrier and begin operating at an unpredictably high field level with no one present. Figure 42 shows a plot of the conditioning process, which took quite some time to complete. In addition a vacuum accident in our test setup during the Q measurements vented the cavity to atmosphere, thereby contaminating the cavity surface. The cavity had to be warmed up, pumped back out, and the multipacting conditioning at the same low field level was done again.

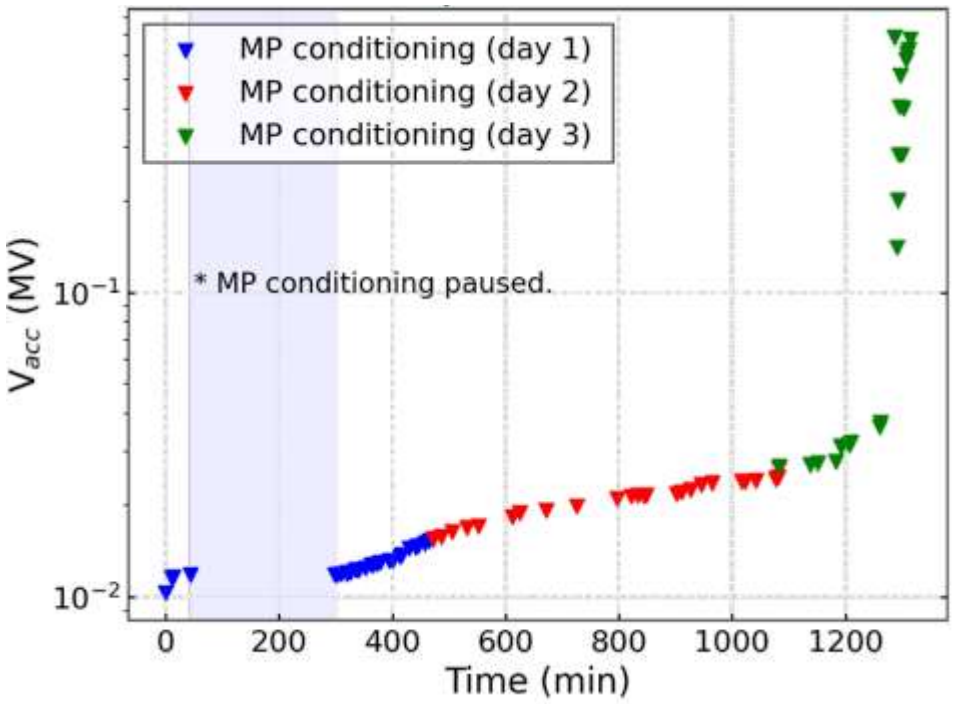

Figure 42. Plot of field level vs time, showing the gradual progress made as the multipacting barrier is conditioned through, with the sudden jump indicating the "break through."

After this initial conditioning multipacting was later only seen for a few seconds, consistent with the idea that this initial multipacting band broadly effects the center conductor and ends up cleaning the majority of the cavity surface so that additional multipacting bands were hardly noticeable. The cavity was then driven to a much higher field level, with the drive signal now being passed through a large power amplifier. The cavity eventually reached the point of field emission, either directly causing a fast breakdown or simply limiting the Q_L (as the forward power goes into generating x-rays instead of raising the field level). The cavity was driven with higher and higher power levels while recording the field level, forward power, and reflected power signal levels. With this information the coupling strength and the intrinsic quality factor (Q_0) can be calculated. The standard result for cold RF testing of SRF cavities is a so-called "Q curve." This plot gives the intrinsic quality factor of the cavity for a given field level, which is usually not a constant value.

Several rounds of RF conditioning were performed during the WiFEL cavity testing. One drives the cavity in a pulsed mode at low duty cycle at a much higher field level than can be sustained during continuous operation. The highest field achievable by the cavity in CW mode is usually noticeably higher after this treatment as it mitigates field emission sites by either destroying the field emitter or by moving the field emitter to a lower electric field region of the cavity.

Q-curve results

The Q-curve plot in Figure 43 shows testing results after multiple rounds of RF conditioning. Each round of RF conditioning helped to push the ultimate field level higher. A maximum field level of E_{peak} = 14.3 MV/m at steady state was reached, with a maximum E_{peak} = 24 MV/m during pulsed operation. The figure also shows the amount of field emission radiation detected during testing, which became the limiting factor for peak fields greater than 10 MV/m. Radiation was measured with a Ludlum Model 375-9 radiation monitor inside of the test bunker.

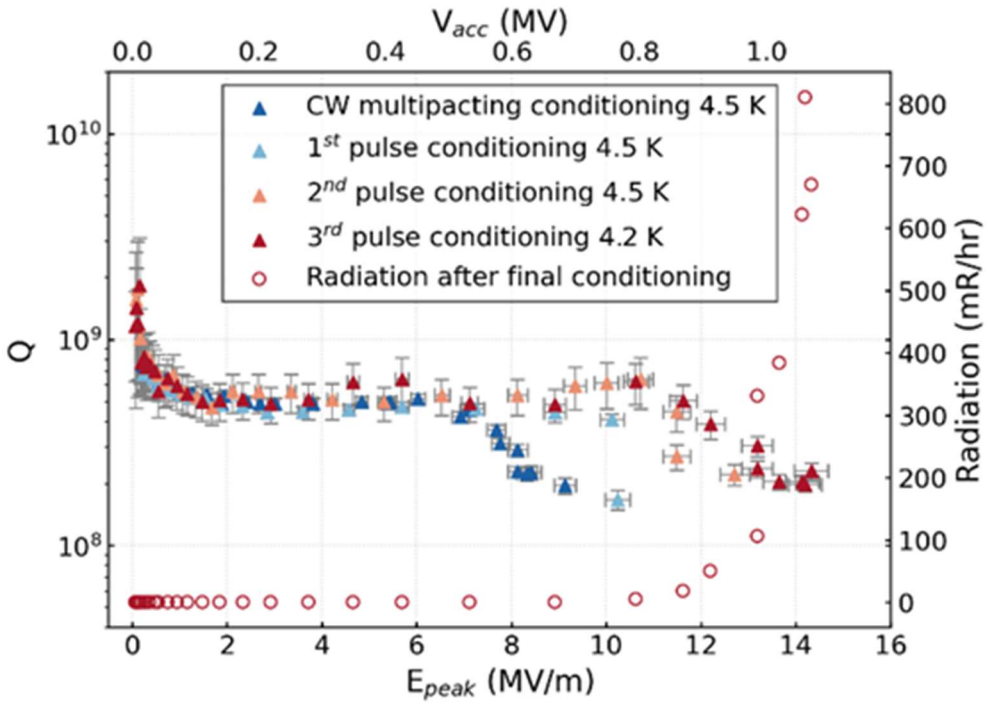

Figure 43. Q-curve plot of WiFEL cold testing results. Maximum CW field Epeak = 14.3 MV/m.

Additional Cold Testing

We also measured microphonics, Lorentz detuning, and the pressure sensitivity of the cavity frequency, exercised the mechanical tuner, and tested the cavity for Q-disease.

Microphonics

Microphonics are low frequency vibrational modes excited in cryostat operation through pumps or helium boiling [2]. Extensive initial design work is devoted to ensuring that the cryostat does not possess excessive microphonic noise. Cavity design can require stiffening of key components depending on the geometry. For a quarter wave resonator the dominant vibrational mode comes from the center conductor acting as a pendulum.

The cavity frequency is constantly being detuned from its nominal value from various sources: atmospheric pressure and helium system pressure changes, microphonics, and Lorentz detuning. Some of these changes are slow enough that they can be compensated through the mechanical tuner, which can handle long time scale changes on the order of seconds or more. The loaded Q of the system during operation is chosen to widen the bandwidth of the resonance enough that the cavity can still run in the presence of detuning microphonics modes. The cavity Q in an SRF system is usually in the range of 10^8-10^{10} depending on the geometry and beta the cavity is designed for. The loaded Q of the system is usually ~10^6 so that the power coupler is in the strongly over-coupled regime.

The microphonics of the system can be measured by analyzing the error signal in the phase locked loop. Very low frequency microphonics were observed while the cryostat was connected to the liquid helium refrigerator. Figure 44 shows the results of the microphonics measurements. These measurements are given as Fourier transforms (detailing frequency spectrum components of microphonics) and a probability distribution (detailing probability the cavity will be at a given frequency excursion).

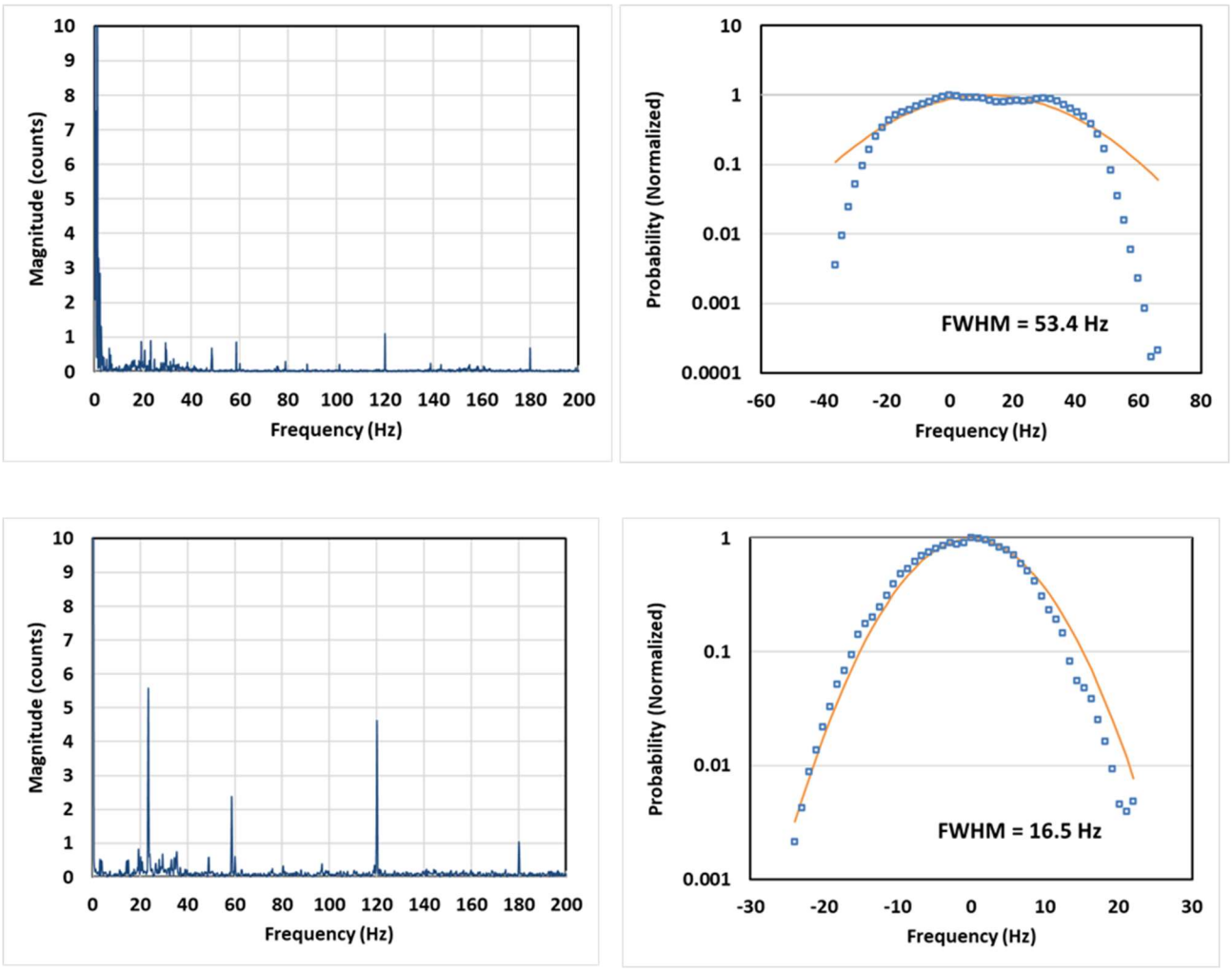

Figure 44. Microphonics data from the WiFEL cryostat. Top plots detail the frequency spectrum components (left) and probability density (right) of the cryostat while connected to the liquid helium refrigerator, the bottom plots provide the same data for the cryostat isolated from the refrigerator. The orange curves are Gaussian fits.

Pressure sensitivity df/dp

The detuning caused by a change in the helium system pressure, df/dp, determines the amount of frequency deviation one can expect from a change in the helium pressure. Figure 45 shows our df/dp measurement. The discontinuities seen in the data come from changing parameters of the phase locked loop during operation and are not physical. df/dp = 35.2 Hz/Torr for our system.

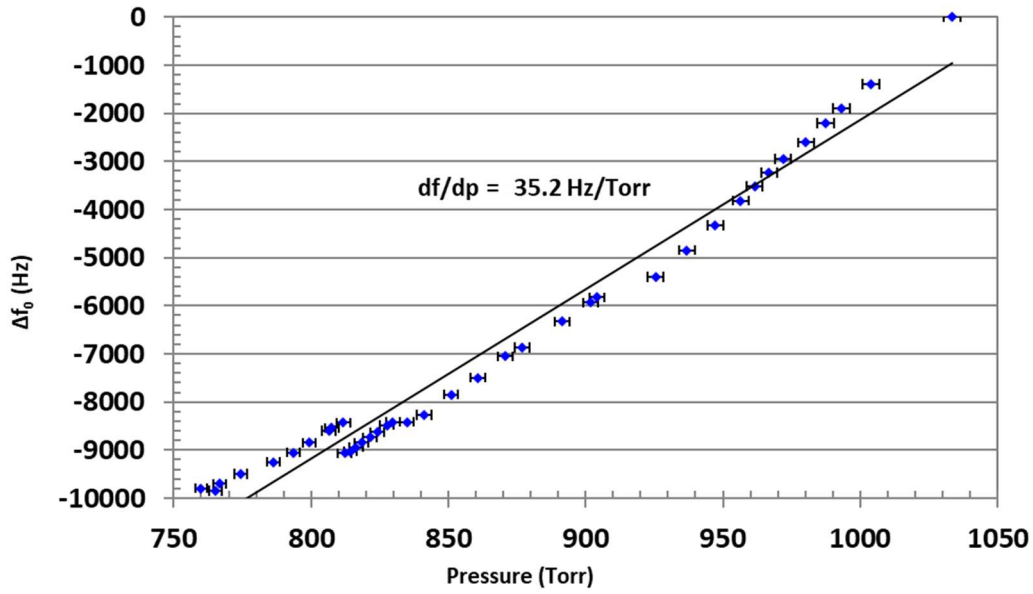

Figure 45. Measurement data for characterizing df/dp for the WiFEL cavity.

Lorentz Detuning

Lorentz detuning is the frequency shift that comes directly from the Lorentz force generated between the cavity magnetic field and the current flowing in the cavity walls, which distorts the cavity shape enough to affect its frequency. The radiation pressure (P_L) scales as shown in Equation 17

$$P_L \propto \mu_0 H^2 - \varepsilon_0 E^2 \tag{17}$$

where μ_0 is the vacuum permeability, H is the magnetic field, ε_0 is the vacuum permittivity, and E is the electric field [2]. Since the pressure scales with the square of the field, this sort of detuning force becomes more important at higher fields. We recorded the frequency change while switching between a low and high RF field level and separated helium pressure detuning from the Lorentz detuning with our measured df/dp. This measurement process was not automated, and therefore human error is expected to be significant. Still the calculated Lorentz detuning was quite similar to other quarter wave cavities previously tested by the Accelerator Development Group.

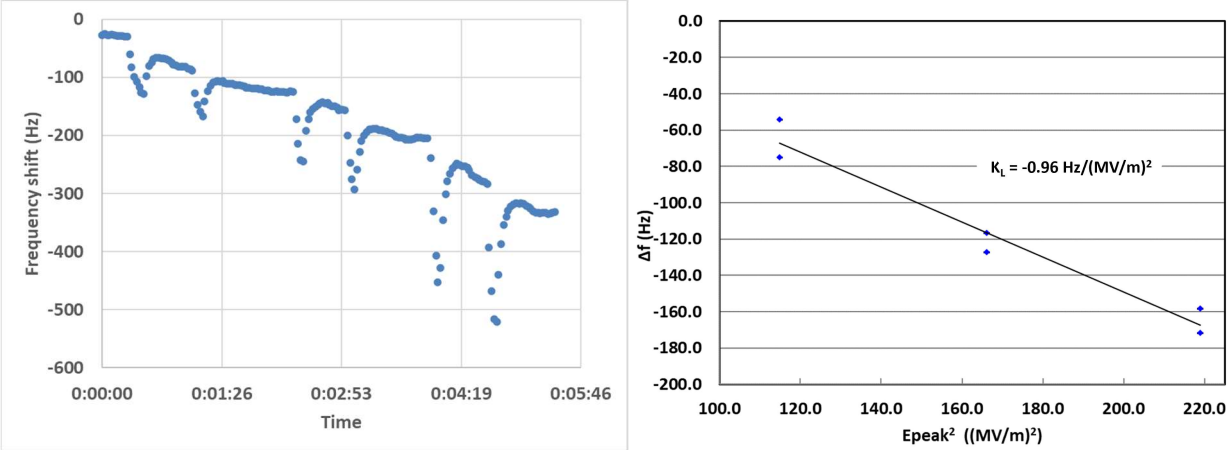

Figure 46. Frequency shift as the cavity is tested at three field levels, with larger frequency changes at higher field levels, two data points for each level. Calculated Lorentz detuning sensitivity was found to be 0.96 Hz/(MV/m)^2.

Q disease testing

So-called "Q disease" can lower the cavity Q as the field increases in proportion to how long the cavity spent in the hydride forming temperature range during cooldown. It is caused by hydrides forming in the SRF surface, which act as pinning sites for magnetic flux. Trapped magnetic flux increases residual resistance and lowers the performance of the cavity. These hydrides are known to form in a specific temperature region (approximately 50-150 K) if the surface is contaminated with hydrogen. [15] Figure 47 shows the phenomenon. Q-disease can be addressed by degassing the cavity surface in a 600° C bake or by spending a very limited amount of time in this hydride forming region with a fast cooldown.

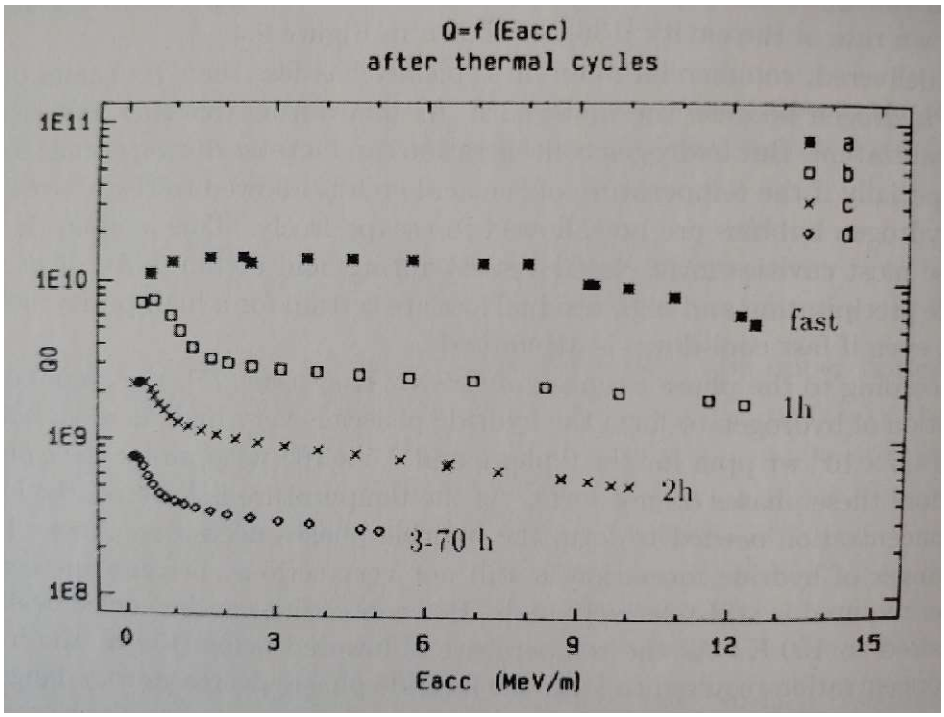

Figure 47. Q curves for a cavity cooled at various rates. Note the increasingly steep drop off in cavity performance for the 1 hour+ cases, a characteristic of "Q-disease." [2]

The WiFEL Q curve (Figure 43) might appear to suffer from Q-disease. We tested this hypothesis by warming the cavity to spend an extended period of time in the hydride forming temperature region. Figure 48 and Figure 49 detail the cooldown process and measured results. While there is some modest cavity performance improvement for the fast cooldown, one would expect the difference to be an order of magnitude or more if the cavity did suffer from Q disease. We concluded that the cavity did not suffer from hydrogen contamination. Similar low field drop off in performance has been attributed to other causes such as surface imperfections from a lossy weld.

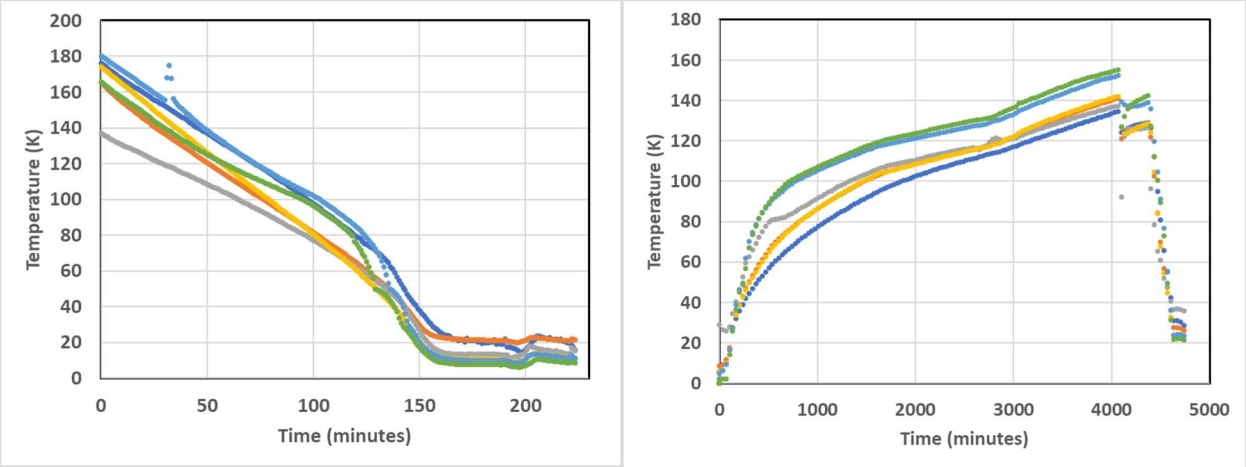

Figure 48. Cooldown rates for two cases used to test whether WiFEL had "Q-disease." The faster cooldown stayed in the hydride forming region for ~75 minutes while the slow cooldown held it in this region for 2+ days.

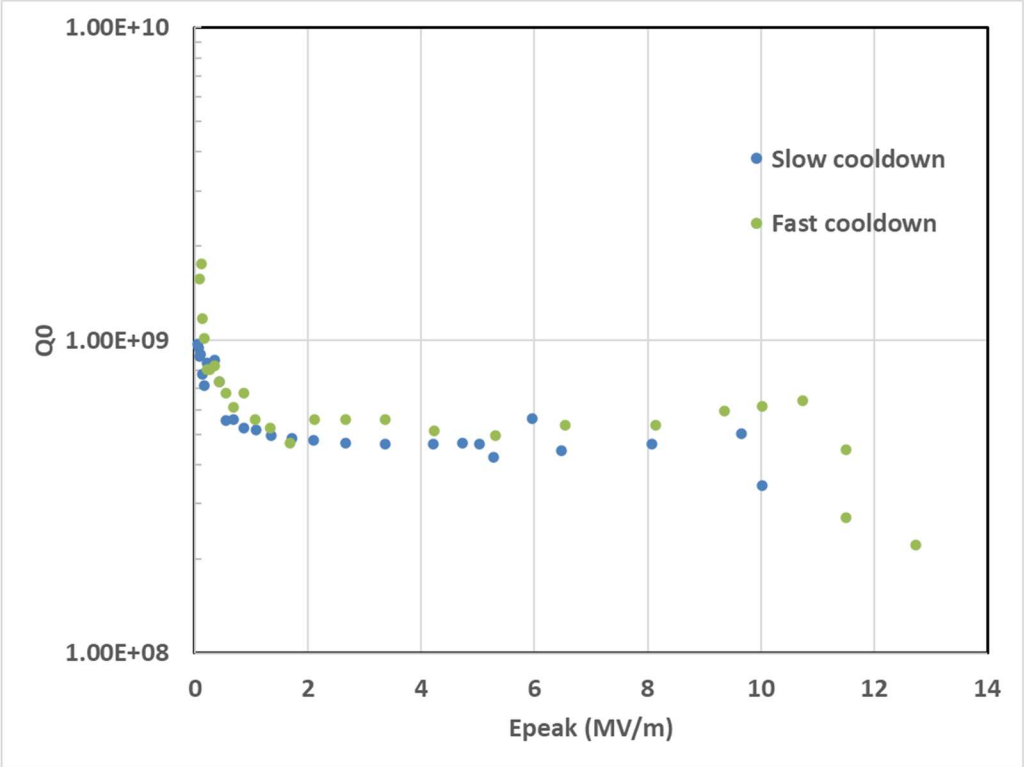

Figure 49. Comparison of Q curves for "fast" and slow cooldown rates.

Exercising mechanical tuner

We exercise the mechanical tuner which is used to compensate for larger, but slower, frequency shifts the cavity experiences. The mechanical tuner used on the WiFEL cavity is a lever style tuner that applies force to the beamport side flange. Figure 50 shows the design of this tuner structure, a rod running coaxially to the bottom tube which threads into the helium jacket and allows force to be applied only between the rod and tube.

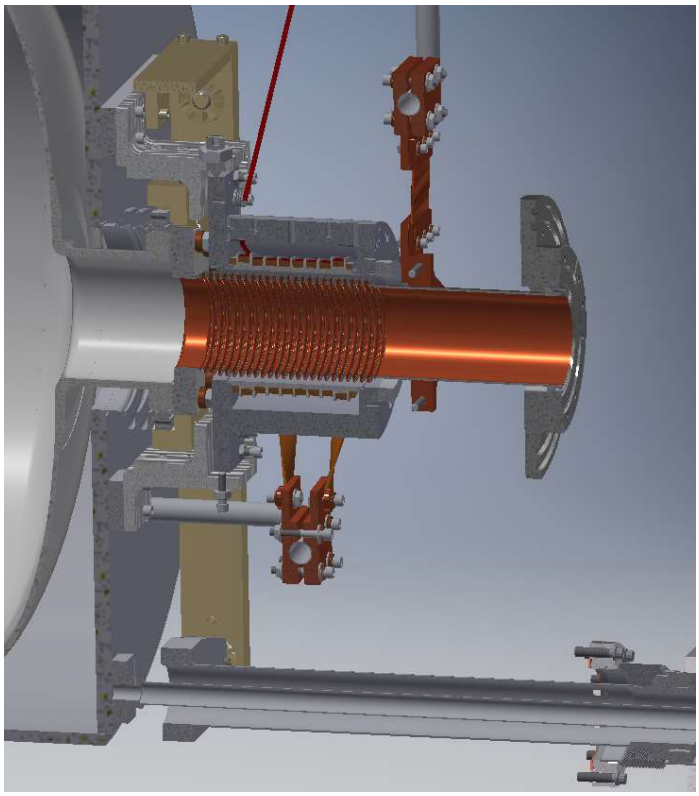

Figure 50. Half-section view of the WiFEL mechanical tuner setup, which applies force to the cavity anode port to deform the cavity very slightly and change frequency.

The mechanical tuner was manually actuated with the force applied being read out by a load cell. Figure 51 shows a linear response under the tuner force loads tested.

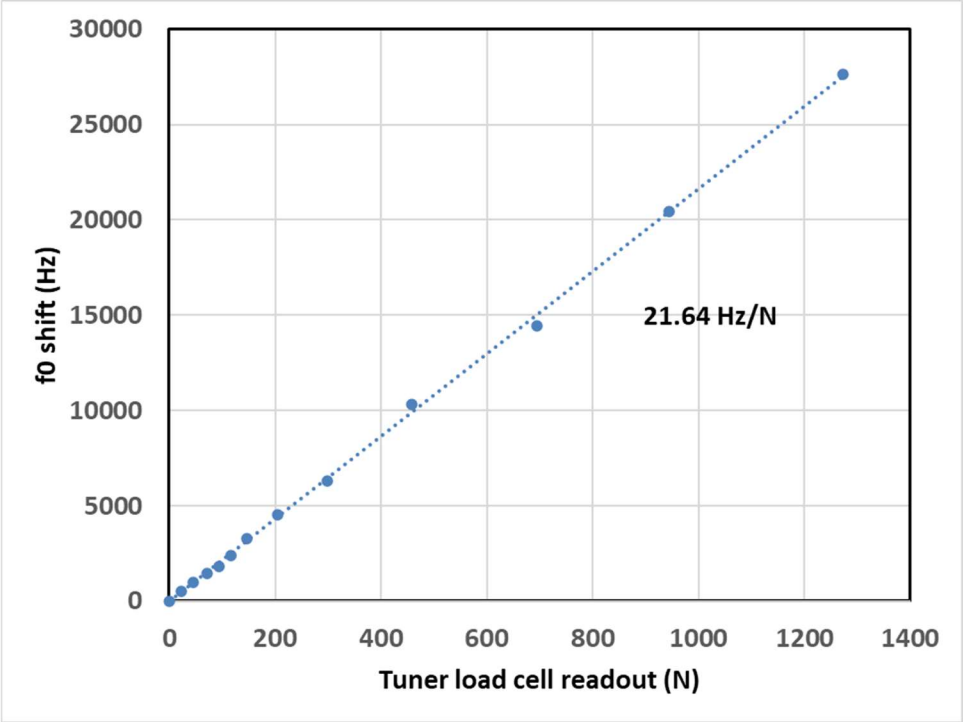

Figure 51. Mechanical tuner force vs cavity frequency shift.

Summary of Cold Testing

The RF testing was completed, and we considered the refurbishment of the WiFEL cavity to be a success. The measured Q of almost 10^9 was close to the expected value. The multiple vacuum incidents along with the field emission radiation at higher fields leads us to suspect that this cavity could achieve larger fields if it were cleaned again.

Future Work

With the cold testing of the WiFEL cavity completed, the question of what to do with the cryostat going forward remains. Our group has a few ideas of what could be done with it, as well as how the experience of testing (and simulating) WiFEL can and will be helpful for future electron guns. The WiFEL cryostat could be used as a testbed for one of the most complicated parts of an e-gun design, the cathode insertion device, which is difficult to design as it is meant to be inserted into the SRF cavity

space, an area that is necessarily free of particles. The WiFEL e-gun could become a source for an ultrafast electron diffraction/microscopy experiment (UED/UEM).

Our successful simulation of the WiFEL cavity properties can benefit future work. Many of the cavity properties (multipacting, RF field distribution, E_z field shape) are functions of the specific geometry and can be optimized through simulation.

Multipacting simulations

The robust dataset we collected on multipacting for the WiFEL measurements has since been used as a benchmark for our group for multipacting simulation. The WiFEL shape was imported into CST Microwave Studio to develop a multipacting model which was modified and fine-tuned to investigate the two regimes of multipacting: (1) low fields where the multipacting takes place near the dome, center conductor, or in between, (2) high fields near the toroid region of the cavity, where the RF field forms a null and the electrons tightly oscillate. The WiFEL cavity shape was used to validate the lower field, broader multipacting region that we saw experimentally. Our group has been involved in further design work for an SRF electron gun, and the WiFEL benchmark data has added confidence to our simulations of multipacting strength and cavity optimization to mitigate multipacting.

Summary

The WiFEL gun was originally designed and fabricated as a project at the University of Wisconsin. Our group received the WiFEL e-gun, modified the cryostat to connect to the liquid helium refrigerator, cold tested the e-gun, and investigated the source of the low quality factor of the cavity. The contamination was found to be a fine powder of niobium pentoxide on the bottom of the cavity. Removal of this contamination required total disassembly of the cryostat for proper cleaning, including ultrasonic cleaning and high-pressure rinsing.

We measured a reasonable quality factor of ~10^9 and were able to operate CW fields up to 15 MV/m after cavity refurbishment. We believe this field could be increased with a second round of cleaning. We performed many operationally important measurements, including multipacting conditioning, microphonics, and Lorentz detuning.

Bibliography

[1] Kelly, M. (2013). *TEM Class Cavity Design. SRF 2013*.

[2] Padamsee, H., Knobloch, J., & Hays, T. (2008). *RF superconductivity for accelerators*. Wiley-VCH.

[3] Tinkham, M. (2015). *Introduction to Superconductivity*. Dover Publications.

[4] Bardeen, J., Cooper, L. N., & Schrieffer, J. R. (1957). Theory of superconductivity. *Physical Review, 108*(5), 1175–1204. https://doi.org/10.1103/physrev.108.1175

[5] *Cooper pairs*. Cooper Pairs and the BCS Theory of Superconductivity. (n.d.). Retrieved November 12, 2022, from http://hyperphysics.phy-astr.gsu.edu/hbase/Solids/coop.html

[6] Padamsee, H. (2009). *RF Superconductivity: Science, Technology and Applications*. Wiley-VCH.

[7] Antoine, C. Z. (2014, December 4). *How to achieve the best SRF performance: (practical) limitations and possible solutions*. CERN Document Server. Retrieved November 12, 2022, from https://cds.cern.ch/record/1974053

[8] Singer, W., Ermakov, A., & Singer, X. (n.d.). *RRR-measurement techniques on high purity niobium.* Retrieved November 12, 2022, from https://bib-pubdb1.desy.de/record/91801/files/

[9] Grassellino, A., Romanenko, A., Sergatskov, D., Melnychuk, O., Trenikhina, Y., Crawford, A., Rowe, A., Wong, M., Khabiboulline, T., & Barkov, F. (2013). Nitrogen and argon doping of niobium for superconducting radio frequency cavities: A pathway to highly efficient accelerating structures. *Superconductor Science and Technology*, *26*(10), 102001. https://doi.org/10.1088/0953-2048/26/10/102001

[10] Posen, S., Romanenko, A., Grassellino, A., Melnychuk, O. S., & Sergatskov, D. A. (2020). Ultralow surface resistance via vacuum heat treatment of superconducting radio-frequency cavities. *Physical Review Applied*, *13*(1). https://doi.org/10.1103/physrevapplied.13.014024

[11] Mohsen, O. (2021). *Design And Optimization of Superconducting Radio-Frequency Electron Sources* (thesis).

[12] Niowave, Inc. (n.d.) *200 MHz Cavity Final Report.*

[13] Somersalo E., Ylä-Oijala P., Proch D. and Sarvas J., *Computational methods for analyzing electron multipacting in RF structures*, Part. Accel. 59 (1998) 107.

[14] Aull S., Junginger T., Knobloch J. and Neupert H. 2015. *Secondary electron yield of SRF materials* Proc. 17th Int. Conf. on RF Superconductivity (Whistler, Canada) p TUPB050

[15] Knobloch, J. (2003). The "Q disease" in superconducting niobium RF cavities. *AIP Conference Proceedings*. https://doi.org/10.1063/1.1597364

[16] Ha, G., Kim, K.-J., Power, J. G., Sun, Y., & Piot, P. (2022). Bunch shaping in electron linear accelerators. *Reviews of Modern Physics*, *94*(2). https://doi.org/10.1103/revmodphys.94.025006

[17] Raich, U. (n.d.). *Emittance Measurements*. *US Particle Accelerator School*. Retrieved from https://uspas.fnal.gov/materials/09UNM/Emittance.pdf.

[18] Minty, M. G., & Zimmermann, F. (2003). *Measurement and control of charged particle beams*. Springer Nature.

Appendix A - Pillbox mode derivation

Deriving the fundamental mode of a pillbox RF cavity begins with defining the boundary conditions. This derivation follows closely that of Padamsee [2]. We start with what the electromagnetic fields look like near the surface of a perfect conductor. By Maxwell's equations we know that immediately outside of a perfect conductor the electric field must be perpendicular to the surface while the magnetic field must be parallel to the surface:

$$\hat{n} \times \boldsymbol{E} = 0 \tag{1}$$

$$\hat{n} \cdot \boldsymbol{H} = 0 \tag{2}$$

We will then look at the case of an infinite waveguide before adding additional boundary conditions by "closing" the ends of the waveguide. Spatially- and time-varying fields can be expressed as:

$$\mathbf{E}(\mathbf{x}, \mathrm{t}) = \mathbf{E}(\rho, \varphi) e^{ikz - i\omega t} \tag{3}$$

$$\mathbf{H}(\mathbf{x}, \mathrm{t}) = \boldsymbol{H}(\rho, \varphi) e^{ikz - i\omega t} \tag{4}$$

Maxwell's equations give us the familiar wave equation:

$$\left(\nabla^2 - \frac{1}{\mathrm{c}^2}\frac{\partial^2}{\partial \mathrm{t}^2}\right)\begin{Bmatrix}\mathbf{E}\\ \mathbf{H}\end{Bmatrix} = 0 \tag{5}$$

Using the above equations gives us the following form on the wave equation:

$$\nabla_\perp^2 + \left(\frac{\omega^2}{c^2} - k^2\right)\begin{Bmatrix}\mathbf{E}\\ \mathbf{H}\end{Bmatrix} = 0 \tag{6}$$

It can be noted that E and H are independent of each other, and the boundary conditions can be written independently.

$$\mathrm{E_z}|_\mathrm{S} = 0 \tag{7}$$

$$\left.\frac{\partial \mathrm{H_Z}}{\partial n}\right|_{\mathrm{S}} = 0 \tag{8}$$

The separate boundary conditions, along with the fact that E and H are independent, allows for there to be independent modes existing in the same waveguide. These modes are classified by which field varies along the transverse dimension, so called Transverse Electric (TE) or Transverse Magnetic (TM) modes.

The next step in finding the analytical solution for a pillbox cavity mode is to add two boundary conditions to turn the waveguide into a cavity. The same boundary conditions enacted on the waveguide boundaries must now be applied to the end walls, which creates standing waves inside of the cavity. This can be seen by combining the forward and backward traveling waves to get:

$$\mathrm{E_Z}(\mathbf{x}, \mathrm{t}) = \psi(\rho, \Phi)\cos\left(\frac{\mathrm{p\pi z}}{\mathrm{d}}\right) e^{iwt} \tag{9}$$

$$\mathrm{H_Z}(\mathbf{x}, \mathrm{t}) = \psi(\rho, \Phi) sin\left(\frac{\mathrm{p\pi z}}{\mathrm{d}}\right) e^{iwt} \tag{10}$$

where p=0,1,2,3… and correspond to a fundamental mode and integer harmonics. Plugging these field expressions into the eigenvalue equation gives:

$$\left(\nabla_\perp^2 + \gamma_j^2\right)\psi(\rho, \Phi) = 0 \tag{11}$$

which shows that γ_j^2 is the jth eigenvalue. The transverse fields can also be calculated using the relationships:

$$\mathbf{E}_\perp = \pm\frac{ik}{\gamma^2}\boldsymbol{\nabla}_\perp E_z \tag{12}$$

$$\boldsymbol{H}_\perp = \pm\frac{ik}{\gamma^2}\boldsymbol{\nabla}_\perp H_z \tag{13}$$

Using these relationships, the field components for TE and TM modes are given as:

TE modes:

$$\mathbf{E}_{\perp} = -\frac{i\eta\omega_j}{c\gamma^2}\sin\left(\frac{p\pi z}{d}\right)\hat{z} \times \boldsymbol{\nabla}_{\perp}\psi(\rho,\Phi) \tag{14}$$

$$\mathbf{H}_{\perp} = \frac{p\pi}{d\gamma^2}\cos\left(\frac{p\pi z}{d}\right)\boldsymbol{\nabla}_{\perp}\psi(\rho,\Phi) \tag{15}$$

TM modes:

$$\mathbf{E}_{\perp} = -\frac{p\pi}{d\gamma^2}\sin\left(\frac{p\pi z}{d}\right)\boldsymbol{\nabla}_{\perp}\psi(\rho,\Phi) \tag{16}$$

$$\mathbf{H}_{\perp} = \frac{i\omega_j}{\eta c\gamma^2}\cos\left(\frac{p\pi z}{d}\right)\hat{z} \times \boldsymbol{\nabla}_{\perp}\psi(\rho,\Phi) \tag{17}$$

where eta, $\eta = \sqrt{\mu_0/\epsilon_0}$, is the impedance of free space. The pillbox cavity fields can be derived by applying the specific geometry of the cavity to these TM and TE mode equations. Consider a cylindrical pillbox cavity of radius R and length d. We will consider the lowest frequency TM mode, with an eigenmode solution given as a Bessel function:

$$E_Z = E_0 J_0\left(\frac{2.405\rho}{R}\right)e^{-i\omega t} \tag{18}$$

$$H_{\phi} = -i\frac{E_0}{\eta}J_1\left(\frac{2.405\rho}{R}\right)e^{-i\omega t} \tag{19}$$

The full set of TM modes can be derived from here. The TE modes are generally considered uninteresting as it does not support an electric field on the beam axis, and therefore cannot accelerate particles, or even be excited by passing beam. The field profiles of more complicated cavity designs are not easily expressed in analytical form, but the pillbox cavity serves to instruct the physicist on how to approach cavity design and field boundary conditions. In practical designs most quarter wave resonator shapes are optimized through iterative computer simulation.

Appendix B - RF Photocathode field shape effects

One of the properties of a QWR mentioned earlier was that of the E_z field shape. Here we show why on-axis axial electric field shape is of great importance to the e-gun beam physics, particularly the emittance of the beam. This derivation follows closely with [16]. We begin with a cylindrically symmetric RF photocathode cavity. The components of the EM fields are given below:

$$E_s = \left(E(s) - \frac{r^2}{4}\left(E''(s) - k^2 E(s)\right)\right) \tag{1}$$

$$E_r = -\frac{1}{2} r E'(s) \sin(\omega t) \tag{2}$$

$$B_\varphi = \frac{k}{2c} r E(s) \cos(\omega t) \tag{3}$$

where

$$E(s) = E_0 \theta(s) \cos(kz) \tag{4}$$

and Θ(s) describes a function to account for having the field level drop off drastically once the particle exits the cavity. This function is very close to a step function. From these EM field components one can see that the radial electric field is proportional to the spatial derivative of the RF field. The force felt by a particle in motion will be given by the Lorentz force:

$$\mathbf{F} = q(\mathbf{E} + v \times \mathbf{B}) \tag{5}$$

For the axially symmetric case that we are interested in, the transverse force felt by a particle is:

$$F_r = e\left(E_r - v_s B_\varphi\right) \tag{6}$$

From the previous equations it can be seen that E_r and B_ϕ depend on E(s), particularly that E_r is dependent on the derivative of E(s). This means that a larger derivative for the beam axis electric field, the larger the transverse kick that is seen by the beam. A large transverse kick will send the particle off

axis into a region where the linear expansion assumed in the electromagnetic field equation is no longer valid.

The emittance of a beam is a measure of the phase space area that the beam takes up in the position/momentum space, as well as being an indirect measure of brightness. The emittance is conserved if the forces experienced by the particles are linear. Large amplitude particles in the cavity will experience nonlinear forces that can result in emittance growth. Figure 52 shows a few typical transverse emittance plots.

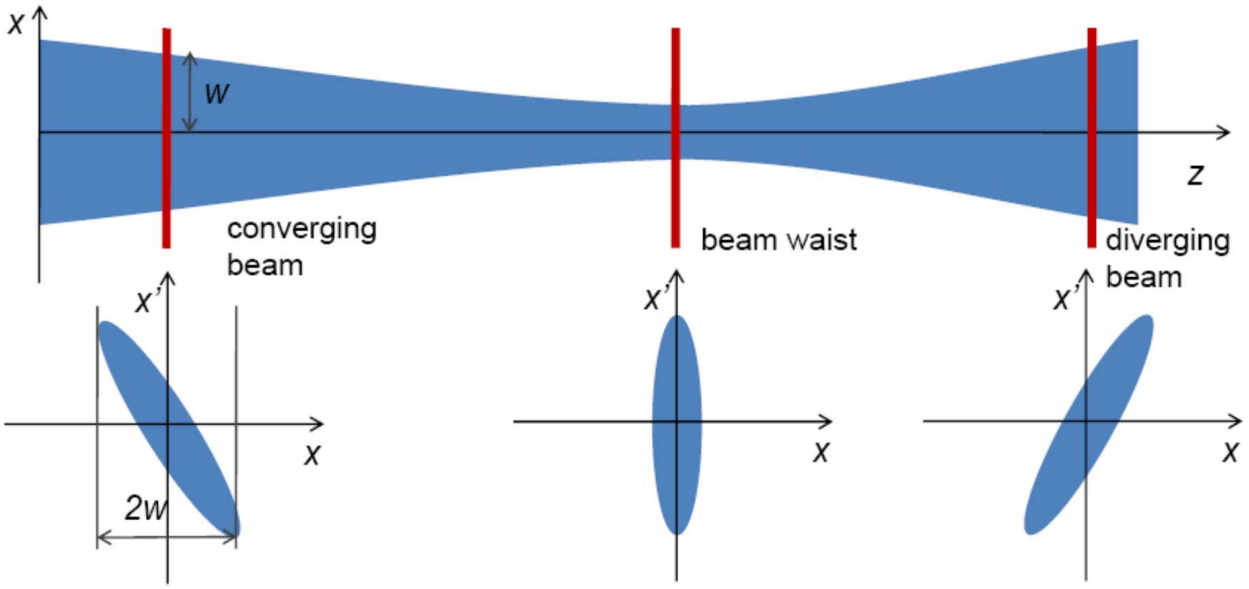

Figure 52. Transverse beam emittance plots showing various beam characteristics. [17]

A transverse force will expand the beam as it travels through the cavity. This force is normally counteracted by a solenoid field, but this becomes more difficult in a superconducting RF system as stray magnetic fields can have quite an adverse effect on the niobium cavity performance and the fields one can apply are therefore constrained.

If linear, this force preserves the emittance of the beam as the ellipse rotates in the phase space plot (but the area of the ellipse stays constant), as shown in Figure 52. It is the beam transverse size that

causes the large amplitude particles to be exposed to nonlinear components of the RF fields. It is through this mechanism that the emittance increases. If you can flatten the E_Z field profile then the emittance will be better preserved.

The longitudinal emittance is also of concern. Electrons are emitted from the cathode at different times throughout the RF cycle. This means that depending on when in the RF cycle the electron is released it will see a different field magnitude and will leave the cavity with a different energy. A large portion of the emittance will be dictated by the profile of the laser exciting the photocathode, since the temporal properties of the laser pulse will cause differing electron emission profiles; a longer laser pulse will cause a longer electron emission time, spreading the emission over a longer portion of the RF cycle. The laser profile also affects the space charge force felt by the particles, as a longer pulse will result in a lower charge density helping to mitigate space charge effects, albeit at the expense of lowering the peak current (a key figure of merit for FEL applications).

Figure 53 shows how electrons emitted at different phases of the electric field will gain different amounts of energy. A typical bunch length will span significantly less than 45°, but this illustrates the strong influence of the cos(ωt) term. This longitudinal energy spread increases the emittance. If emission is excited around the peak of the RF field this will cause some emittance growth. Emission phasing is optimized through particle tracking and is commonly selected to ensure maximum energy gain through the cavity.

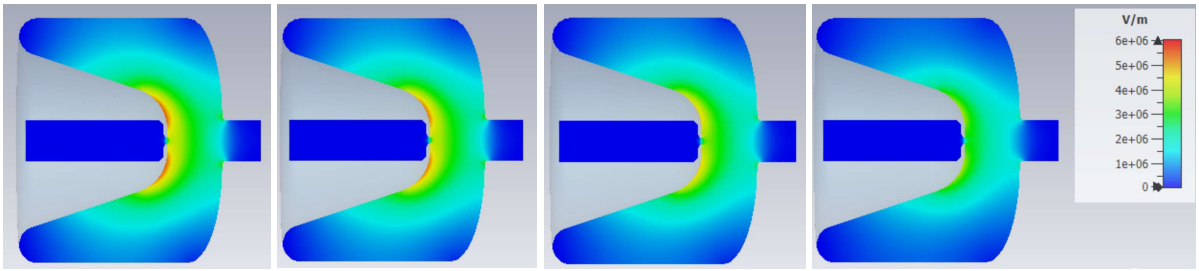

Figure 53. Electric field magnitude at RF phases 0°, 15°, 30°, and 45°

Decreasing the emittance results in a much higher brightness X-ray beam in a light source. [18] The beam brightness scales as the inverse square of the transverse emittance.

Figures 54 and 55 show the relevant WiFEL cavity field profiles which contribute to the transverse force seen by the beam and therefore to the emittance growth. Figure 56 shows the field profile for E_Θ, which is almost completely cancelled. All these plots show the fields at 1 mm from the beamline, with 6 varying azimuthal angles plotted. The plots show little variance in azimuth indicating a very symmetric cavity.

Figure 57 shows E_z, the main accelerating field of the cavity. This profile is reasonably flat in the region near the cathode, leading to the emittance preservation discussed in this Appendix.

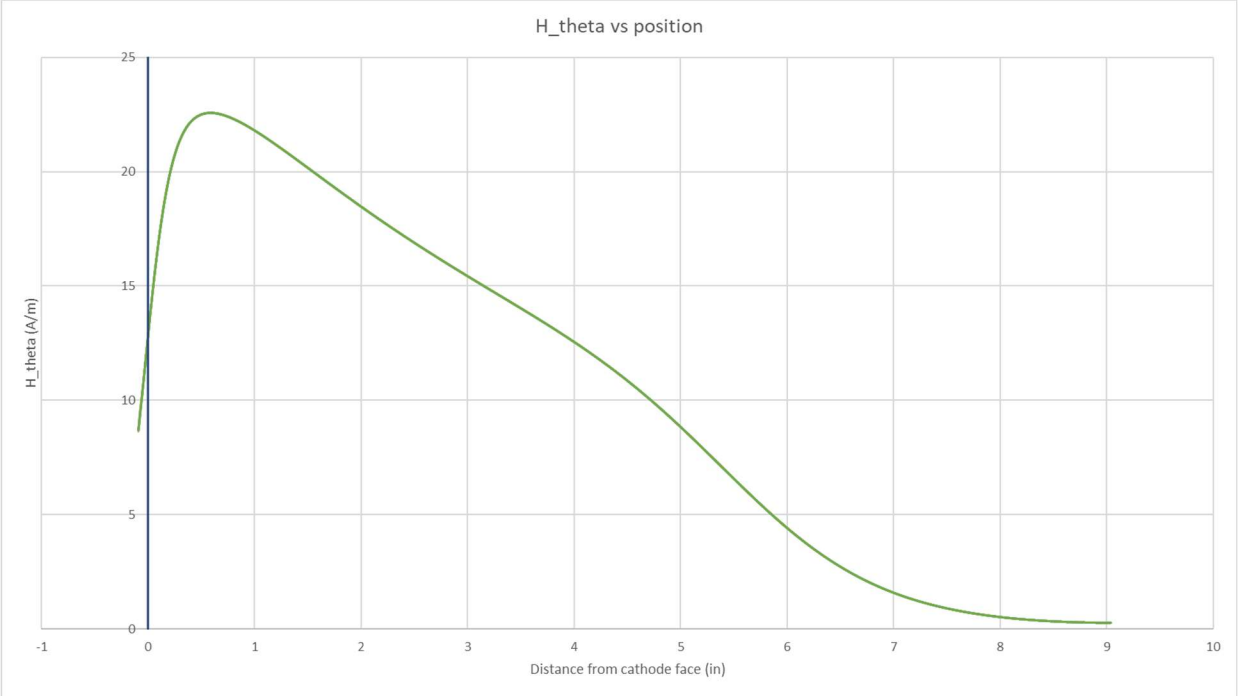

Figure 54. H_Θ field profile along beamline, 1 mm away from beamline.

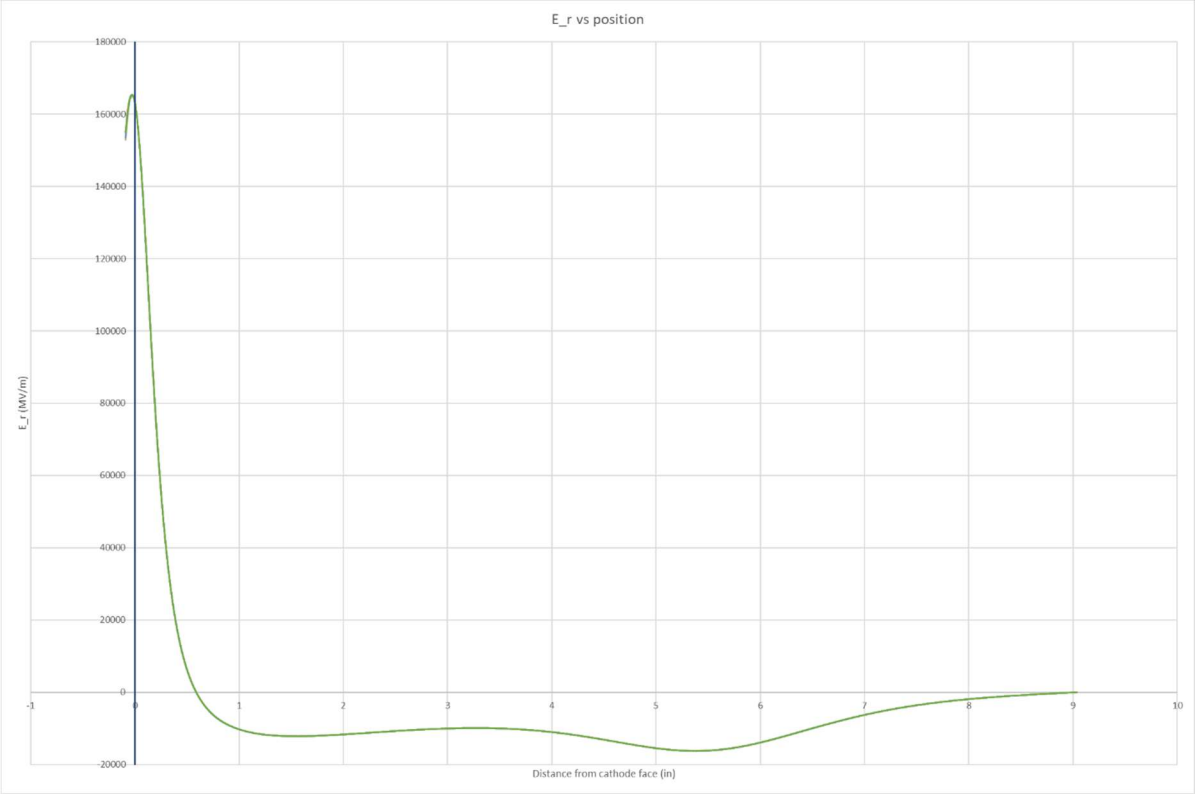

Figure 55. E_r field profile along beamline, 1mm away from beamline.

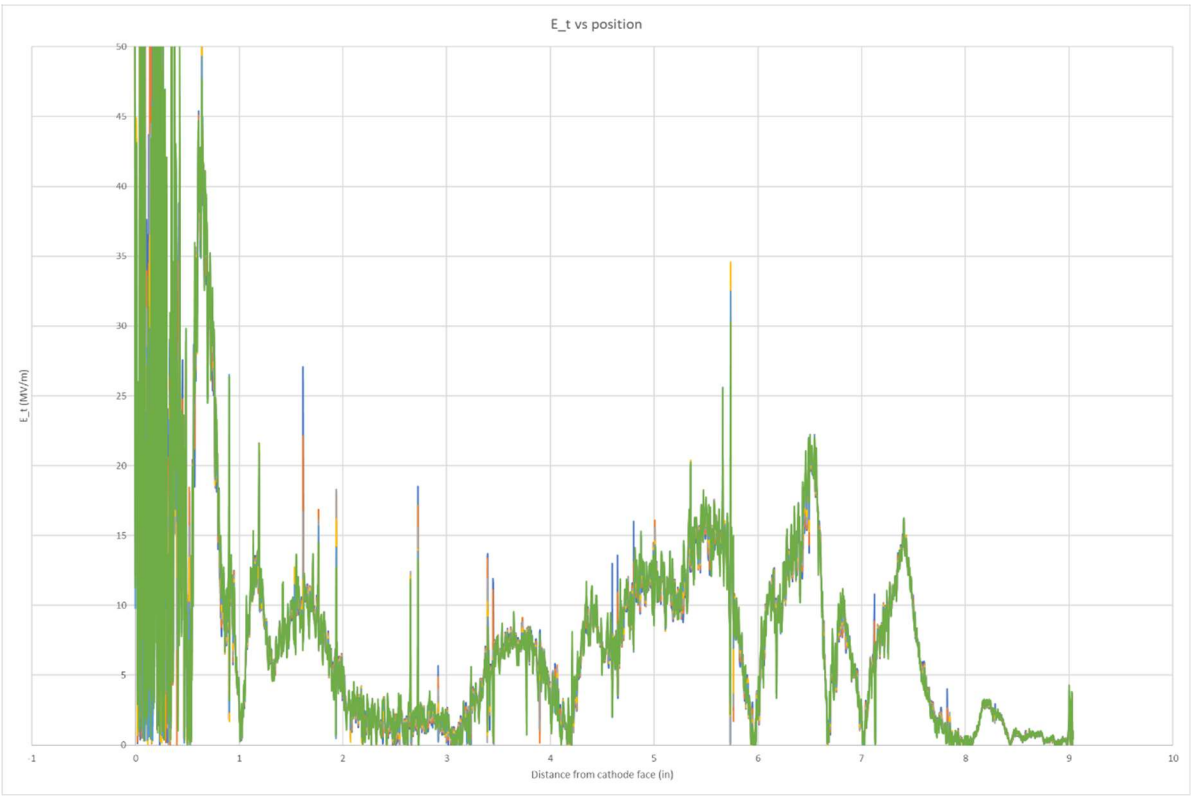

Figure 56. E_Θ field profile along beamline, 1mm away from beamline. This electric field component is vanishingly small compared to E_r and E_z.

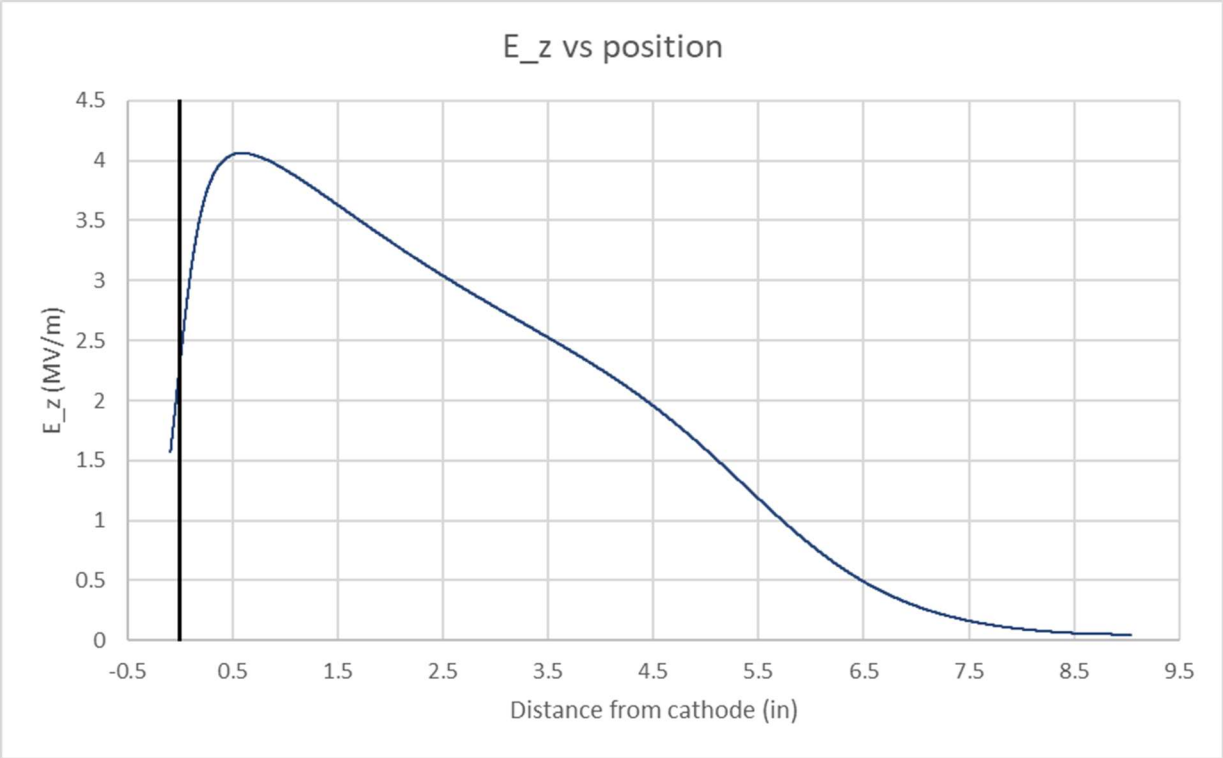

Figure 57. E_z field profile along beamline.

Appendix C – Cleaning the cavity

Disassembly of the WiFEL cryostat

We completely removing the jacketed WiFEL SRF cavity from the cryostat to clean it. Internal objects are mechanically supported in ways that require disassembly in a very specific manner. The half section view of the CAD model of the cryostat in Figure 58 shows the kinematic feet which directly support the cavity. Everything inside the cryostat is either supported mechanically from the jacketed cavity or from the end cap flanges.

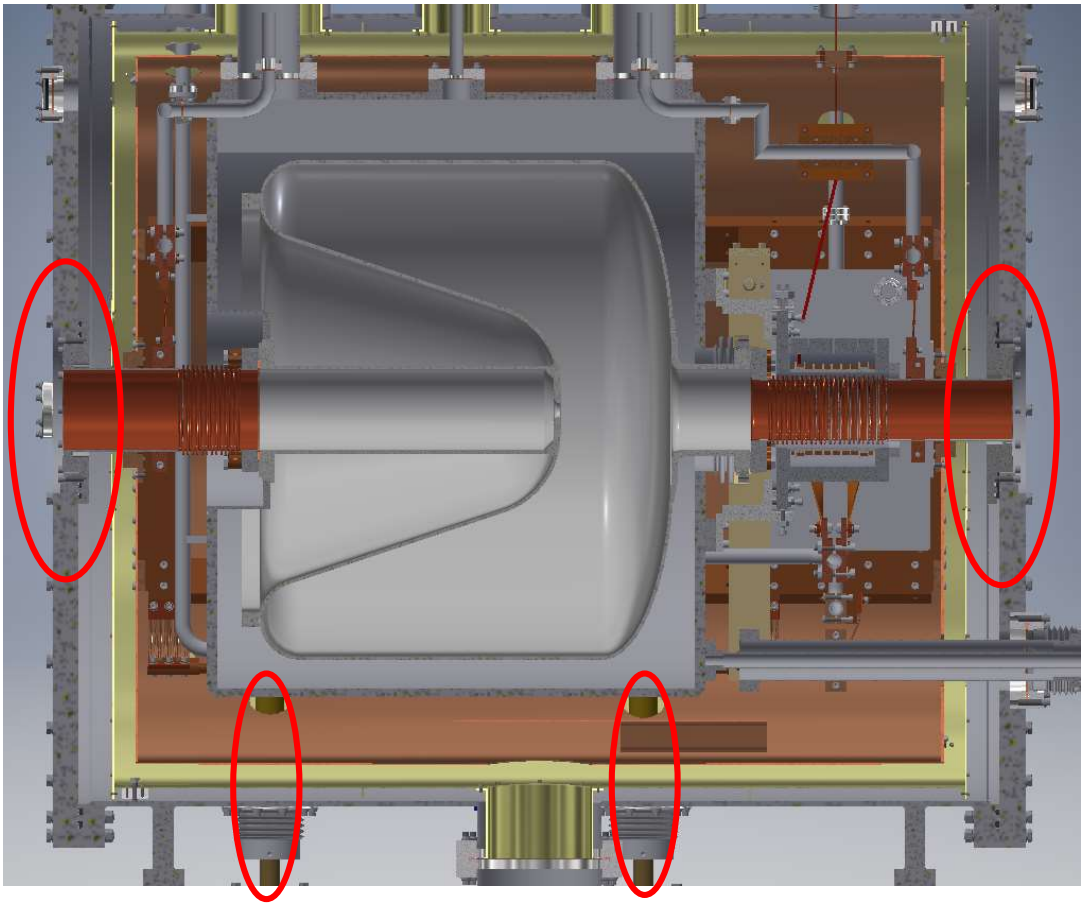

Figure 58. Section view of WiFEL cryostat with the main support points circles in red, end flange supports on top and kinematic feet on bottom.

Careful removal of the end caps combined with securing the beamline flange must avoid sag or twist since the LN2 copper shield is entirely supported by these beam tubes. Figure 59 and Figure 60 show the removal steps.

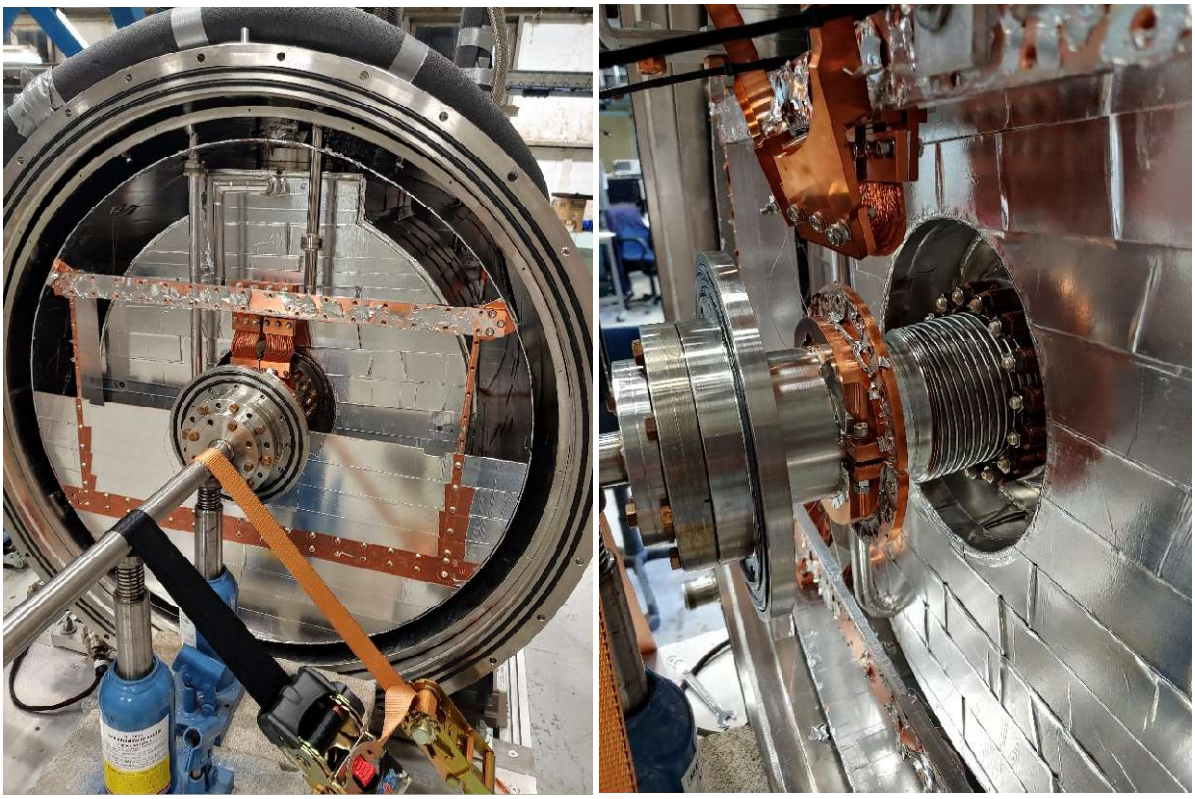

Figure 59. Cathode side of cryostat with end cap removed, with end flange cantilever support setup (left). LN2 copper shield support has been removed from beam tube and is supported by external fixturing (right).

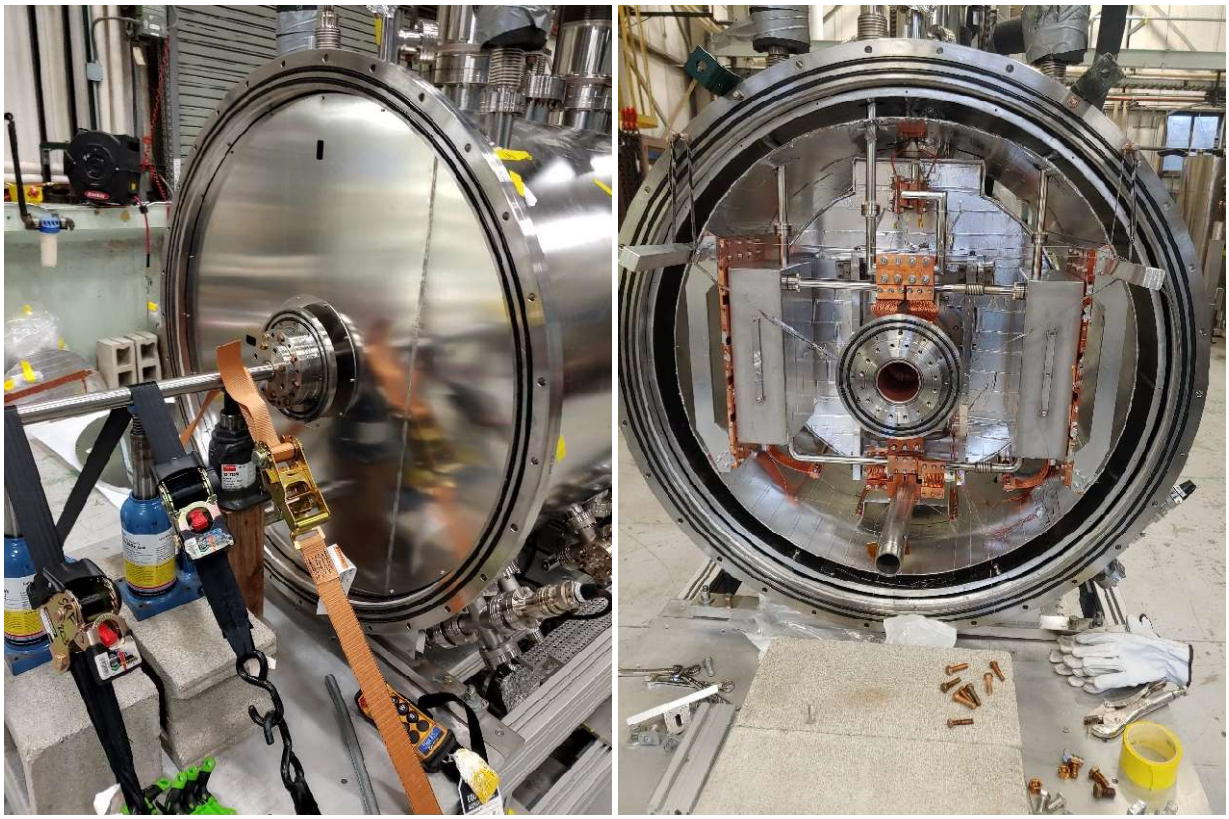

Figure 60. Anode/solenoid side of cryostat with end cap removed, magnetic shield still attached, and same cantilever support setup (left). Magnetic shield and LN2 shield removed, with LN2 shield now entirely supported by external fixturing (right).

The remaining disassembly was mostly straightforward. Two die carts and long Unistrut rails were used to support the jacketed cavity while the kinematic feet were removed, then the cavity was slid out of one end of the cryostat as shown in Figure 61.

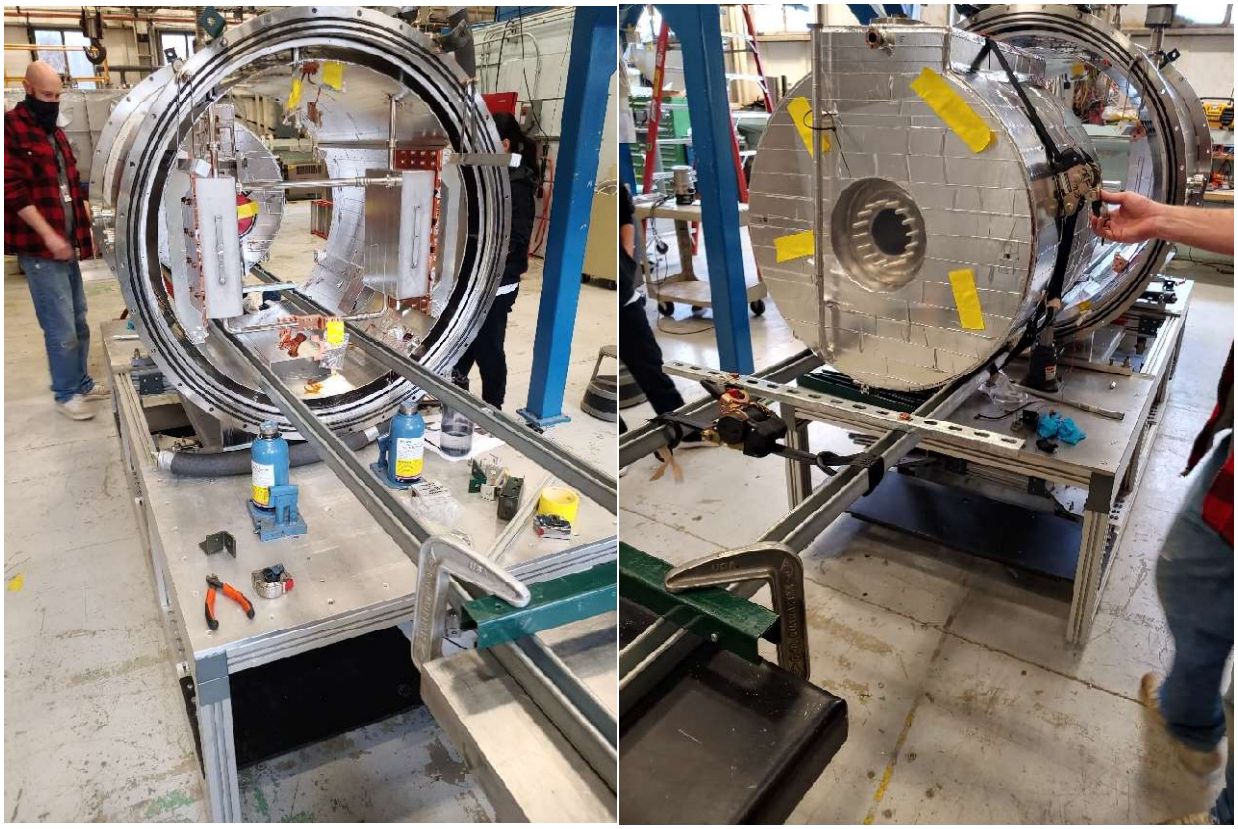

Figure 61. Cavity removal from the cryostat using die carts and Unistrut rails.

The next complication comes from the removal of the solenoid and mechanical tuner from the cavity. The superconducting leads of the solenoid needed to be carefully supported during removal, and the solenoid body is captured by the end flanges of the beam tube but requires independent support. The solenoid body is supported by the jacketed cavity, but the solenoid needs to be released and slide over the beam tube in order to reach the flange bolts, shown in Figure 62.

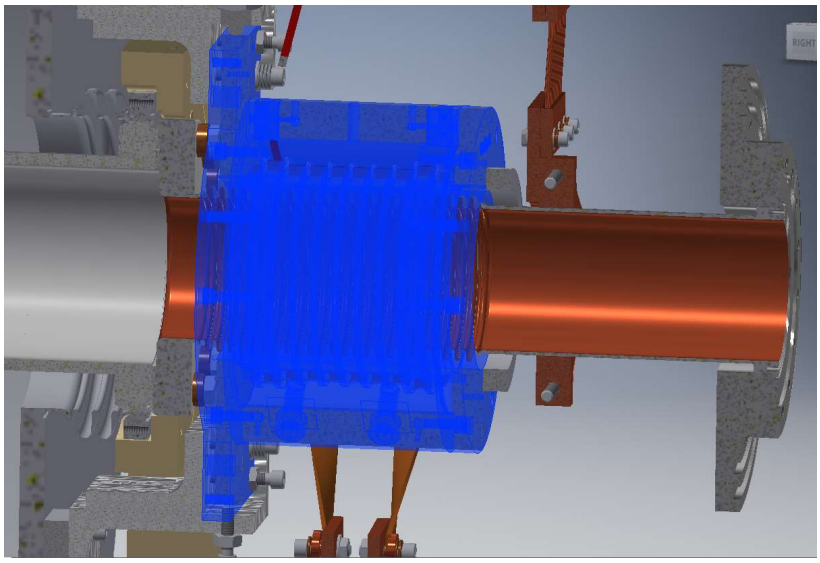

Figure 62. Solenoid body (highlighted in blue) is supported by the cavity jacket. Beam tube is supported by the end flange and from the cavity flange. Removal from cavity flange required sliding the solenoid body over the beam tube to the right.

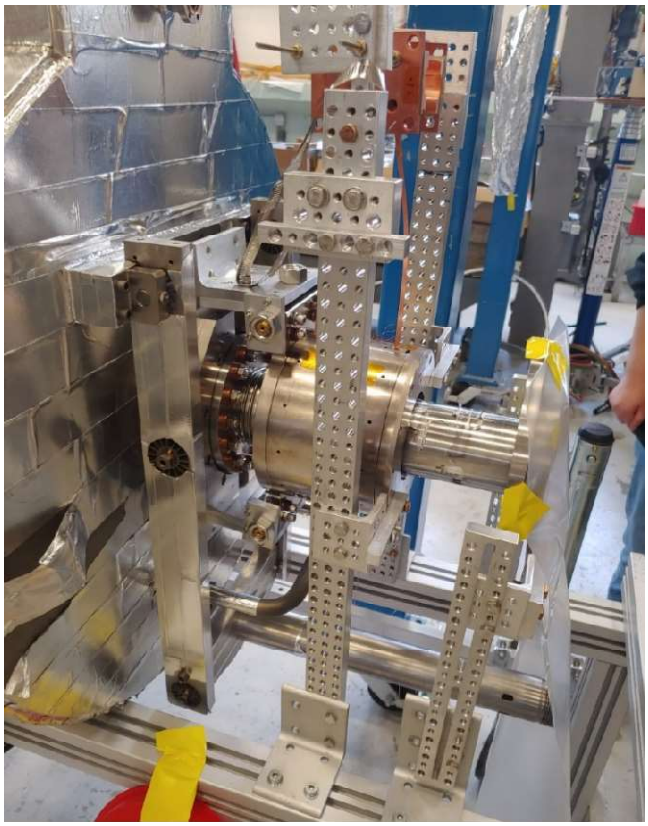

Figure 63. Temporary fixture setup for solenoid and beam tube removal. Solenoid support has been removed from cavity jacket and the solenoid has been slid away for access to the cavity flange bolts. Note the fixture provides support for the superconducting current leads.

Removing the mechanical tuner from the jacket was the final step. The cavity is rigidly supported from the cathode side flange by the jacket, but the beamport side has a thick bellows between the cavity and the jacket to provide the compliance required for the mechanical tuning movement, and the mechanical tuner provides the vertical support for this side of the cavity. This is shown below in a section view in Figure 64.

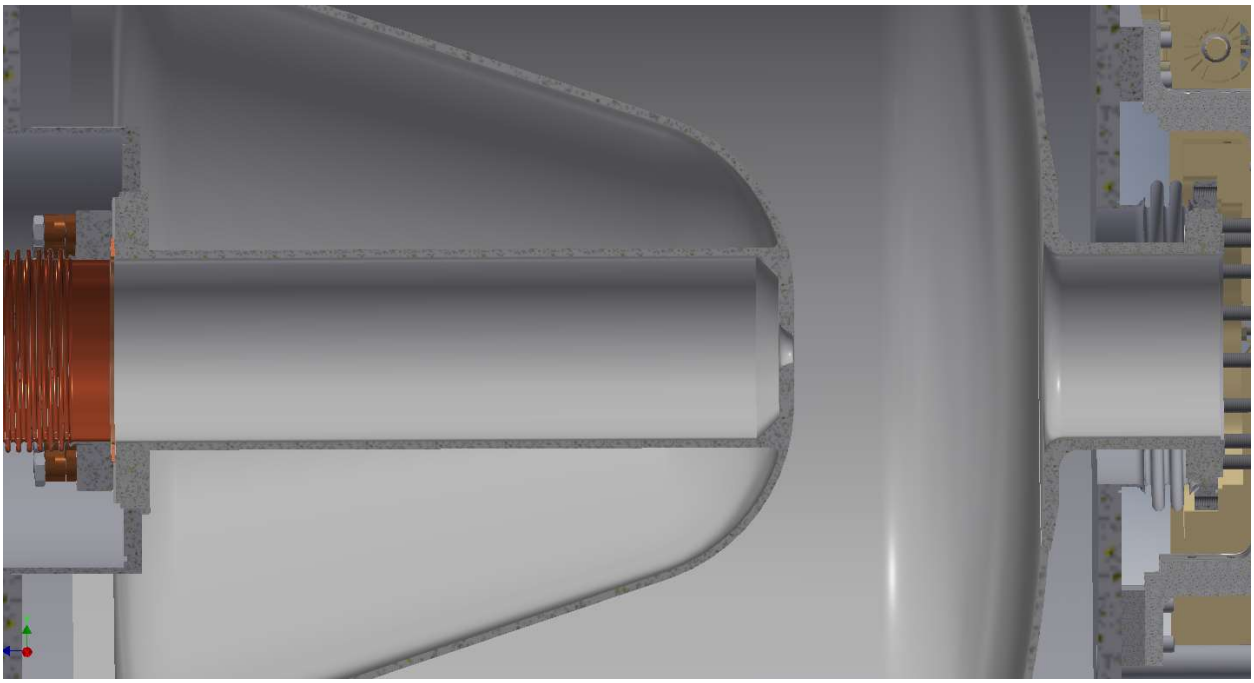

Figure 64. Section view showing how the WiFEL cavity is supported internally. Cathode side is rigidly supported by the helium jacket while the beamport side is supported by the mechanical tuner assembly.

We must be able to orient the cavity in any direction to clean it, but the mechanical tuner only provided vertical support. Brackets were installed temporarily to provide direct support from the jacket to the cavity flange. The cavity was then rotated vertically so that the cavity was entirely supported by the cathode side/cavity jacket and therefore the beamport side support and the entire tuner could then be removed as shown in Figure 65. Additional brackets also shown in Figure 65 were installed for support during the cleaning process.

Figure 65. Temporary supports added to mechanical tuner for cavity flange support before turning vertical (left). Cavity in vertical orientation with tuner removed and supports installed (right).

WiFEL Cavity Cleaning

To clean the WiFEL cavity we first ultrasonically cleaned the cavity with a soapy mixture and then high pressure rinsed the cavity with ultra-pure de-ionized (DI) water. These steps were made difficult by the shape of the cavity and lack of access to certain areas, as there are no ports in the cavity other than the cathode hole and the beam port.

Ultrasonic cleaning was done in two orientations because of the odd shape of the cavity. We could not procure a large enough tank to hold the cavity, so we sealed and filled the cavity with water and dipped the ultrasonic transducer into the water. We added a large vacuum spool piece to the jacketed cavity to enable this step. Figure 66 shows this extra spool piece and ultrasonic transducer outside of the cavity.

Figure 66. Ultrasonic cleaning setup for the WiFEL cavity, with the transducer suspended from an overhead crane (left). The ultrasonic transducer is suspended by a crane while submerged into the water, and a pumping setup was used to transfer DI water into and out of the cavity (right).

The high-pressure rinsing setup was also constrained due to the overall shape of the cavity and lack of additional cleaning ports. The cavity could only be rinsed in one orientation, which limited the total surface area that could be effectively rinsed by our usual high pressure rinsing wand. We held a shorter wand at an angle to reach more areas of the cavity and placed the cavity on a turntable with the beam port facing downward so the entire cavity would be rinsed. Since the wand's spray holes were varied and non-symmetric, the wand was rotated in its fixture many times during the high pressure rinsing to make the rinsing as uniform as possible. The cavity was rinsed for a total of three hours with stops to rotate the wand.

Figure 67. WiFEL cavity, beamport down, on a turntable in the clean room before rinsing with the short HPR wand used for this cleaning visible in the foreground (left). Wand placement and alignment in cavity (right).

WiFEL Clean Assembly

The niobium superconducting RF surface must be clean to avoid field emission and allow very high electric field gradient and therefore total accelerating voltage. Field emission sites can be “conditioned” by injecting RF power to the cavity and blowing them up with localized arcing, which hopefully spreads most of them into lower electric field regions. Plasma processing can also help, but it is better to start with a pristine surface and keep it that way.

The assembly of the cavity with any part of the RF space open to the outside environment was done in a clean room environment. The bulk of the assembly was done in Argonne’s Physics division ATLAS clean room to limit the possible contamination. Figure 68 shows the cavity on its cart in the cleanroom.

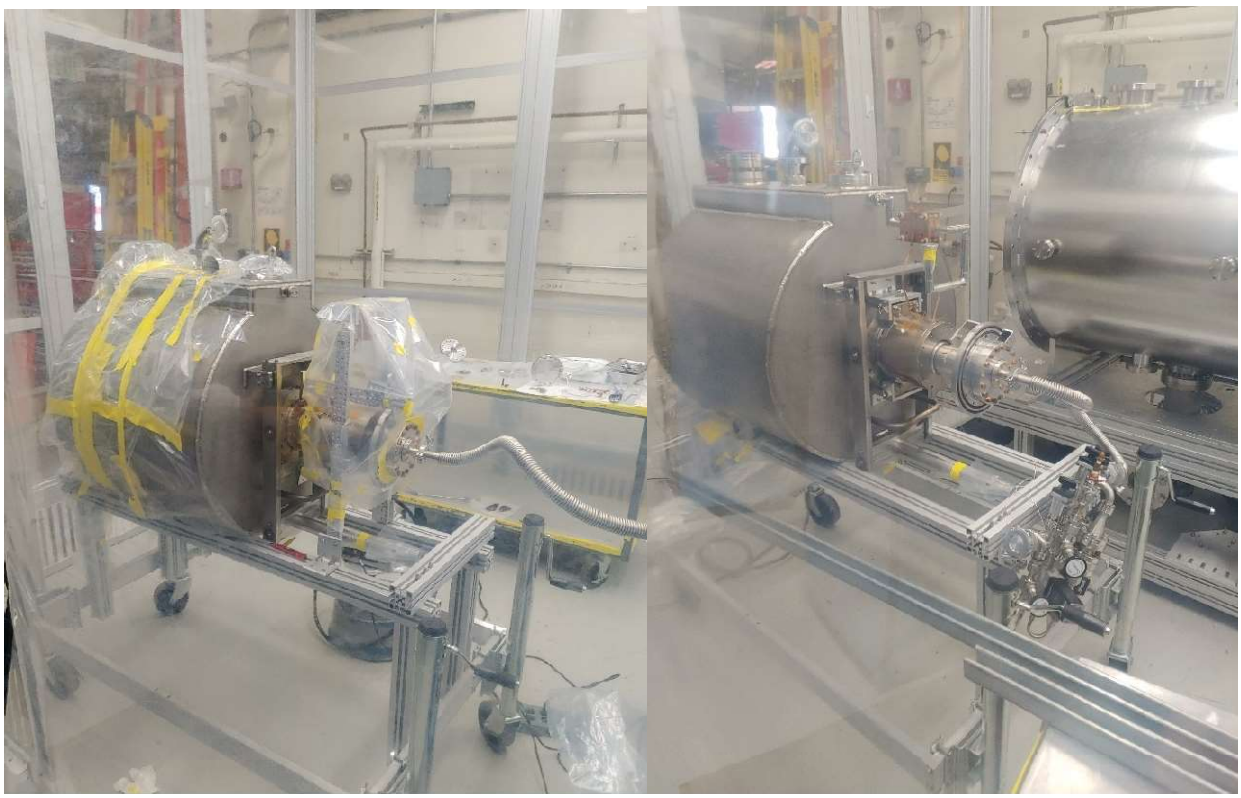

Figure 68. WiFEL cavity on its cart in the ATLAS clean room. RF space is sealed with the flexible hose connected to the “up-to-air” system (left). Cavity with solenoid support removed and “up-to-air” system tied to the cart (right).

The “up-to-air” system is one of the most utilized tools for clean vacuum pumping of the cavity. It is essentially a small vacuum manifold with various valves, a pressure transducer, as well as two mass flow controllers. This allows the user to control both the direction and rate of flow. This is done to keep a constant mass flow during pump out in an effort to avoid turbulent flow that could stir any remaining contamination inside. The system also has a very fine gas filtration on an input to allow backfilling of the cavity space with either clean air or nitrogen if supplied from a gas cylinder. This is particularly useful for creating a purge flow of nitrogen, a technique used to create positive pressure inside the cavity space while working on an exposed port, which hopefully helps to minimize contamination.

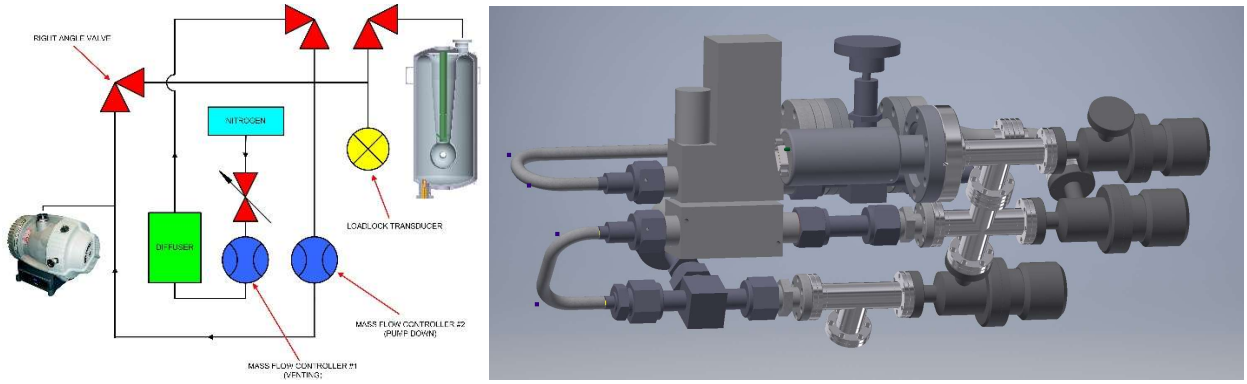

Figure 69. Up-to-air system flow diagram (left) and 3D Inventor model (right).

We also use a Climet Model CI-750t particle counter sensitive to sub-micron level particles, which helps to confirm that the environment is clean enough to open the cavity vacuum space. This device checks particle counts during preparation steps such as initial cleaning and immediately before un-sealing the cavity space.

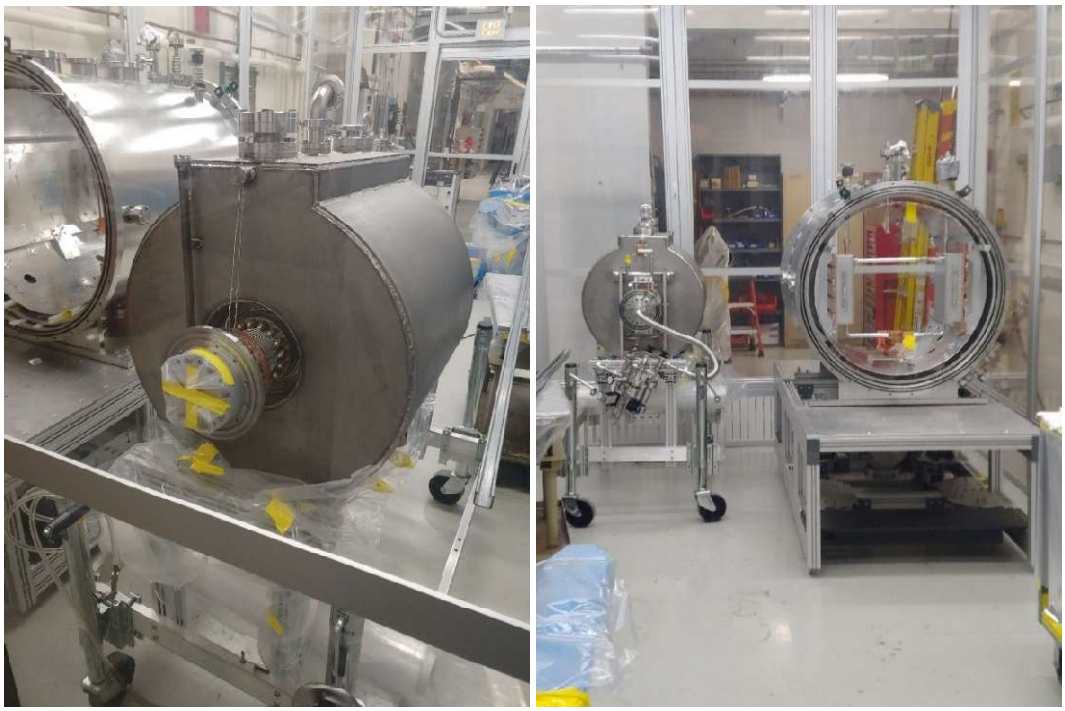

Figure 70. WiFEL cavity with cathode and anode side flanges (along with superconducting solenoid) prepped for assembly into the cryostat.

The first components requiring clean assembly were both the cathode and anode side flanges of the cavity and the mechanical tuner. On the anode side this also included the superconducting solenoid, with all the complications that were mentioned during the disassembly. Figure 70 shows the cavity after the first set of clean assembly tasks. On the cathode side this included a bellows and an end flange that mates to the cryostat end cap. On the beamport side the solenoid/beamtube/bellows assembly was assembled with our “up-to-air” system on the cryostat end flange.

Because of the required order of operations for assembly of the cryostat, a few of the desired clean assembly steps had be completed after the cavity was put back into the cryostat. Many of the key surfaces were sealed off with clean plastic for intermediate “dirty” steps. The remaining clean connections to be made were the cathode side flange (replaced with the RF pickup assembly) and the beamport side flange connected to the coupling cavity. Both assemblies required having the cryostat almost fully assembled, which was a very dirty process. The “up-to-air” system was utilized during these connections by having a clean nitrogen purge flow providing positive pressure to reduce contamination during these operations. The purge was kept flowing up until pressure built slightly in the cavity, indicating an adequate seal.

Figure 71. WiFEL cavity being lifted onto Unistrut rails by a hoist just outside of the cleanroom.

The WiFEL cavity was then moved back into the cryostat with the initially assembled parts (bellows/flanges, solenoid, and tuner) carefully sealed as best as possible with clean plastic. Figure 71 shows two die carts provided height adjustment and translational movement with the Unistrut rails between. A hoist lift was used to move the cavity from its cart onto the rails just outside of the cleanroom. Once the cavity was slid into the cryostat (seen in Figure 72) and the kinematic feet (seen in Figure 73) were installed the assembly continued inside the cleanroom.

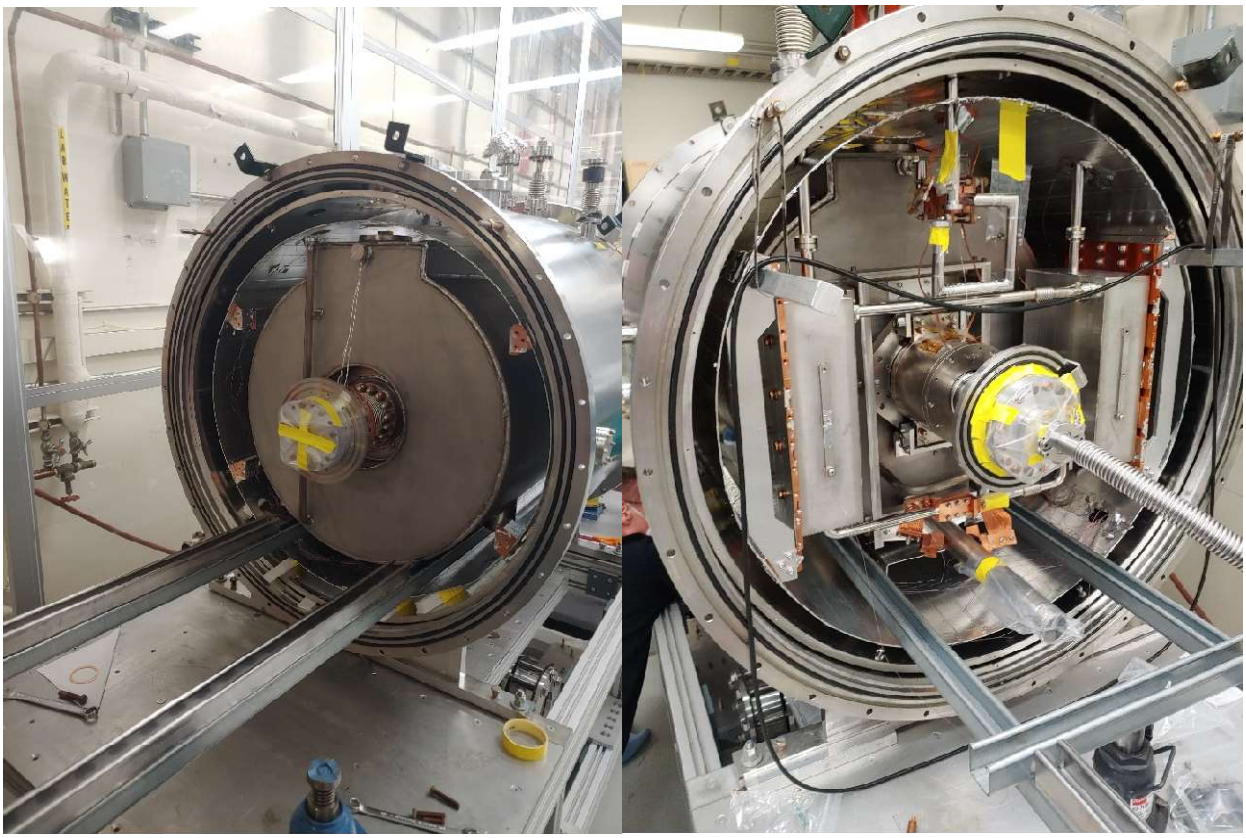

Figure 72. The WiFEL cavity in the process of being slid into the cryostat just outside of the cleanroom.

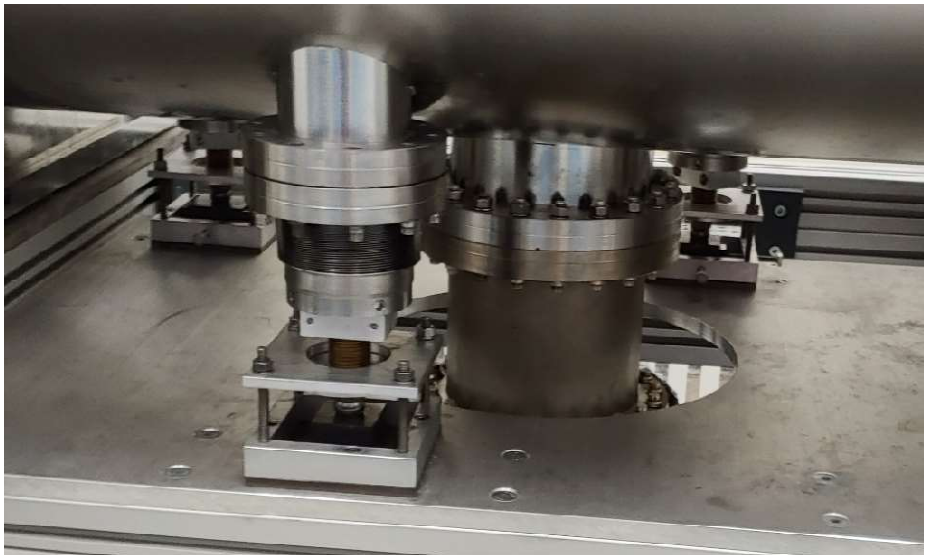

Figure 73. Close up of the kinematic feet that support the cavity. G10 rods with thermal strapping penetrate the cryostat walls in three spots for support.

The internal cryostat helium system plumbing connections shown in Figure 74 were made and leak checked. We added four cryogenic silicon diodes to measure temperatures at four points: the mechanical tuner, the solenoid cooling loop, a helium boil off port, and midway up the helium jacket.

Figure 74. Internal cryostat helium system plumbing connection process: solenoid intercept loop (left), cathode bellows intercept loop and fast cooldown line and respective top connections (center), helium leak checking conflat joints (right).

The endcaps were lifted using a hoist while the end flange was cantilevered using the same bottle jack/tow strap rig as during disassembly, threading over the supports until the sealing surfaces mated. Steps are shown in Figure 75.

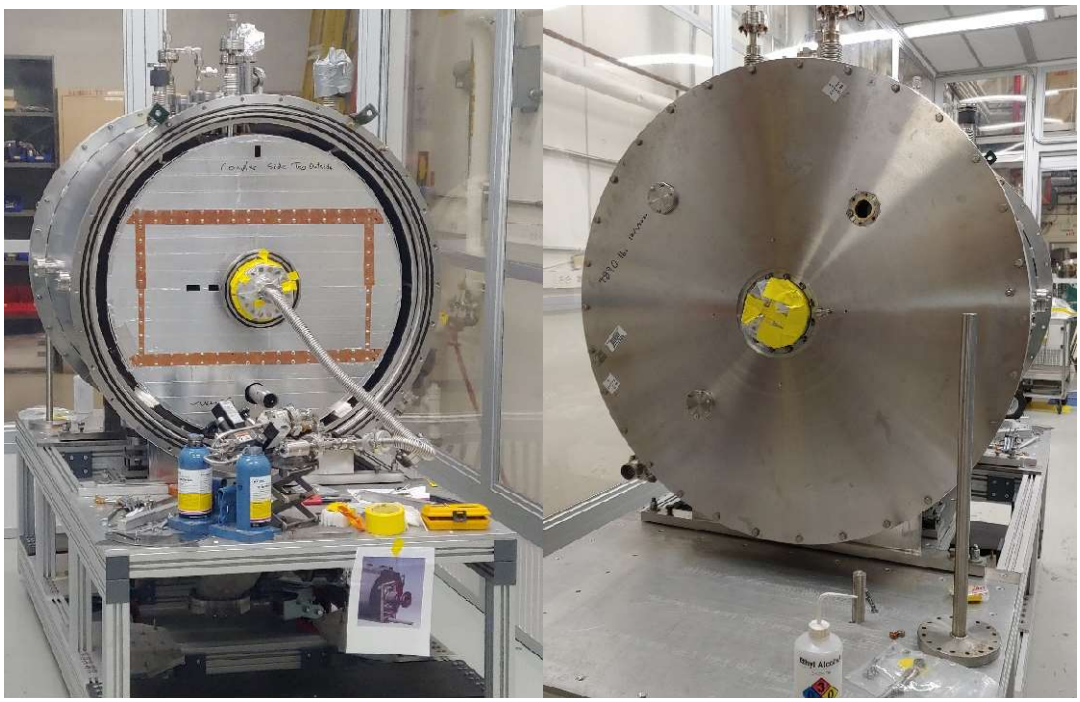

Figure 75. WiFEL cryostat in the process of being sealed: beamport/solenoid side with shielding replaced before end cap installation (left), cathode side with end cap installed (right).

The two remaining clean assemblies could be addressed once both ends of the cryostat were sealed. The cathode side flange assembly included the burst disc assembly as well as the RF pickup assembly shown in Figure 76. The other side of the cryostat had to attach the coupling cavity and power coupler. These were cleaned and pre-assembled then slid onto a Minitec platform on the cryostat table shown in Figure 77. This assembly also contains the gate valve and turbomolecular pump for the cavity space. A clean nitrogen purge gas flowed through the cavity space during this process.

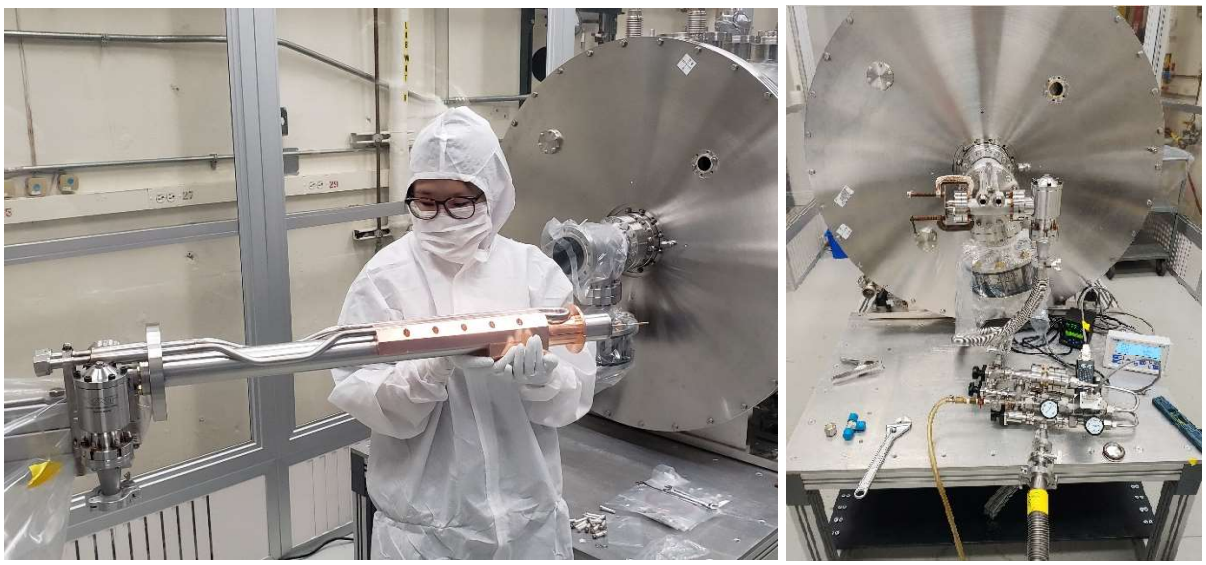

Figure 76. RF pickup assembly being prepared for assembly, cantilevered off of a moveable cart (left). Post-assembly with up-to-air system attached (right).

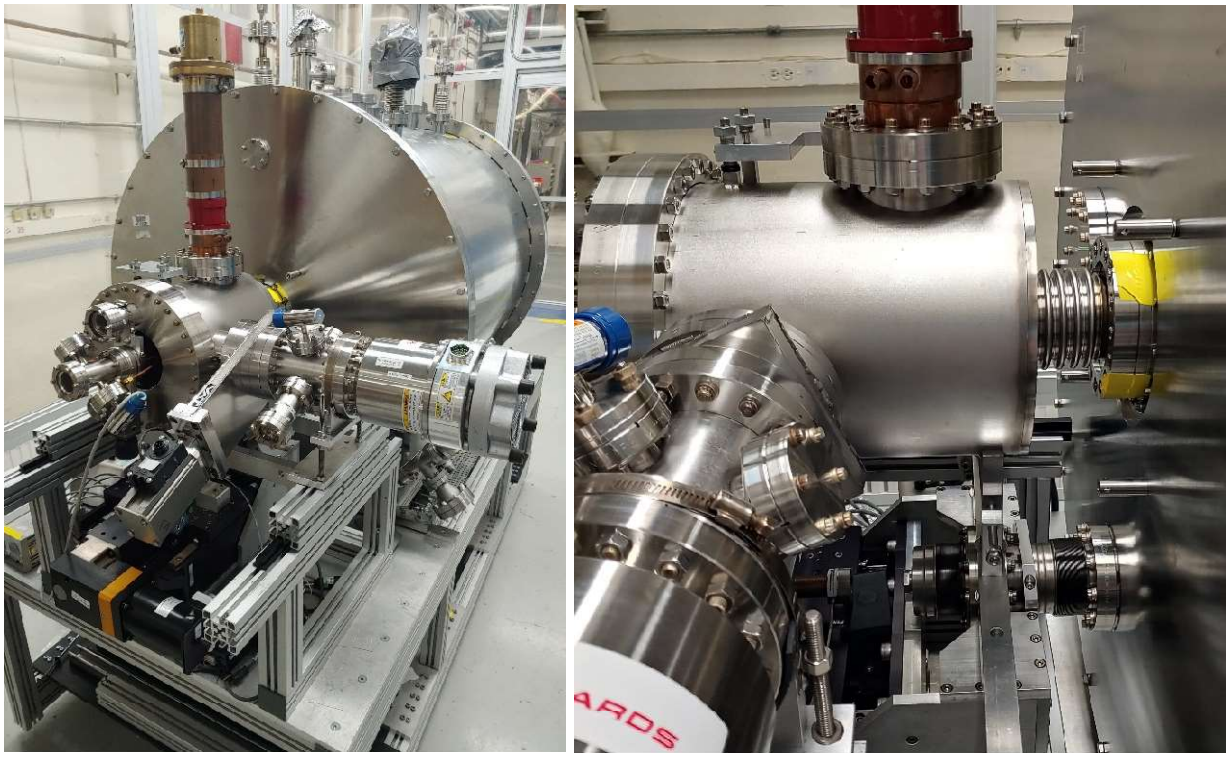

Figure 77. Coupling cavity and power coupler (along with gate valve and turbomolecular pump) installed onto the solenoid side of the cryostat (left). A closeup of the last clean connection to be made during the assembly (right).

After a quick RF continuity check done to ensure there were no issues with the pickup antenna or the power coupler assembly, the cavity space was evacuated. At least one conflat seal was not tightened properly, but the pumping was done in the cleanroom environment, so hopefully few particles were dragged into the cavity space. This was one of two vacuum accidents that lead us to believe our final results could be improved upon, as they were in general limited by field emission likely caused by these vacuum issues.